Applied Machine Vision

Advancing Quality Assurance and Quality Control in Industrial Manufacturing

Mikkelstrup, Anders Faarbæk

DOI (link to publication from Publisher):
10.54337/aau596075654

Publication date:
2023

Document Version
Publisher's PDF, also known as Version of record

APPLIED MACHINE VISION

ADVANCING QUALITY ASSURANCE AND QUALITY CONTROL IN INDUSTRIAL MANUFACTURING

BY
ANDERS FAARBÆK MIKKELSTRUP

DISSERTATION SUBMITTED 2023

AALBORG UNIVERSITY
DENMARK

Applied Machine Vision

Advancing Quality Assurance and Quality Control in Industrial Manufacturing

PhD Thesis

Anders Faarbæk Mikkelstrup

Thesis submitted August 2023

Dissertation submitted: August 2023

PhD supervisor:: Assoc. Prof. Morten Kristiansen
Aalborg University, Denmark

PhD committee: Associate Professor Brian Lau Verndal Bak
Aalborg University, Denmark

Professor Emeritus Gunnar Bolmsjö
Linnaeus University, Sweden

Professor Lazaros Nalpantidis
Technical University of Denmark (DTU), Denmark

PhD Series: Faculty of Engineering and Science, Aalborg University

Department: Department of Materials and Production

ISSN (online): 2446-1636
ISBN (online): 978-87-7573-655-3

Published by:
Aalborg University Press
Kroghstræde 3
DK – 9220 Aalborg Ø
Phone: +45 99407140
aauf@forlag.aau.dk
forlag.aau.dk

Printed in Denmark by Stibo Complete, 2023

Curriculum Vitae

Anders Faarbæk Mikkelstrup

Anders Faarbæk Mikkelstrup was born and raised in Holstebro, Denmark. Engineering has always fascinated him, which led him to enrol in the BSc program in Mechanical Engineering and Production at Aalborg University. He then earned an MSc in Manufacturing Technology, also at Aalborg University. Afterwards, he joined the Robotics and Automation group at Aalborg University to pursue a PhD, playing an integral part in the two industrial projects, CeJacket and INTERASE. During this time, he conducted research in collaboration with numerous Danish manufacturing companies, contributing to a greater understanding of the possibilities of machine vision systems in manufacturing. As a part of the PhD, Anders collaborated with and had an external stay at the University of California, San Diego, under the supervision of Professor Henrik I. Christensen.

Anders' research mainly focuses on the design, development, and practical application of machine vision systems to innovate and enhance manufacturing systems, particularly emphasising 3D machine vision.

Curriculum Vitae

Abstract

Driven by technological advancements and improved affordability of imaging components, machine vision has grown considerably to become a fundamental technology within intelligent and computer-integrated manufacturing, permitting more complex and advanced uses. Therefore, this PhD study aims to explore the potential of applying machine vision for quality assurance and quality control of manufacturing processes, supporting the digital transformation. The PhD thesis follows the Design Science Research (DSR) methodology and is based on two industrial research projects, CeJacket and INTERLASE. Through a comprehensive literature study, several research gaps are identified, leading to the formulation of two research questions and associated research objectives. To answer the research questions, the PhD thesis focuses on solving defined problems within the industrial cases.

In the context of CeJacket, this thesis studies the use of machine vision to propose an automated system that utilises 3D scanning for adaptive post-weld treatment and quality inspection. The purpose is to improve treatment reproducibility and quality assurance, particularly focusing on high-frequency mechanical impact (HFMI) treatment. The proposed system demonstrates substantial improvements in the work environment, reproducibility, productivity, and overall quality assurance and quality control.

Related to the INTERLASE project, the thesis proposes several solutions based on machine vision research to optimise the fundamentally sensitive laser processes, emphasising calibration and monitoring. These include (1) a flexible and generic method for in situ calibration of galvanometric scanner systems, allowing accurate processing even with limited prior knowledge of the system; (2) an in-line method to identify local variations in surface absorption for laser marking, thereby enhancing the process stability and quality assurance; and (3) a system for in-line process monitoring of double-curved robotic laser welds, leading to strengthened process knowledge and quality assurance.

The outcomes of the PhD study demonstrate how machine vision can optimise manufacturing processes and deliver effective and robust solutions for quality assurance and quality control.

Abstract

Resumé

Drevet af teknologiske fremskridt og mere omkostningseffektive komponenter har *machine vision* oplevet betydelig vækst og er blevet en nøgleteknologi inden for intelligent og computerintegreret fremstilling. Dette har muliggjort mere komplekse og avancerede anvendelser. Derfor har dette ph.d.-studie til formål at udforske potentialet ved at anvende *machine vision* til kvalitetssikring og -kontrol af fremstillingsprocesser for at understøtte den digitale transformation. Ph.d.-afhandlingen følger Design Science Research (DSR)-metodikken og er baseret på to industrielle forskningsprojekter, CeJacket og INTERLASE. Gennem et omfattende litteraturstudie identificeres adskillige forskningshuller, hvilket fører til formuleringen af to forskningsspørgsmål og tilhørende forskningsmål. For at besvare forskningsspørgsmålene fokuserer afhandlingen på løsning af definerede problemstillinger indenfor de industrielle cases.

I forbindelse med CeJacket studerer denne afhandling brugen af *machine vision* til at foreslå et automatiseret system, der anvender 3D-scanning til adaptiv post-svejsebehandling og kvalitetsinspektion. Formålet er at forbedre behandlingens reproducerbarhed og kvalitetssikring, især fokuseret på *high-frequency mechanical impact* (HFMI) behandling. Det foreslåede system demonstrerer væsentlige forbedringer i arbejdsmiljøet, reproducerbarheden, produktiviteten og den overordnede kvalitetssikring og -kontrol.

Relateret til INTERLASE-projektet foreslår afhandlingen adskillige løsninger baseret på forskning i *machine vision* for at optimere de fundamentalt følsomme laserprocesser, med vægt på kalibrerings- og overvågningsaspekter. Disse omfatter (1) en fleksibel og generisk metode til integreret kalibrering af galvanometriske scannersystemer, der muliggør nøjagtig bearbejdning selv med en begrænset forudgående viden om systemet; (2) en tilgang, der kan identificere lokale variationer i overfladeabsorptionen til lasermærkning som en del af proceslinjen, hvorved processtabiliteten og kvalitetssikringen forbedres; og (3) et system til procesovervågning af dobbeltkrumme robotlasersvejsninger, hvilket fører til styrket procesviden og kvalitetssikring.

Resultaterne af ph.d.-studiet viser, hvordan *machine vision* er i stand til at optimere fremstillingsprocesser og levere effektive og robuste løsninger til kvalitetssikring og -kontrol.

Contents

Thesis Details

Thesis Title:	Applied Machine Vision: Advancing Quality Assurance and Quality Control in Industrial Manufacturing
PhD Student:	Anders Faarbæk Mikkelstrup
Supervisor:	Morten Kristiansen

The main body of this thesis consists of the following published peer-reviewed papers:

Paper A [1] A. F. Mikkelstrup, M. Kristiansen, and E. Kristiansen, "Development of an automated system for adaptive post-weld treatment and quality inspection of linear welds," *International Journal of Advanced Manufacturing Technology*, vol. 119, pp. 3675–3693, 2022.

Paper B [2] A. F. Mikkelstrup, G. N. Nikolov, and M. Kristiansen, "Three-Dimensional Scanning Applied for Flexible and In Situ Calibration of Galvanometric Scanner Systems," *Sensors*, vol. 23, no. 2142, pp. 1-19, 2023.

Paper C [3] A. F. Mikkelstrup, A. N. Thomsen, and M. Kristiansen, "A novel method for approximating local changes in the surface absorption for laser marking using 3D laser scanning," *IOP Conference Series: Materials Science and Engineering*, vol. 1135, no. 012002, p. 1-11, 2021.

Paper D [4] A. Mikkelstrup, M. Thomsen, K. Stampe, B. Endelt, J. Boll, E. Kristiansen, and M. Kristiansen, "Quality inspection system for robotic laser welding of double-curved geometries," *Procedia Manufacturing*, vol. 36, pp. 50–57, 2019.

In addition to the main papers, the following publications and patents have also been made or issued:

Paper E [5] A. F. Mikkelstrup and M. Kristiansen, "Integrated Digital Reconstruction of Welded Components: Supporting Improved Fatigue Life Prediction", *arXiv preprint arXiv:2307.15604*, pp. 1-6, 2023, submitted in July 2023 to the IEEE International Conference on Imaging Systems and Techniques (IST2023).

Paper F [6] M. Kristiansen, R. Darula, B. Endelt, A. F. Mikkelstrup, J. Schjødt-Thomsen, J. H. Andreasen, F. Farrokhi, P. K. Hansen, P. B. W. Jensen, E. Putnam, and N. Hansen, "Improving the fatigue life of large offshore foundations," *Marine Structures*, vol. 87, no. 103314, p. 1-13, 2023.

Paper G [7] G. N. Nikolov, A. N. Thomsen, A. F. Mikkelstrup, and Morten Kristiansen, "Computer aided process planning system for laser forming: From CAD to part", *International Journal of Production Research*, pp. 1-18, 2023.

Paper H [8] S. E. Schrøder, U. L. Christensen, M. Hessellund, A. L. Enevoldsen, A. F. Mikkelstrup, and M. Kristiansen, "Object detection and colour evaluation of multicoloured waste textiles using machine vision," in Proceedings of the 16th International Conference on PErvasive Technologies Related to Assistive Environments, ser. PETRA '23. New York, NY, USA: Association for Computing Machinery, 2023, p. 543–549.

Patent A [9] M. Kristiansen, E. Kristiansen, B. Endelt, S. Villumsen, A. Thomsen, and A. Mikkelstrup, "A method for processing elements into final elements," Jan. 2022, wO 2022/002338 A1; G05B 19/4097 2006.1.

Patent B [10] M. Kristiansen, E. Kristiansen, A. Thomsen, B. Endelt, A. Mikkelstrup, and G. Nikolov, "A planning method for processing an element into a final element," Jan. 2022, wO 2022/002339 A1; G05B 19/4097 2006.1

This thesis has been submitted for assessment in partial fulfilment of the PhD degree. The thesis is based on the submitted or published scientific papers and issued patents listed above. Parts of the papers are used directly or indirectly in the extended summary of the thesis. As part of the assessment, co-author statements have been made available to the assessment committee and to the faculty.

Preface

This PhD thesis presents the culmination of several years of research to investigate the potential of applied machine vision to advance quality assurance and quality control in industrial manufacturing. The PhD thesis is formatted as a collection of papers to allow for a broader exploration of the research questions, focusing on different aspects of quality assurance and quality control within various manufacturing processes. As such, the main body of the thesis is composed of four main publications in which I am the principal author and supported by four additional papers and two patents.

The PhD thesis has been carried out at the Department of Materials and Production at Aalborg University and has been generously supported by the two Innovation Fund Denmark projects: "*Create Disruptive Solutions for Design and Certification of Offshore Wind Jacket Foundations*", project number 6154-00017B, and "*Integrated Laser Processes for Cost-Effective Prototyping and One-of-a-Kind Production*", project number 7050-00024B.

The journey to complete this PhD has been a significant, sometimes overwhelming, yet profoundly enlightening part of my life. In fact, I had never planned to pursue the PhD, but when given the opportunity, I knew I would regret not taking on the challenge. Through the years, I have gained theoretical knowledge within applied machine vision and immense practical experience in commissioning and programming robots and PLCs. I can confidently say that the many late nights, the battle against perfectionism, the endless debugging, and even the moments of doubt have all aided my personal and academic growth. Throughout the journey, countless people have contributed their time, effort, and expertise to guide me through the PhD. I would like to express my sincerest gratitude to all who have made this possible.

First and foremost, I would like to thank my supervisor, Morten Kristiansen. Not only did you present me with the opportunity to pursue a PhD degree, but your guidance and support, even when my motivation was lacking, have been invaluable. In addition, I wish to show my appreciation to Ewa Kristiansen. You gave me useful guidance, acting as my co-supervisor at the start of the PhD. A special note of thanks also goes to Henrik Iskov Christensen and his research group at the University of California, San Diego, for hosting me

during my research stay. Your hospitality and support enriched my research experience and provided a stimulating environment despite the stay sadly being interrupted due to COVID-19. Moreover, I want to show my appreciation to Jens Vestergaard Boll. You offered an essential industrial perspective on aspects of laser processing and the challenges therein.

To the fantastic Robotics and Automation group, one could not have wished for a better research group. Your collective wisdom and unwavering support, personally and professionally, have made my time at the university an unforgettable experience. I would like to especially thank Dimitris Chrysostomou, Dimitris Raptis, and Anders Noel Thomsen, who gave me valuable feedback to improve the PhD thesis. My appreciation also goes to the skilled team at the laboratory at Fibigerstræde, always providing essential assistance regardless of the task. Furthermore, I would like to mention Georgi Nikolaev Nikolov specifically. Our friendship, insightful discussions and countless hours at the laser cell have undoubtedly contributed to my research and personal development.

In addition, I would like to express my appreciation to all of my friends, who each, in their own way, have been there when I needed it. However, I especially want to thank Mathias Ernst Halvorsen and Kristoffer Stampe. Words cannot express my appreciation for your constant encouragement, understanding, and companionship throughout my studies and on the sideline of the PhD.

But most importantly, I owe my family my sincerest gratitude, especially my parents, Jesper and Jette, and my brother, Morten. You always supported and believed in me, even at the most challenging times. However, at the heart of my gratitude lies my loving fiancée, Dimitra. Not only did you birth our beautiful daughter, Sophia, but your love, patience and faith in me, kept me going at times when I, admittedly, was on the brink of surrender. Without you and your sacrifices, this PhD would not have been possible. Therefore, out of the most profound respect, I dedicate this thesis to you, Dimitra.

In conclusion, I would like to reflect upon a quote by Sir Edmund Hillary: *"It is not the mountain we conquer, but ourselves."*. This PhD has truly been a mountain, a challenge that I took up not only to enrich my knowledge but especially to challenge my resilience and perseverance. Looking back, I can certainly say I am leaving this journey as a stronger and more complete individual. Finally, I hope this work contributes to a better understanding of the possibilities for applied machine vision to advance quality assurance and quality control in industrial manufacturing and provides a foundation for future research.

Aalborg University, August 14, 2023

Anders Faarbæk Mikkelstrup

Part I

Introduction

Chapter 1

Background

This chapter introduces the background and motivation along with the two industrial cases that form the basis of the study. Additionally, the research methodology used to guide the study is presented. Finally, an overview of the thesis concludes the chapter.

1.1 Motivation

In an evolving world where customer demands rapidly change, flexible and adaptive manufacturing systems capable of handling small batches and multiple variations of products are in demand. Traditional applications in manufacturing are characterised as stand-alone and segregated, with poor integration of physical and digital systems. This inherently leads to a lack of automation and control capabilities, resulting in limited flexibility. [11]

In an attempt to ensure that Europe stays at the forefront of manufacturing, in 2013, the European Commission launched a public-private partnership under Horizon 2020, now Horizon Europe, creating the *Factories of the Future Roadmap*[1] for advanced manufacturing research and innovation. The aim is to enable a more innovative, competitive, and sustainable European industry by realising the next industrial revolution, known as Industry 4.0.

Introduced in Germany in 2011, Industry 4.0 is expected to deliver an annual manufacturing efficiency gain of 6% - 8% [12], while Germany's electrical industry association predicts an increase in industrial productivity of up to 30% [13]. An increased level of digitalisation is one of the driving forces behind Industry 4.0 and the development of smart factories. The increased level of digitalisation is achieved through cyber-physical systems, defined as systems of interconnected sensors combined with embedded computers that are integrated and able to control and monitor the physical processes [14]. As such, Industry

[1] https://www.effra.eu/factories-future-roadmap

4.0 embraces data acquisition and exchange in manufacturing technologies. The result is not only flexibility and adaptiveness of industrial manufacturing but improved performance, transparency, and quality of the manufacturing processes [11].

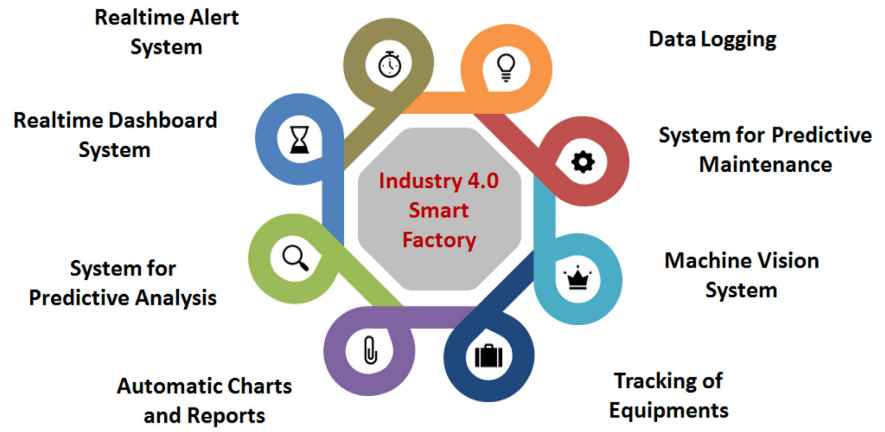

Fig. 1.1: Major components of Industry 4.0 used in developing smart factories. Reprinted from [15], licensed under CC by 4.0.

As depicted in Fig. 1.1, one of the significant components in Industry 4.0 is machine vision, which [15] define as *"a computational capacity applied in new ways for current technologies to resolve real problems"*. Machine vision systems can be characterised as an integrated system of sensors, cameras, and computing power combined with software algorithms to provide sensory input to machines by extracting, processing, and analysing visual data [15]. In recent years, machine vision has gained popularity within the manufacturing industry and academia and has become the primary technology within intelligent and computer-integrated manufacturing [16]. In fact, according to Global Industry Analysts, Inc. [17], the global market for machine vision systems is projected to grow from its current value of US$8 Billion to US$16 Billion by 2026, rapidly growing at an annual rate of 12%. The increased popularity of machine vision systems can partly be attributed to the improved affordability of imaging components along with technological advancements, offering new capabilities that allow for more complex and advanced uses [18, 19, 20].

Unlike humans, machine vision systems are not limited to the visible spectrum. They do not suffer from fatigue, are impartial, and can achieve excellent reproducibility, efficiency, and accuracy. Moreover, machine vision systems facilitate automating previously manual processes, leading to an improved work environment, especially in the case of highly repetitive and physically demanding processes. Hence, machine vision systems can not only replace humans in processes that were traditionally human-operated but are

also able to extend human capabilities to perform tasks that were previously not possible. [16, 15]

In the context of Industry 4.0, machine vision systems have shown a clear potential to advance the quality assurance and quality inspection of manufacturing processes [21, 15]. Operating next to or as an integrated part of production processes, machine vision systems can acquire and automatically store information about each workpiece and manufactured part. This improves the traceability of the given manufacturing process and supports potential component redesign to minimise future manufacturing errors. In addition, machine vision can acquire data to permit continuous process monitoring and detection of imperfections and abnormalities early in production. This minimises the risk of required reworking, scrapping parts, and experiencing delays. [21]

The motivation for this PhD thesis is further underlined by the previously mentioned *Factories of the Future Roadmap*, which identifies machine vision applications as technological enablers or solutions that require research and innovation focus. The identified applications of machine vision are directly related to quality assurance and quality control in manufacturing processes and include the development and integration of in-line inspection techniques, on-machine calibration and metrology, and robust automation of processes with input uncertainty [22]. Note that some of the areas are overlapping. Similarly, a literature review by [23] presents several opportunities within quality assurance and quality control that could aid the adaptation of Industry 4.0. These include using machine vision systems for early failure detection and self-adaption techniques, in situ metrology and correction of manufacturing processes, and exploitation of new technologies for industrial inspection tasks. The authors of [23] further note that there is a general lack of use cases and case studies in the literature that provide real scenarios for use.

In summary, this PhD thesis, set within the context of Industry 4.0, aims to advance quality assurance and quality control of industrial manufacturing by exploiting the technological advances in machine vision. However, to ensure real-world justifiably and applicability of the potential solutions, the focus is placed on two selected industrial cases, which will form the foundation of the study.

1.2 Industrial Cases

The first case deals with automation and quality assurance of post-weld treatment as a part of the CeJacket project, introduced in Section 1.2.1. The second case deals with laser processing in manufacturing and is a part of the INTERLASE project, presented in Section 1.2.2.

1.2.1 CeJacket

The first industrial case takes offset in the CeJacket (Create Disruptive Solutions for Design and Certification of Offshore Wind Jacket Foundations) project. The CeJacket project focuses on developing more efficient manufacturing methods for producing jacket foundations for the offshore wind industry. The overall goal is to reduce the expenses of jacket foundations by 6-8 %, partly by improving the fatigue strength of the welded components to minimise material consumption.

A vast majority of machines and supporting structures contain welded assemblies, including offshore structures, farming equipment, and automotive components. However, it is widely accepted that welded joints have lower fatigue life than the base material [24]. This is partly due to local residual tensile stress concentrations in the weld's heat-affected zone (HAZ) as it cools down and solidifies [1]. Sharp notches at the weld toe[2] and other weld defects act as stress raisers, which form the basis for fatigue cracking [24]. As weld defects are expected, substantial safety factors should be employed in the design of the assemblies to prevent premature failure due to fatigue. However, this is not a feasible solution in the pursuit of material reduction for lighter and cheaper structures. One applicable approach is to use post-weld treatment.

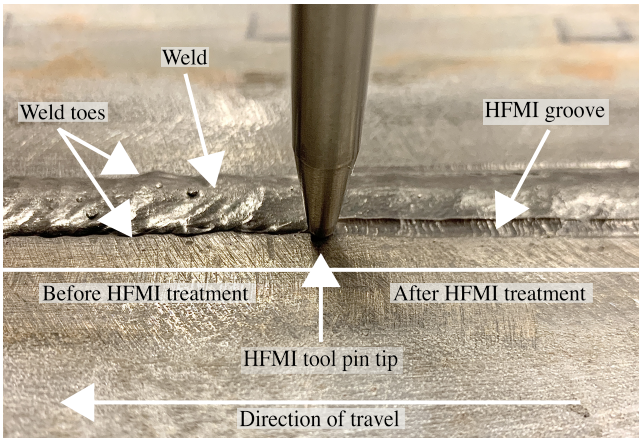

Fig. 1.2: A weld is shown before and after HFMI treatment. Note the transformation of the weld toe into a smooth and shiny groove. Reprinted from [1], licensed under CC BY 4.0.

Post-weld treatment is a group of methods applied to improve the fatigue strength and life of welded components by minimally altering the weld mechanically or thermally. One of these methods is high-frequency mechanical impact (HFMI) treatment, depicted in Fig. 1.2. HFMI treatment relieves the tensile stress concentrations, introduces compressive residual stresses in the treated

[2]**Weld toe:** the transition between the weld and base material.

area, and reshapes the notch into a smooth geometry by striking the weld toe region with a pin at a frequency above 90 Hz (cold forming) [25]. HFMI treatment has been shown to improve the fatigue life of welds significantly [25, 26, 27] even in cases of under- and over-treatment [28].

Industrial Challenges

The current and predominant approach to performing HFMI treatment is through manual operation based on a set of strict guidelines both in terms of execution and quality. The guidelines have been proposed by the International Institute of Welding (IIW) [29] and define a set of intervals for tool orientation and speed during treatment. However, the combination of a small tool pin tip radius and a vibrating and heavy tool makes the treatment guidelines challenging to adhere to, especially in the case of curvilinear welds. This was also indicated in a study by [30], in which it was concluded that operators affect the fatigue life scatter of HFMI treatment. As such, uncertainties in workmanship and quality assurance have led the industry to not fully accept the treatment. The Norwegian classification society, DNV, explicitly states that peening[3] cannot be recommended for use at the design stage for offshore steel structures [31]. Therefore, to expand the industrial applicability of HFMI treatment, effort must be placed on improving quality assurance, potentially aided by machine vision.

1.2.2 INTERLASE

The second industrial case is based on the INTERLASE (Integrated Laser Processes for Cost-Effective Prototyping and One-of-a-Kind Production) project. The INTERLASE project focuses on developing a flexible laser processing machine for one-of-a-kind manufacturing of sheet metal parts, following the principles of Industry 4.0.

Lasers are characterised by their ability to emit radiation in the form of light that can be precisely focused into a tiny spot. The result is a highly intensive and localised heat source, enabling precise and high-speed non-contact processing for numerous applications. Commonly, laser processing is done as separate processes, e.g. laser cutting and welding. This requires a lot of storage capacity and handling, as the processing time of laser cutting and welding differ. Complexity is added to the process as many sheet metal parts also need to undergo a forming step between the cutting and welding steps. The core idea behind the INTERLASE project, as presented in Patent A [9], is to combine a range of laser processes, i.e. laser cutting, welding, forming [32], and marking [33] in a single flexible machine. The purpose is to minimise handling, lead time, cost, and complexity. Moreover, manufacturing new and costly tools

[3] **Peening**: an overarching term covering HFMI treatment.

is not required in case of modifications to the part design. The overall goal is to reach a level of automation of the system, such that it is possible to input a CAD file of the part and a sheet metal blank, which is then laser processed directly into the final part with a minimum of operator intervention.

Industrial Challenges

Realising the presented system is challenging as laser processes are complex and inherently difficult to control [34]. Therefore, research within the field of quality assurance and quality control of laser processes is necessary to realise the presented system and to expand the industrial applicability of laser processing [34]. To limit the scope of the PhD thesis, a selected set of challenges are presented below in which machine vision systems could play an essential role.

Calibration of Galvanometric Scanner Systems One of the causes of positional errors in laser processing is the manipulation of the laser beam. The use of industrial robots is typically the most flexible approach for manipulating the laser beam, but the lack of positional accuracy and inferior dynamics of industrial robots limit the actual applications [35, 36]. Instead, galvanometric scanner (GLS) systems provide a means to precisely and rapidly manipulate the laser beam using rotational and translatoric optical components, as illustrated in Fig. 1.3 [2].

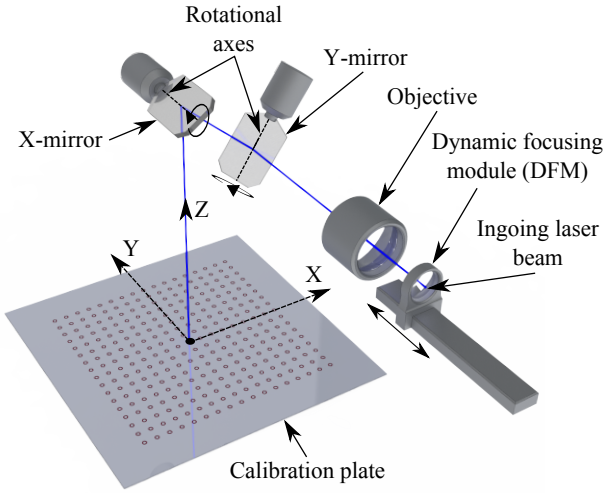

Fig. 1.3: Depiction of a simplified GLS system in the process of marking circular fiducials on a calibration plate. The primary components are represented, including the mirrors and the focusing module. Adapted from [2], licensed under CC BY 4.0.

However, GLS systems must be carefully calibrated to achieve the desired precision due to unknown thermal, mechanical, or optical defects [37, 38]. Mounting the GLS system on an industrial manipulator adds flexibility and extends the workspace of the scanner but complicates calibration as the relative positioning to the work plane is no longer constant [2]. Typically, the calibration and subsequent validation are performed based on a time-consuming procedure that requires tedious manual measurements prone to errors. This is unsuitable for a flexible and automated industrial laser processing setup. Machine vision could potentially be applied to provide the measurements required to calibrate the GLS system.

Pre-Process Inspection of Laser Marking Laser marking [33] is process used to produce marks for aesthetic or labelling purposes. As illustrated in Fig. 1.4, laser marking is highly sensitive to the surface absorption of the part. Even minor changes in the surface texture or reflectivity affect the amount of energy induced into the part's surface and, thus, the resulting colour [33, 39]. As a result, it is imperative to ensure that the surface is perfectly clean and homogeneous and free of scratches, contamination, and other defects.

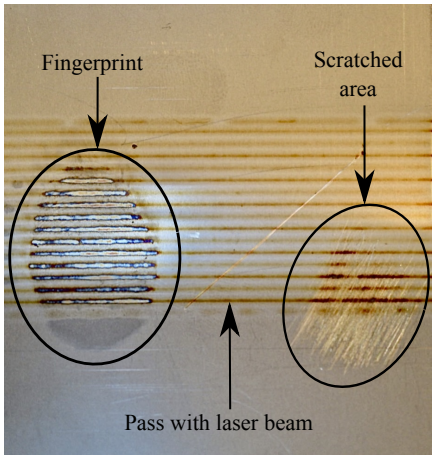

Fig. 1.4: Demonstration of how contaminants and scratches influence the surface absorption and, thereby, the resulting colour in laser marking. Each of the horizontal lines represents a laser beam pass. Observe the change in colour as the laser passes over the affected areas.

Industrially, the pre-process inspection is performed visually by a human operator, who cleans or discards the workpiece in the case of contaminants or abnormalities. However, humans are subject to bias and cannot determine the surface's reflectivity in the wavelength of the laser, limiting the accuracy of the inspection. Machine vision could potentially be utilised to perform the pre-process inspection to minimise human bias.

Quality Inspection of Laser Welding A process especially sensitive to positioning errors is laser welding. Calibrating the tool can reduce the positional errors of the laser beam. However, the use of a small laser spot size and the lack of filler material require not only strict tolerances for lateral positioning of the tool but also for the joint alignment and gap width to ensure fusion, adequate structural integrity, and satisfactory quality of the weld [40, 41]. The problem is particularly pronounced in automated production setups using six-axis robots when welding along complex 3D trajectories. Process monitoring using machine vision has shown a potential to acquire robust process data to support post-weld quality inspection or feedback control to reduce process variance; however, further research is required to fully exploit the potential [34].

1.3 Research Method

As this PhD thesis is related to engineering, the research can be characterised by the Design Science paradigm. Design Science was formally introduced in 1969 by Herbert Simon [42] and *'()...seeks to develop and design solutions to improve existing systems, solve problems, or even create new artefacts*[4] *that contribute to better human performance, whether in society or in organisations.'* [44, pp. 56]. As a result, Design Science can be referred to as Applied Science, emphasising the real-world usability of the generated knowledge to solve problems, commonly seen in engineering [45, 46].

Although problem-solving is the primary focus, Design Science does not aim to provide the optimal solution but rather a satisfactory solution. As stated in [47, pp. 27], an optimal solution for a simplified problem is unlikely to be optimal in the real world. Instead, the solution should be aimed at the particular class of problems, providing a generalised solution with broader applicability [48]. Defining a satisfactory solution depends on the involved stakeholders and the expected advancement of the existing solution from an academic and industrial standpoint [49]. In summary, [44, pp. 57] notes that the premise of Design Science Research is to be both rigorous, scientifically and pragmatically valid, i.e. have utility.

1.3.1 Design Science Research Methodology

Since the formal introduction in 1969, several approaches to performing Design Science Research have been presented. One variation is the research methodology proposed by [43], which was initially developed with Information Systems in mind but can be applied to other fields as well. The method proposed by [43] is essentially a consolidation of existing methods and consists of six steps. It has

[4] **Artefact:** generally characterised as an artificial object that offers a research contribution and is designed to solve a specific problem [43].

been chosen for this PhD thesis as it is highly suitable for research focusing on technological innovation and further emphasises the real-world applicability of the developed solutions by balancing theory and practice.

The below section is based on [43] and [50] and presents the Design Science Research Methodology originally proposed by [43] along with the required skills and knowledge at each stage.

1. **Problem identification and motivation:** A real-world problem is identified and defined, and the value of the solution and its implications are justified. Awareness of the problem's current state and its solution's relevance must be determined.

2. **Define the objectives for a solution:** The solution's objective is derived from the problem definition, considering what is possible and feasible and the anticipated contributions from the solution. To achieve this, knowledge of existing solutions and their performance is required.

3. **Design and development:** The actual artefact is created, e.g. in the form of a model, method, or tool to meet the objectives from the previous stage. As such, this stage relies on theoretical and fundamental knowledge of the field.

4. **Demonstration:** The created artefact is applied to demonstrate its performance in carrying out the defined objectives to solve the identified problem, e.g. through case studies, simulations, or experimental studies. Therefore, this step requires practical experience to utilise the developed artefact.

5. **Evaluation:** The results from the demonstration are evaluated to determine how the created artefact solves the identified problem by comparing the defined objectives to the observed results. Insufficient performance of the artefact can lead to reiteration of step three to refine the solution depending on the nature of the research. Therefore, this step requires knowledge of how to analyse the results.

6. **Communication:** The problem, its significance, and the created artefact, along with its design, performance, application, and contribution, are communicated to researchers and other stakeholders who might benefit from the research, such as industry professionals. One typical approach is to use scholarly research publications, which require disciplinary knowledge.

Although the activities are structured sequentially, the method proposed by [43] differs from other Design Science Research methods such as [48] in its flexibility. It allows the completion to be done starting from almost any

step and in any order, depending on the initiation of the research. As such, a problem-centred approach would start with the first step, typically triggered by an observed problem. Instead, an objective-centred solution, where an industrial or research need to develop an artefact has arisen, would start from the second step. Similarly, cases exist where the research could be initiated from steps three and four, respectively, a design- and development-centred approach and a client-/context-initiated solution. [43]

This PhD thesis takes an objective-centred approach initiated by the problems derived from the two industrial cases. As such, the PhD thesis uses the identified problems and knowledge of related works to define the research objectives, step two. Additionally, the PhD thesis creates the theoretical foundation of machine vision as a prerequisite for step three. The published papers associated with the thesis constitute the development of artefacts (step three), demonstration (step four), and evaluation (step five) to solve the identified problems, adhering to the principles of creating generalised solutions with real-world applicability. Step six is shared among the PhD thesis and the published papers, as the thesis communicates the summarised contributions, whereas the published papers communicate the specific contributions associated with each created artefact.

Note that as the thesis outline presented in the following section is derived from the applied research methodology, it exemplifies the use of the Design Science Research (DSR) methodology in the context of this thesis.

1.4 Thesis Outline

The PhD thesis is formatted as a collection of four published papers that constitute the main body, supported by four additional papers and two patents. Note that the PhD thesis can be read without reading the associated papers, although the papers provide additional details and background not present in the PhD thesis. The PhD thesis is divided into three main parts: introduction, findings, and appended papers, as presented below.

Part I: Introduction

Chapter 1 Project Background
The chapter introduces the background and motivation for the PhD thesis and the two industrial cases. From the industrial cases, a set of real-world problems have been identified.

Chapter 2 Related Work
This chapter presents a comprehensive literature study on post-weld treatment and laser processing conducted to examine existing solutions and identify research gaps.

Chapter 3 Research Questions and Objectives
This chapter formulates several research questions and objectives based on the identified problems and research gaps.

Chapter 4 Fundamentals of Machine Vision Systems
This chapter serves as the theoretical introduction to the findings and presents the fundamentals, i.e. the overall approach, challenges, and considerations, related to the design and development of machine vision systems.

Part II: Findings

Chapter 5 Summary of Papers
This chapter presents the machine vision systems developed to address the research questions and objectives. The findings are presented in the form of extended abstracts of the papers constituting the main body of this thesis. Lastly, the academic and industrial implications of each paper are discussed. Adhering to the principles of Design Science, the artefacts have been created to provide substantial research contributions while yielding generic, flexible, and robust solutions with wide industrial applicability.

Chapter 6 Concluding Remarks
This chapter concludes the study. The research contributions are summarised, the implications are discussed, and future work is presented.

Part III: Papers

Paper A Development of an Automated System for Adaptive Post-Weld Treatment and Quality Inspection of Linear Welds
This paper explores the application of machine vision to develop an automated system for adaptive post-weld treatment and quality inspection of linear welds. By relying on 3D scans and finite differences, the weld features are extracted to tailor the treatment to each weld and to evaluate the treatment, thereby substantially enhancing the process stability and overall quality assurance.

Paper B Three-Dimensional Scanning Applied for Flexible and In Situ Calibration of Galvanometric Scanner Systems
This paper proposes a generic, flexible, and in situ methodology for calibrating galvanometric scanner systems to improve the quality assurance of laser processing. The proposed method is based on measurement data from a 3D laser scanner combined with a simple

neural network to predict and correct scan field distortion, such that positional errors are reduced when processing.

Paper C **A Novel Method for Approximating Local Changes in the Surface Absorption for Laser Marking Using 3D Laser Scanning**
This paper studies the use of machine vision to approximate local changes in the surface absorption for laser marking caused by surface abnormalities. The method exploits the backscatter intensities from a 3D laser scanner combined with a reflectance model to identify areas of varying surface absorption, serving as quality control.

Paper D **Quality Inspection System for Robotic Laser Welding of Double-Curved Geometries**
This paper proposes an in-line system for detecting variations in the laser welding trajectory of double-curved geometries. The method relies on a 2D machine vision approach that combines common image processing techniques with a Kalman filter aided by a neural network to enhance quality control.

Chapter 2

Related Work

This chapter summarises the related works within quality assurance and quality control of the two related industrial cases. First, related works within automation and quality control of HFMI treatment are presented, and the research gaps are highlighted. Secondly, the related works in calibration and monitoring of laser processing are presented and examined.

2.1 Automation and Quality Inspection of Post-Weld Treatment

The presentation of the related work in the following section is based on Paper A [1].

Automating post-weld treatment, particularly high-frequency mechanical impact (HFMI) treatment, has shown substantial potential in several areas. First, by removing operator bias from the treatment and enhancing control of the process parameters, the quality assurance is improved compared to the manual application of the treatment [51]. Secondly, automating the HFMI treatment improves the work environment considerably, as the operator no longer has to operate the heavy and vibrating HFMI tool directly. Lastly, clamping the tool, e.g. when mounting it on a robot, is itself expected to lead to a more efficient treatment. The improved efficiency results from the scatter band of compressive forces being 50% narrower compared to manual operation, while the impact force is maintained or even improved [51, 52, 53].

However, few solutions have been proposed for performing automated post-weld treatment, specifically HFMI treatment, and these are limited to linear welds following predefined linear trajectories [54, 55]. Following a strict linear trajectory has resulted in a large scatter in the treatment quality and degradation of the treatment quality [56, 55]. This outcome is believed to be a

consequence of the robot's failure to adapt to the complexity of the actual weld toe. The challenge in automating HFMI treatment thus lies in identifying the areas to treat and adapting the treatment specifically to each unique weld. To further improve quality assurance and quality control, attention must be paid to post-treatment quality inspection. In both cases, detailed knowledge of the surface geometry is essential, underlining the potential for machine vision.

2.1.1 Quality Inspection

As stated in Section 1.2.1, IIW [29] define a set of general recommendations for performing quality inspection of post-weld treatment. The recommendations consist of quantitative measures, shown in Fig. 2.1, and qualitative measures, as further detailed below.

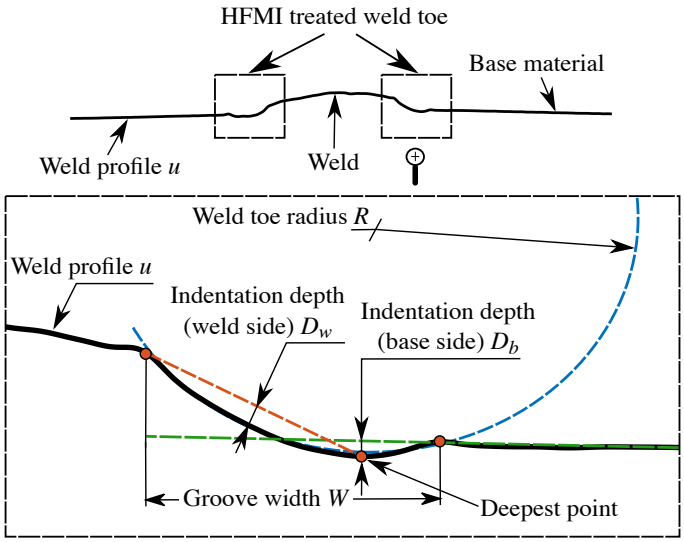

Fig. 2.1: Definition of quantitative measures for HFMI treatment. Adapted from [3], licensed under CC by 4.0.

Qualitative Measures

The original fusion line observed as a think crack-like feature, must not be visible in the groove. Additionally, the groove must be continuous, shiny and smooth with no signs of individual indenter strikes or breaks along the line [29]. For the trained eye, there is a clear distinction between under-, over- and properly treated welds [54]. Incorrect application, such as excessively high coverage rates, i.e. low speed or two passes, may be observed as flaking type damage [56]. Similarly, directing the indenter excessively in a single location

may further lead to crack-like features at the edges of the groove, which should be avoided [54].

Typically, visual inspection is used to evaluate the quality measures of the groove, commonly using a simple magnifying glass. From the literature study, no machine vision solution has been proposed to evaluate the qualitative measures of HFMI treatment. However, to limit the scope of the study, focus is placed on the quantitative measures, as presented below.

Quantitative Measures

As noted by [29], the indentation depth of the groove D_b, measured from the base side, is an outstanding indicator for the level of treatment. A minimum indentation depth D_b of 0.1 – 0.2 mm is required to ensure adequate treatment. However, as the yield stress and indenter size vary based on the material and weld, the optimal indentation depth D_b lies in the range of 0.2 – 0.6 mm. Conversely, the groove width W should be in the range of 3 – 6 mm with the groove positioned so that 25% – 75% of its width is in the weld material. Its positioning is determined by comparing the weld toe's original location with the created groove's position ϵ. Other notable quantitative measures include the weld toe radius R (the radius of the created groove) and the indentation depth on the weld side D_w. [29]

Currently, the industrial approach to evaluate the quantitative measures relies on simple manual gauges applied at several points along the treatment. However, the gauges employed for quality inspection of HFMI treatment have proven unreliable as they are known to contribute to the measured treatment variance. As noted by [57], the gauge is responsible for nearly 60% of the total variance in measuring the depth of undercut and throat thickness in untreated welds. According to [58], a standard requirement outlines that the measurement system itself should contribute with no more than 9% of the total variance.

Numerous researchers have proposed non-contact methods for quality assurance of untreated and treated welds. This includes [59], who proposed a method to determine weld quality by classifying weld defects, i.e. incomplete fusion and inadequate penetration. The presented method relies on state vector machine (SVM) classification of 3D images reconstructed from 2D images utilising the shape-from-shade (SFS) algorithm.

On the other hand, [58] significantly reduced measurement variation compared to manual methods by employing a laser line scanner to perform quality control and quality assurance of welds. Other methods have utilised laser scanning to evaluate the weld profile and identify weld defects, applying techniques like RANSAC fitting [60] or second-order differentiation [61] to extract feature points. For quality assurance of post-weld treatment using non-contact methods, the current state-of-the-art involves manually evaluating the

quantitative measures based on 3D scans. An example is [55], who successfully identified the treatment level, i.e. under-, over-treated or properly treated. Hence, it has been demonstrated that machine vision can provide sufficient data for quality assurance. However, further research in machine vision for automated evaluation of the quantitative metrics is required to improve the quality control of weld-toe treatment.

2.2 Calibration and Monitoring of Laser Processes

Laser processing has gained popularity in the manufacturing industry in the recent years due to its flexibility, low thermal distortion, and high productivity. However, the inherent complexity and sensitivity of laser processing limit the number of actual applications. To fully exploit the potential of laser processing, research efforts have been placed on quality assurance and quality control; specifically calibration, monitoring, and automation of laser processing [34].

To limit the scope of the study, the focus here is placed on the industrial challenges of laser processing presented in Section 1.2.2. More specifically, calibration of galvanometric laser scanner (GLS) systems, pre-process inspection of laser marking, and quality inspection of laser welding. Below, the related works within each of the presented topics are summarised.

2.2.1 Calibration of GLS systems

The presentation of the related work in the following section is based on Paper B [2]. The conventional approach to calibrate galvanometric laser scanner (GLS) systems is to construct look-up tables (LUT) that use experimental data to describe the relationship between the joint space[1] and the task space[2] [62, 63, 64]. However, constructing look-up tables is computationally heavy and sensitive to the properties of the underlying experimental data [65, 37]. Other authors have proposed comprehensive physical models that describe the joint and task space relationship. These models rely on exhaustive parameter fitting using optimisation based on accurate experimental data and extensive prior knowledge of the optical and mechanical design of the GLS system [37, 66, 67, 38]. As a result, model-based methods are computationally heavy, known to suffer from non-convex optimisation problems, and sensitive to slight changes in the hardware design, limiting their industrial application. Instead, [68], [65], and [69] have applied data-driven methods that rely on artificial networks to build grey/black box models. These methods provide increased flexibility with limited mathematical modelling and dependency on the hardware configuration and have been shown to outperform LUT-based

[1] **Joint space:** defined by the rotations of the mirrors and the position of the focusing module.
[2] **Task space:** the Cartesian space of X, Y, and Z coordinates.

and model-based approaches [69]; however, data-driven methods are yet to be applied for calibration of GLS systems for materials processing.

The experimental data form the foundation for most calibration approaches as it permits visualisation of the GLS system's positional errors. Typically, the experimental data is acquired by laser marking a specific pattern on a calibration plate, which is then measured to determine the actual Cartesian positions of the GLS system. Commonly, the measurements are performed externally, making them difficult to automate, prone to errors, and time-consuming [64]. However, as data-driven methods require accurate and high-density measurements to achieve satisfactory calibration accuracy, the measurements must be performed automatically and in situ to avoid introducing errors if the calibration plate is moved.

Several authors have proposed to acquire the experimental data automatically and in situ using co-axially coupled machine vision systems [64] or in an off-axis configuration [67]. However, these solutions require significant modifications to the existing optical configuration or, simply, assume a constant relative orientation between the GLS system and the work plane [67]. Nevertheless, as stated in Section 1.2.2, the constant orientation does not apply to robot-manipulated GLS systems. As such, existing methods based on machine vision are unsuitable for calibrating robot-manipulated GLS systems, but the use of machine vision has shown potential and should be investigated further.

2.2.2 Pre-Process Inspection of Laser Marking

The presentation of the related work in the following section is based on Paper C [3].

The literature generally presents three approaches to estimate the surface absorption of material in its solid state for materials processing: purely theoretical or through indirect or direct measurement techniques [70]. The classic theoretical methods include the Drude model [71] and the Hagen and Rubens model [72], which require accurate information about parameters such as oxidation, surface roughness, contamination, and material properties. On the other hand, indirect measurement techniques use computational models to evaluate the surface absorption based on the surface roughness and temperature, angle of incidence, and light intensity [73, 74, 75, 76]. Consequently, indirect measurement techniques outperform the purely theoretical methods but with increased computational complexity [70]. However, accurate knowledge of the extensive parameters is rarely available for the workpieces in an industrial setup, making the theoretical and indirect measurement techniques unsuitable.

Instead, direct measurement techniques rely, as the name suggests, directly on experimental measurements and provide an accurate and straightforward approach to estimating surface absorption. These can be divided into two categories: methods that directly measure absorption based on a temperature

rise in the material (calorimetry methods) and those that indirectly evaluate absorption through the radiative properties of the surface (radiometric methods), i.e. reflectance and emission [70, 77]. Calorimetry methods are relatively simple compared to radiometric methods but cannot estimate surface absorption locally. The authors of [78] used integrated sphere spectrophotometry, a radiometric method, to determine the absorption of stainless steel, providing simple and highly accurate measurements. However, this method is additionally unsuitable for flexible production setups, as each sample requires placement inside the integrated sphere, limiting the physical size of the sample.

Alternatively, [79] attempted to estimate the reflectance properties of a surface from range and brightness images based on bidirectional reflectance models. The primary purpose was to distinguish between specular and Lambartian surfaces, e.g. for defining regions in a human face. Other authors have used machine vision, i.e. LiDAR scanners, to remotely determine surface roughness and characteristics of urban building materials based on the estimated surface reflection [80, 81]. In both cases, the focus was not on estimating the surface reflectivity of components for laser processing.

In summary, numerous theoretical models, as well as indirect and direct measurement methods, have been developed for estimating surface absorption. Although, no existing method can estimate the surface absorption locally as a part of a flexible laser marking setup, i.e. capable of handling variation in part size and geometry. This limitation hinders the ability to locally control the induced heat in the material, a prerequisite for a stable laser marking process and a quality outcome. However, as machine vision has demonstrated an ability to estimate the surface reflection of building materials remotely, it could potentially be applied to estimate the local surface absorption for laser marking.

2.2.3 Quality Inspection of Laser Welding

The presentation of the related work in the following section is based on Paper D [4].

In recent years, extensive research has been conducted on seam tracking, joint monitoring, and real-time control of the laser welding process. The majority of studies in this area have employed machine vision systems containing similar key components, such as an imaging sensor, a strong light source characterised by a particular wavelength and a narrow band-pass filter, often combined with a neutral density filter [82, 83, 84]. The authors of [85] and [86] used this approach, along with common techniques like BLOB analysis and edge detection, to study the laser welding process of single-curved welds. They successfully mapped and monitored 3D butt joints, tracked the laser focal point, and corrected joint misalignment in real time. To enhance the reliability of vision-based laser welding monitoring systems, [40] integrated a Kalman filter for joint gap estimation in linear welds to aid in instances of image processing

failure. This method not only strengthened the reliability of the monitoring system but also optimised the computation time relative to other methods. [87] also focused on 2D welds and enhanced the reliability of the monitoring by employing a Kalman filter combined with a radial basis function neural network to account for noise.

As an alternative to employing machine vision, [88] and [89] utilised a photodetector to monitor the laser welding by capturing light emitted from the process. This enabled the creation of mathematical models to enhance control over deep-penetration welds by adjusting the process parameters (e.g. velocity and laser power), improving the overall weld quality. However, although model-based approaches are less sensitive to the welding trajectory as they measure the reflected energy, they cannot quantify positional inaccuracies.

In summary, existing machine vision systems have not been developed to determine the positional deviations when welding complex geometries that require double-curved welding trajectories, limiting their industrial application. Although machine vision has demonstrated a strong potential for process monitoring, further investigation is needed to adapt it to complex welding trajectories.

Chapter 3

Research Questions and Objectives

This chapter presents the two research questions and associated research objectives derived from the problem definition and the related work. The aim of the research objectives is to address the research questions through the industrial cases.

Derived from the industrial cases and the presented related works, it is apparent that machine vision has a substantial potential to advance the quality assurance and quality control of industrial manufacturing, specifically post-weld treatment and laser processing. This leads to the two research questions:

> **RQ1**: How can machine vision be applied to advance the quality assurance of manufacturing processes in the context of the industrial cases?
>
> **RQ2**: How can machine vision be applied to advance the quality control of manufacturing processes in the context of the industrial cases?

The ISO 9000 standard defines quality assurance as providing confidence that the quality requirements will be fulfilled, e.g. by improving the manufacturing process itself [90]. Therefore, the use of machine vision for automation and calibration of manufacturing processes has a substantial potential to improve the robustness, reproducibility, and overall quality of a given process, aiding in enhancing the quality assurance of the process.

Following the given definition of quality assurance, the research objectives presented below directly address **RQ1** through research in applied machine vision.

> **RO1.1:** Investigate the application of machine vision to extract the location and geometry of the weld toe for automated and adaptive post-weld treatment.

RO1.2: Develop a flexible and generalised methodology for automated calibration of galvanometric laser scanner (GLS) systems using machine vision.

Conversely, quality control, defined by the ISO 9000 standard, focuses on fulfilling requirements. As such, quality control prevents any undesirable change in quality through monitoring activities to act on any deviations to correct the overall quality of the product, i.e., by adjusting process parameters or discarding the produced product. Depending on the expected outcome of the quality control, capability of the applied sensor and consequence of failure, the monitoring activities can be placed before, during, and after the given process [90]. Note that quality assurance and quality control are closely related and sometimes overlap. Machine vision is highly beneficial in improving quality control through process monitoring and inspection of manufacturing processes by detecting and correcting process deviations.

Following the given definition of quality control, the research objectives presented below directly address **RQ2** through research in applied machine vision.

RO2.1: Research the use of machine vision to evaluate the quantitative metrics for automated quality control of post-weld treatment.

RO2.2: Explore the potential of machine vision to identify local variations in surface absorption for improved quality control of laser marking.

RO2.3: Study the application of machine vision for quality inspection in laser welding of double-curved geometries to enhance quality control.

Chapter 4

Fundamentals of Machine Vision Systems

This chapter presents the overall approach, challenges, and considerations related to the design and development of the machine vision systems proposed in Chapter 5 and Part III. Hence, this chapter partly serves as an introduction to the associated papers by providing the fundamentals and insight into some of the key methods applied in the context of this thesis. The purpose is to further the understanding of the developed machine vision systems and the challenges therein.

4.1 Design and Development of Machine Vision Systems

Machine vision belongs to the field of systems engineering, but whereas classic computer vision constitutes the system intellect, machine vision can be characterized as the system body or the practical realization of computer vision techniques for solving industrial problems [91]. As such, machine vision deals with both hardware and software and is, therefore, a complex and interdisciplinary topic involving subjects from optics to computer science and mechanical engineering. With an emphasis on industrial application, machine vision can generally be characterized as a methodology that applies an image-capturing device for data analysis and interpretation to complete a wide range of industrial tasks. [92, 91]

Designing a robust and reliable machine vision system is a complex discipline that requires careful consideration. Each machine vision application is based on a detailed analysis of the system requirements, and thus each system is specifically designed for the task at hand, e.g. focusing on robustness, accuracy, or reliability. Based on the specified system requirements, [93] notes

the importance of considering the exact type of information that should be retrieved and how this is translated into a decision and future action. For example, in the case of process monitoring, questions such as *"What should be monitored to determine the state of the system?"*, *"How should the hardware and software components be implemented?"*, and *"How is a faulty system defined?"* should be answered [93]. [94] has summarized several key points in the design of an optimal machine vision system:

- **Application justice:** The machine vision system must comply with the technical and financial requirements. Moreover, it should be considered whether the system improves the privacy, safety, quality, robustness, or reliability of current systems. In some cases, the complexity of the machine vision task does not justify the development and use of an automated machine vision system.
- **Budget consideration:** An optimal balance between cost and performance must be achieved based on the budget and requirements of the system. However, achieving a highly effective and accurate machine vision system commonly comes at a performance cost, which involves expensive components, training of operators, and possible cost of data storage.
- **Systematic consideration:** The system should be developed and integrated for industrial use. Robustness, external communication, and control by robots or a central logic controller, ease of use for the operator, universal compatibility, level of intelligence, and use of commercially available solutions should be considered.
- **Scene consideration:** Considerations related to how the scene affects the data acquisition and the resulting constraints are essential. For most machine vision techniques, lighting conditions play a significant role. However, the surrounding environment, movements of the sensor and object, vibrations, position, geometry, surface preparation, and part material should not be neglected.

The above considerations should result in a clear set of technical requirements for the system, including budget, reliability, accuracy, operating conditions and constraints, as well as limitations.

4.1.1 Challenges in Industrial Integration

Designing and developing machine vision systems for industrial integration is not without its issues. [21] and [95] present some challenges and barriers related to integrating machine vision systems in the manufacturing industry that have been considered in developing the solutions proposed in this PhD thesis. The challenges and barriers are summarised below:

- **Hardware limitations:** Factors such as camera frame rate and limited data transfer and processing rates can pose challenges, e.g. for high-speed in-process inspection. Moreover, limitations in the spatial resolution, as noted in Section 5.3, depth of field, and field of view may cause issues, e.g. with large variations in part size or for highly accurate applications.
- **Noise:** Unstable environments with changes in humidity, temperature, and lighting conditions can alter the system's operating conditions, resulting in acquisition noise. Similarly, vibrations, variations in surface texture, and reflective surfaces may cause outlier formation and inaccurate data, as demonstrated in Section 5.2 and Section 5.4.
- **Complex parts:** In the case of complex part geometries, acquiring data from a single position may not be enough. As such, careful planning of the data acquisition strategy may be required to avoid occlusions and to capture hidden surfaces to ensure a complete representation of the geometry. This potentially requires stitching multiple views, as presented in Paper E [5], which, in itself, is a challenging problem.
- **Harsh environments:** High temperatures, vibrations, or even light pollution, as shown in Section 5.5, are typical in manufacturing but difficult for machine vision systems, which may result in noisy data or equipment failure.
- **User-depended constraints:** The operator skill and experience may significantly affect the resulting outcome of the given machine vision system as some systems rely on operator input, e.g. for calibration. This is especially evident when comparing the outcome of identical machine vision with different operator setups. Therefore, operator training and excellent practical guidelines are essential to ensure consistent results and correct operation.

The exact choice of the components is related to the specific application and should factor in the above considerations and challenges. Therefore, these considerations and challenges have acted as a basis for choosing the components and approaches applied in the developed solutions, as further detailed in Chapter 5 and the associated papers, Part III. Note that in the following sections, when a reference is made to the developed machine vision systems, it refers to the machine vision systems developed as part of the PhD.

4.2 Architecture of Machine Vision Systems

The general architecture of a machine vision system varies throughout the literature [94, 96, 93, 15, 91], where the main difference lies in the number of steps and the contents of each step. However, assuming the digitization is performed within the acquisition device, a typical machine vision system consists of the four steps which leads to an action carried out by the manufacturing system. Fig. 4.1 illustrates the general architecture, key components, and methods applied in the developed machine vision systems.

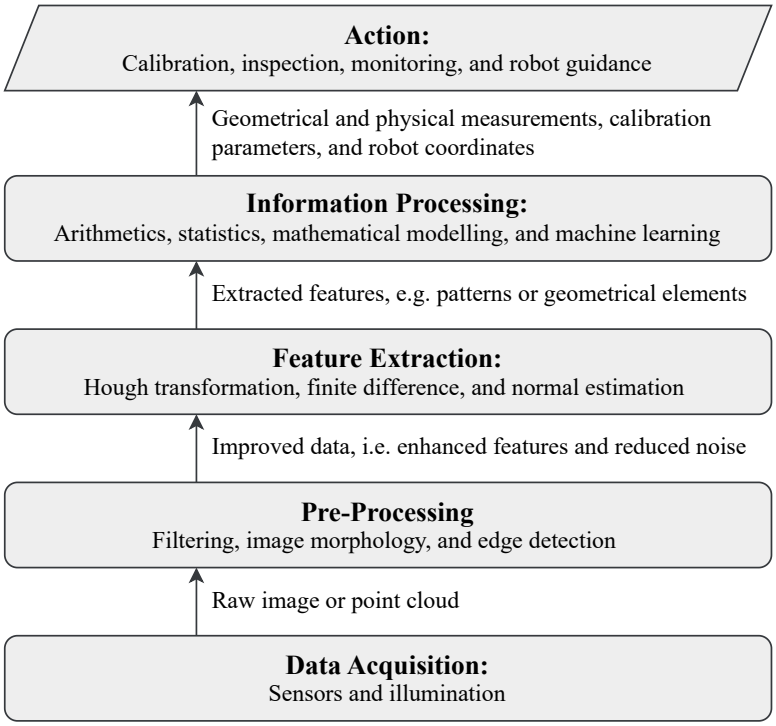

Fig. 4.1: Steps, key components, and methods of the developed machine vision systems.

Hence, the following sections are based on Fig. 4.1 and give a general introduction to the fundamental steps as well as key components and methods used in the design and development of the machine vision systems presented in Chapter 5. Emphasis is placed on 3D vision, which is the primary method in this PhD thesis. However, representing 3D point clouds using the depth information as pixel intensities as 2D images permits using the methods initially developed for 2D, significantly expanding the number of available methods for processing. This approach has been applied in a number of the developed methods, such as those presented in Paper B [2] and Paper C [3]. Thus, the

methods related to 2D machine vision are also introduced. Note that in the below sections, the term "image" can refer to both the classical representation of an image, but also as 3D data represented as a range image.

4.2.1 Data Acquisition

The foundation of a machine vision system is acquiring data. The raw analogue electrical signals the imaging sensors receive are digitized to form a digital image or point cloud. The quality and the amount of acquired data are essential for the succeeding operations as recovering missing data and filtering noise is difficult, time-consuming and, in some cases, even impossible.

The capabilities of the resulting system are hence highly impacted by the data acquisition setup. The typical setup, and those applied in the context of this PhD thesis, consist of three main physical components: optical illumination, an image acquisition device, and a computing unit depending on the specific application domain [16, 94]. However, countless camera filters, lighting, optics, and sensor options exist. These provide a wide design space, which can be exploited based on knowledge, conceptualization, and careful consideration of the system requirements. In fact, a well-designed acquisition setup and methodology can limit the succeeding data processing to trivial operations simply due to the high quality of the raw data. In the literature, there is a broad agreement that effort applied in the early stages of designing and developing machine vision systems is well worth the resources [96, 91, 16, 93]. Noise stemming from internal factors such as digitization of the image, the electronic components, and the transmission circuits of the acquisition device is, however, challenging to avoid [16].

Traditionally, machine vision has relied on acquiring 2D data, providing a flat image of the given scene. Therefore, 2D machine vision is highly suitable for applications that do not require depth information and rely upon high contrast and colour, such as reading QR or bar codes, classification, and in-plane inspection and measurement tasks. The inherent simplicity of 2D vision allows for cost-effective, compact, and flexible solutions for various applications, as shown in Section 5.5 and Paper H [8].

Instead, 3D data acquisition methods serve to obtain 3D geometrical information. Previously, acquiring 3D data was limited to contact-based methods that physically touched the surface there were measuring. With technological developments, it is now possible to acquire dense 3D data with a high accuracy and acquisition rate using non-contact optical methods. As a result, 3D vision is suitable for applications that require dimensionally stable depth information, such as robot guidance (Section 5.2), calibration (Section 5.3), inspection tasks (Section 5.4 and Section 5.5), and surface reconstruction (Paper E [5]). [15, 97, 20]

4.2.2 Pre-Processing

The pre-processing stage deals with improving the quality and accuracy of the raw data by denoising, enhancing features, and by applying geometric transformations. Filtering background noise or unwanted reflections, enhancing edges and boundaries, or isolating areas of interest are typical examples of pre-processing. Therefore, the pre-processing stage forms the foundation for the data analysis and can often significantly improve the basis for the succeeding operations. Ensuring that surfaces remain smooth, preserving edges, protecting textures, and avoiding introducing new objects are common issues in pre-processing images and point clouds. Furthermore, achieving or maintaining a uniform distribution of the points in point clouds can be challenging [98, 99].

In 2D image processing, one common pre-processing approach is to apply the common neighbourhood processing methods that operate in the spatial domain, i.e. directly on the individual pixels (point operations) or a group of pixels (group operations). These include filtering operations and basic threshold or morphological operations, which can be used to remove noise or enhance image features based on geometric structures [98, 16]. Additionally, both threshold and morphological operations can be used to perform segmentation to isolate areas of interest to ease subsequent processing. Hence, in Section 5.3 and Section 5.5, the Canny edge detector is used as a pre-processing step to isolate and enhance edges and in Section 5.3 followed by morphological operations to isolate and enhance circular patterns specifically.

In 3D point cloud processing, statistical methods are the earliest classical approach for denoising and outlier removal in 3D point clouds and, therefore, widely applied, researched, and implemented into libraries [99]. Statistical methods work by exploiting the spatial distribution of the point cloud. As a result, outlying points are removed by exploiting the spatial distribution evaluated using Euclidean distances in Paper E [5]. Another approach is to apply filtering techniques from signal processing, as demonstrated in Section 5.2. Here a 2D median filter is used to remove outlier noise, while a Butterworth filter is applied to smooth the data further, proving to be an effective approach.

4.2.3 Feature Extraction

As with the pre-processing methods, many methods exist for extracting features from images and point clouds. The choice of method depends on the specific application, its technical requirements, and the information to be extracted. [100] defines feature extraction as transforming the input data into a set of features that allows for extracting relevant information to perform a given task. A suitable image feature can be defined by discriminating information such that the given feature can be reliably distinguished from other objects in or across

images or point clouds. However, feature extraction is a challenging problem, as features are inconsistent and sensitive to various factors, such as scale, noise, perspective, and illumination. In general, feature extraction methods can focus on local or global features, depending on the specific application [101, 100].

Local features are described as distinctive patterns or geometrical objects, such as edges, corners, or normals in the image or point cloud. A suitable local feature is defined as being localizable, distinctive, and repeatable and can be used for registration, defect detection, and industrial dimensional and geometrical inspection [102]. Section 5.2 shows the application of local features, as the gradient and curvature across the point cloud are evaluated across the point cloud using finite differences to identify the sharp edges that form the weld toes. Similarly, in Section 5.4, the normals are computed across the surface, which is later used as an input to the bi-directional reflectance distribution function (BRDF).

Instead, global features are usually topological and refer to descriptive characteristics that capture information about the entire image or point cloud. Global features can represent colour, texture, or shape information through a feature vector. However, their limitations include sensitivity to noise and variations in illumination and failure to identify essential features [101]. Specifically, in Section 5.3, the Hough transform is applied to extract the shape of circular fiducials, while the Hough transform is applied to extract lines in Section 5.5.

4.2.4 Information Processing

In the last step of the developed machine vision systems, the extracted features are processed, permitting the system to make a decision and, subsequently, carry out an action on the physical system.

As demonstrated in the case of this PhD thesis, the information processing can be performed using various methods, such as simple arithmetic to compare measurements (Section 5.5), statistics for quality control (Section 5.2), mathematical modelling to determine surface reflections (Section 5.4), and machine learning to predict and correct positional deviations (Section 5.3). Therefore, the resulting output consists of geometrical and physical measurements, robot coordinates or calibration parameters, depending on the specific application.

Application of AI in Industrial Machine Vision

The use of AI for image analysis, e.g. for pre-processing, feature extraction, and information processing, is rapidly emerging due to the increased availability of large training data sets coupled with advancements in computational power. This has improved the industrial adaptation of AI to perform complex machine vision tasks.

However, there are still some concerns related to the industrial application of AI in machine vision. As stated by [103], data availability is the primary challenge. In many cases, research on AI is done under the assumption of sufficient data being available for training the models. However, acquiring data that represents the varying conditions, settings, and configurations of a real-world manufacturing system may be connected with substantial financial and operational costs. Similarly, labelling the acquired data for training models may be time-consuming and rely on expertise and domain knowledge, depending on the specific application. Note that the quality of the network output is no better than its input. Another concern is related to the lack of transparency in black-box AI models, which stems from the difficulties in validating the decision process of the models. [103, 91]

Therefore, as this PhD thesis deals with complex manufacturing processes with a high degree of input uncertainty and process variance, AI-based image analysis does not have the appropriate technological readiness level to be applied to the context of this study. However, in this PhD thesis, machine learning has been applied for function approximation, as presented in Section 5.3 and Section 5.5. In addition, there are aspects of this study that could potentially benefit from future research into the use of AI, as presented in the future work, Section 6.3.

Part II

Findings

Chapter 5

Summary of Papers

This chapter presents the developed solutions and summarises the findings from the research questions and objectives formulated in the previous chapter. The developed solutions have been documented in the four papers, Part III, that constitute the main work of this PhD thesis. The findings of each paper are presented in the individual sections below as extended abstracts, along with the resulting implications.

5.1 Research Classification

This PhD thesis investigates the use of machine vision to advance the quality assurance and quality control of industrial manufacturing by addressing the research questions and objectives given in Chapter 3. As previously stated in the motivation for the thesis, Chapter 1, machine vision systems offer advantages beyond human capabilities. Machine vision systems are not constrained to the visible spectrum or suffer from fatigue while offering impartiality as well excellent reproducibility, efficiency, and accuracy [16, 15]. This allows machine vision systems to replace humans in previously manual processes or simply extend human capabilities to perform previously impossible tasks.

As a result, efforts to advance quality assurance and quality control using machine vision can roughly be classified into two categories based on the approach: those that aim to replace human involvement and those that aim to extend human capabilities. This distinction is illustrated in the classification scheme, Fig. 5.1, further depicting each published paper's contribution.

Hence, the presented classification scheme illustrates the relationship between the associated papers as well as the PhD thesis' contribution to advancing quality assurance and quality control.

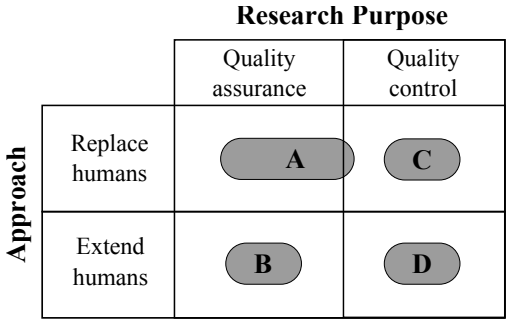

Fig. 5.1: A classification scheme presenting the relationship between the associated papers, denoted by the bold letters, and how they contribute to advancing the quality assurance and quality control of manufacturing processes. Note that the placement of the individual contributions is based on interpretation, as defined using their primary approach and purpose.

5.2 Paper A: Adaptive Post-Weld Treatment and Quality Inspection of Welds

The first paper in this thesis, Paper A [1], is titled "Development of an Automated System for Adaptive Post-Weld Treatment and Quality Inspection of Linear Welds". The paper has been submitted and published in *The International Journal of Advanced Manufacturing*, Springer, 2022.

The paper relates to research question **RQ1** and **RQ2** by addressing research objectives **RO1.1** and **RO2.1**:

> **RO1.1:** Investigate the application of machine vision to extract the location and geometry of the weld toe for automated and adaptive post-weld treatment.
>
> **RO2.1:** Research the use of machine vision to evaluate the quantitative metrics for automated quality control of post-weld treatment.

Referring to the research classification, Section 5.1, Paper A [1] focuses primarily on quality assurance and touches upon quality control by replacing the human operator.

The work is a continuation of the study presented in [6], where the effects of HFMI treatment are investigated on large-scale samples for the offshore industry. The study performed in [6] demonstrated that HFMI treatment significantly improves fatigue performance on large-scale samples. Moreover, the industrialisation of post-weld treatment was discussed, wherein automation of post-weld treatment is presented as a potential and effective solution, leading to Paper A [1].

The below section is based on Paper A [1], so phrasing, context, results, figures, and table may be repeated.

5.2.1 Introduction

It is widely accepted that the fatigue life of welds in metal structures is often lower than the base material, resulting from localised stress concentrations found along the weld toe [24]. To address this issue, several post-weld techniques have been developed to improve the fatigue life of welds, including high-frequency mechanical impact (HFMI) treatment. HFMI treatment has been demonstrated to outperform existing methods [25], but the manual application is characterised by an unpleasant work environment and suffers from uncertainties in the workmanship and quality [30]. Instead, [55] and [54] presented automated approaches based on generic linear trajectories, which resulted in poor treatment quality. Therefore, this study investigates the application of 3D scanning to propose an automated system designed to perform adaptive post-weld treatment and quality inspection of linear welds. The aim is to improve the overall quality assurance of the post-weld treatment and the robustness of the succeeding quality inspection.

5.2.2 Methodology

The proposed system relies on a combination of software and hardware operations and can be divided into two primary operations: automatically treating the weld toe and performing the quality inspection of the treatment.

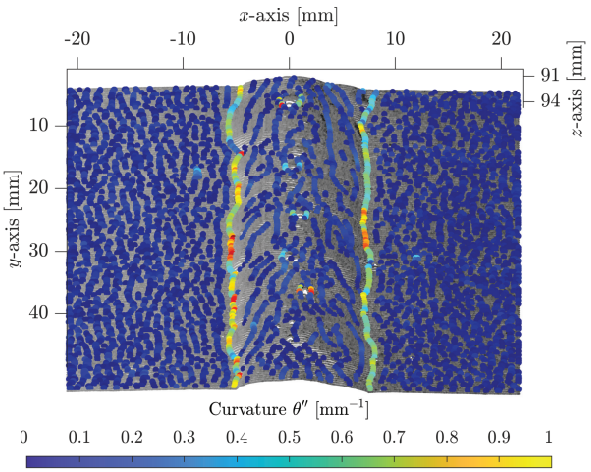

Fig. 5.2: The local curvature peaks displayed across the entire point cloud. The random scattering of points represents scan noise and surface anomalies, while the clear, semi-clustered lines of connected points highlight the weld toes and other distinct areas. Reprinted from [1], licensed under CC BY 4.0.

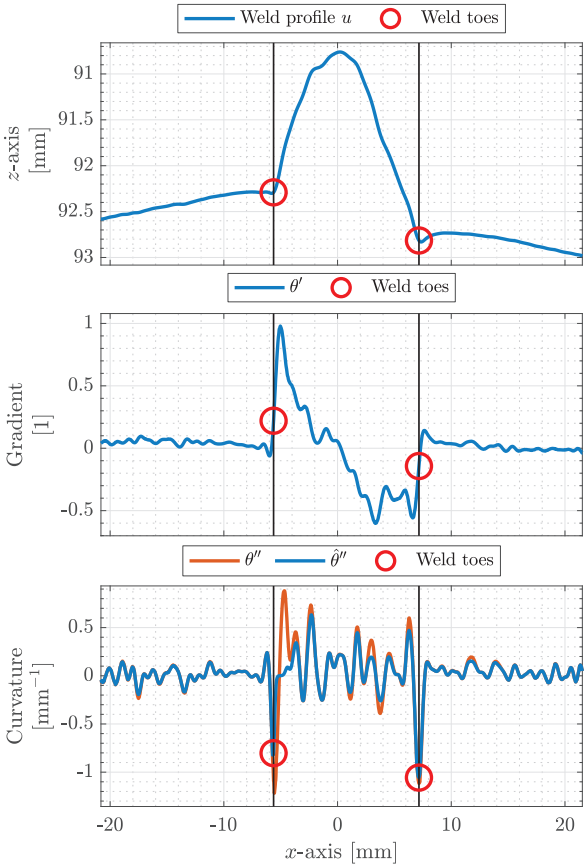

Fig. 5.3: The upper plot presents the weld profile with red circles depicting the located weld toe. The middle plot presents the gradient across the weld profile, while the button plot presents the curvature (red line) and the penalised curvature (blue line). Note that using either the gradient or curvature separately would result in an incorrect estimation of the weld toe location. Reprinted from [1], licensed under CC BY 4.0.

The line scanner constitutes the main component, which is utilised to acquire point clouds of the weld (pre- and post-treatment) along a linear, manually programmed trajectory such that each scan line forms a 2D profile of the weld. The acquired data is then pre-processed using a 2D median filter and a low-pass Butterworth filter to smooth the data and remove noise and outliers.

The weld toes are identified by extracting the weld toe features using finite difference approximations, i.e. determining gradients and curvatures along each weld profile. This is depicted in Fig. 5.2. Distinguishing the weld toes from other curvature peaks is addressed by penalising the computed curvatures based on their associated gradients, as shown in Fig. 5.3. As the weld toes form continuous lines along the weld, an assumption of continuity is applied to filter

out falsely located weld toe points. As a final filtering operation, excess lines are removed, leaving only the two lines furthest from the centre of the weld as the weld toes. Lastly, the estimated positions are refined using smoothing splines, resulting in a set of coordinates for each weld toe across all weld profiles.

After determining the locations of the weld toes, the travelling and working angles are computed using the curvature and profile of the weld. To ensure suitability for robotic application, the computed angles are smoothed out. As the last step, the determined weld toe locations and treatment angles are transformed into the robot's global coordinate system to generate a set of process instructions to be performed by the robot.

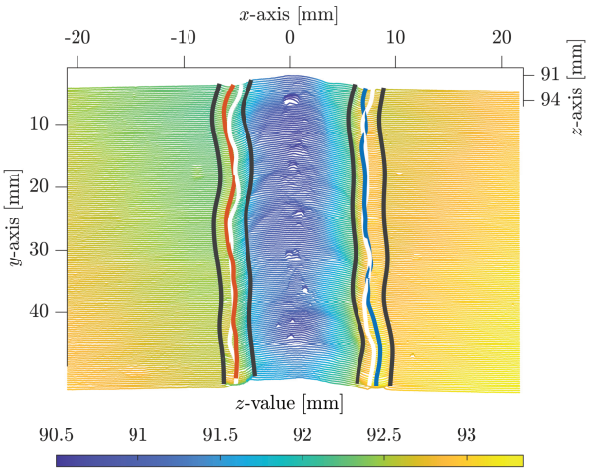

Fig. 5.4: The located treatment grooves (black lines) along with the estimated treatment trajectories (red and blue lines) and the located weld toe (white lines) before treatment. Reprinted from [1], licensed under CC BY 4.0.

The quantitative measures, as given in Section 2.1, are evaluated for the treated weld by identifying each treatment groove in the associated point cloud using principles similar to those employed for the weld toe, described in the above section. As previously, the method is primarily based on the gradients and curvature of each weld profile. The located treated groove is depicted in Fig. 5.4. The groove width and indentation depth are calculated using basic arithmetic, while an algebraic fit is used to calculate the weld toe radius. The groove deviation is determined by assuming that the groove's deepest part is where the tooltip made contact. This assumption aids in estimating the treatment path, which is then compared to the weld toe location in the scan of the untreated weld. These measures are evaluated automatically, facilitating the automatic generation of a treatment documentation report.

5.2.3 Results

An experimental setup has been designed and built to validate the proposed system, consisting primarily of a line scanner and the HFMI tool; both mounted onto an industrial robotic manipulator. Establishing the setup involved interfacing the 3D scanner, commissioning the robot, designing fixtures, and simulating the robotic motions to ensure adequate placement for reachability.

The experimental validation was performed by comparing the proposed system's adaptive robotic treatment to a strict linear robotic treatment and a conventional manual treatment, each treating 600 mm of weld toe. A noticeable reduction in robot programming time was observed from over 10 min (manual, linear trajectory) per treated sample to around 2 min, showing a reduction of more than 80%. A further decrease in the programming time is expected if the method is applied to curved welds, as manually programming curved trajectories is tedious and time-consuming.

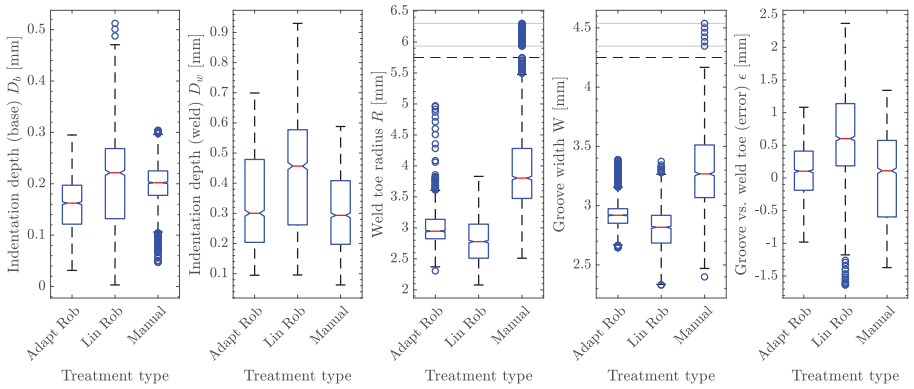

Fig. 5.5: Box plot illustrating the variance and median of the evaluated quantitative quality metrics, as defined Section 2.1, Fig. 2.1. Reprinted from [1], licensed under CC BY 4.0.

Statistical analysis of the results demonstrated that the developed system reduced the overall treatment variance by 31.9% and 26.6% compared to the linear robotic and manual treatment, respectively. The treatment variance is represented as the mean-variance across all evaluated quantitative metrics, depicted in Fig. 5.5. The error in the groove's position versus the weld toe, denoted as ϵ, was found to be 0.09 mm, 0.65 mm, and 0.02 mm for the adaptive robotic, linear robotic, and manual treatment, respectively. As such, the adaptive robotic treatment resulted in a substantial mean error reduction of 86.2% (0.56 mm) and a standard deviation reduction of 45.8% (0.33 mm) compared to the linear robotic treatment. While the mean error in the adaptive robotic treatment was slightly greater than that of the manual treatment, the standard deviation was 64.1% (0.25 mm) lower, indicating improved process stability.

5.2.4 Conclusion

This work addresses **RO1.1** by applying a 3D scanner to obtain a dense representation surface of the weld, followed by finite difference approximations to extract the weld toe features. This allows for identifying and extracting the weld toe's location and position such that the post-weld treatment can be specifically adapted to each weld. **RO2.1** is similarly addressed by identifying and locating the treatment groove, i.e. by applying machine vision and finite differences approximations. However, the quantitative metrics are evaluated using basic arithmetic on the extracted features from the treatment groove.

Addressing the research objectives has led to the development of an integrated and automated system for adaptive post-weld treatment and quality inspection based on 3D scanning. Designed primarily for linear welds, the system demonstrates a substantial potential to enhance both the post-weld treatment and quality inspection, particularly excelling in process stability and providing extensive technical documentation of the treatment. Furthermore, by automating the treatment and the quality inspection, the working conditions for the operator are vastly improved while eliminating any potential bias from the operator related to the treatment process and inspection.

5.2.5 Implications

From an academic perspective, the study explores a research gap related to automated post-weld treatment and quality inspection, advancing existing solutions limited to manual operation or fixed linear robotic treatments. In addition, it has been shown that machine vision is a powerful tool, opening the door for further studies.

It is worth noting that the study has supported further research. The authors of [104] cited and applied elements of the proposed method to experimentally validate the effects of adaptive, automated HFMI treatment on the fatigue performance of treated samples. The results showed that the manual and robotic treated samples had comparable fatigue performance, while the reproducibility was improved for the robotic treated samples.

From the viewpoint of the welding industry, the improved process stability, quality assurance, and extensive technical documentation of the HFMI treatment could allow classification agencies to accept the treatment for use at the design stage for offshore steel structures. This could result in considerable materials savings for the offshore industry due to more durable welds, improving the sustainability and economic feasibility of welded structures.

However, the presented work has some limitations. The developed system focuses on linear welds, limiting its actual applications in the industry. Moreover, the resulting fatigue performance from the adaptive robotic treatment has not been experimentally validated, which is crucial for commercial application.

Other approaches to identify and locate the weld toe, e.g., using machine learning, could be investigated further.

5.2.6 Additional Work

In this section, additional and relevant work conducted after the publication of the presented paper, Paper A [1], is briefly introduced. Additionally, Paper E [5] continues the work in Paper A [1] and proposes a method for digitally reconstructing untreated and treated welded components for fatigue life prediction using finite element modelling.

Geometrical Inspection of Welds

It has been investigated if the proposed method using the gradient and curvature of the weld profile could be applied for geometrical inspection of the weld itself. The geometrical inspection aimed to evaluate the weld quality to avoid treating defective welds, i.e., the amount of undercut, homogeneity, and bead height and width. The study showed promising results, but further work is required to improve and validate the investigated method.

Fig. 5.6: The large-scale sample on which the automated post-weld treatment of curved welds is based. The sample exemplifies part of a jacket structure for the offshore industry.

Automated Post-Weld Treatment of Curved Welds

The ability to only treat linear welds is a clear limitation of the presented method. As such, a study was conducted to investigate if the proposed method of Section 5.2.2 could be applied to perform automated post-weld treatment of curved welds. The study was based on large-scale samples of jacket structures for the offshore industry, as shown in Fig. 5.6.

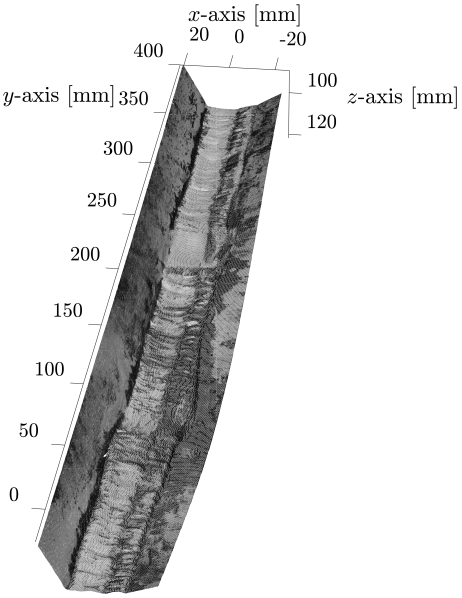

Fig. 5.7: Point cloud of the curved weld in the local coordinate system of the 3D scanner.

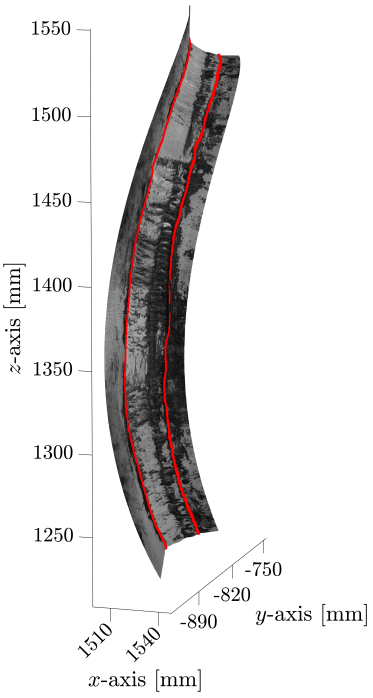

Fig. 5.8: Point cloud of the curved weld in the global coordinate system of the robot. The two red lines indicate the located weld toes, constituting the robotic trajectory for the treatment.

Due to the increased geometrical complexity of curved welds, the robotic scanning trajectory is planned using robot simulation software and the CAD file of the part. Maintaining a constant velocity, distance, and orientation relative to the weld surface is essential to ensure sufficient scan quality. As all point clouds are acquired in the local coordinate system of the 3D scanner, the actual robot trajectory is logged during the scanning motion. This permits transforming the point cloud to the global coordinate system of the robot, which is later necessary when generating process instructions for the robot. However, by initially representing the acquired point cloud in the local coordinate system of

the scanner, depicted in Fig. 5.7, it is possible to apply the same methodology as presented in Section 5.2.2.

As such, the acquired point cloud is filtered, and the gradient and curvature of the weld profile are extracted to locate the weld toes. The locations of the weld toes are then transformed into the global coordinate system of the robot to form the treatment trajectories, depicted in Fig. 5.8.

The proposed method for post-weld treatment of curved welds was tested empirically. Here, it was observed that the generated robotic trajectory allows the HFMI tool to accurately follow the weld toes as intended. However, any actual HFMI treatment was not performed due to time constraints. Hence, future work involves testing the proposed methodology for curved welds by performing post-weld treatment and the subsequent quality inspection.

5.3 Paper B: Flexible and In Situ Calibration of Galvanometric Scanner Systems

The second paper in this thesis, Paper B [2], is titled "Three-Dimensional Scanning Applied for Flexible and In Situ Calibration of Galvanometric Scanner Systems". The paper has been submitted and published in *Sensors*, MDPI, 2023. The paper relates to research question **RQ1** by addressing research objective **RO1.2**:

> **RO1.2:** Develop a flexible and generalised methodology for automated calibration of galvanometric laser scanner (GLS) systems using machine vision.

Referring to the research classification, Section 5.1, Paper B [2] also focuses on quality assurance but takes another approach, as the proposed method extends the capabilities of the human operator.

The work provides a prerequisite for the computer-aided process planning system for laser forming presented in Paper F [6]. The proposed calibration methodology supports the laser processing operations by calibrating the applied GLS system, thus, demonstrating the proposed method in use.

The below section is based on Paper B [2], so phrasing, context, results, figures, and table may be repeated.

5.3.1 Introduction

Galvanometric Laser Scanning (GLS) systems are commonly applied in laser processing for their precision and repeatability. However, calibration is required due to unknown mechanical and thermal defects, which is further complicated in robotic applications due to variable relative positioning. Traditional calibration methods involve creating look-up tables (LUT) or constructing physical

models, but these are computationally costly, data-sensitive, or require in-depth knowledge of the optical design [62, 69, 37]. While artificial neural networks (ANN) have been shown to outperform existing methods, their application in calibrating GLS systems for laser processing is limited and unsuitable for robotic applications where the positional relationship is not fixed [69].

As such, the proposed method aims to introduce a generalised and flexible in situ calibration method for GLS systems based on 3D scanning, which emphasises robotic applications. The intended purpose of the methodology is to minimise positional errors by compensating for scan field distortion through a neural network. By employing 3D scanning to evaluate and correct the relative pose between the GLS system and the calibration plane, the need for a fixed positional relationship is eliminated, making the proposed calibration method suitable for robotic applications.

5.3.2 Method

Initially, a simple sheet metal plate is manually placed within the workspace of the system, which serves as a calibration plate to eliminate the need for specialised calibration equipment. Subsequently, a 3D scan is performed, providing a point cloud of the calibration plate. The surface normal and position of the plate are estimated by fitting a plane to its surface, hence, reducing calibration errors and removing the need for precise positioning of the plate. In order to determine the scan field deviation, a set of fiducials is marked onto the plate using a simplified geometrical model, which relates the scanner control input to the Cartesian points in the workspace using a few parameters. Again, a 3D scan is performed to determine the calibration plate's surface normal, as presented in Fig. 5.9. This information is used to project the point cloud to 2D, permitting the use of prevalent image processing techniques to determine the fiducials' actual positions, i.e. image morphology, Canny Edge Detection, and the Circle Hough Transform, depicted in Fig. 5.10.

By comparing the actual positions to the nominal target positions, it is possible to identify any scan field distortion, represented as positional deviations. A Radial Basis Function (RBF) feed-forward network of three layers is trained using the detected positional deviations, making it able to predict the necessary corrections across the scan field. The result is a simple, fast, and generalised solution. The RBF network is chosen due to its low computational load and training times, reliability, and reduced extrapolation errors. The network is trained using the Orthogonal Least Square (OLS) method due to its simplicity, speed, and deterministic behaviour. The characteristics of both the network and training method are necessary to achieve a robust solution that can be integrated into the control system of the scanner, supporting a fully automatic solution.

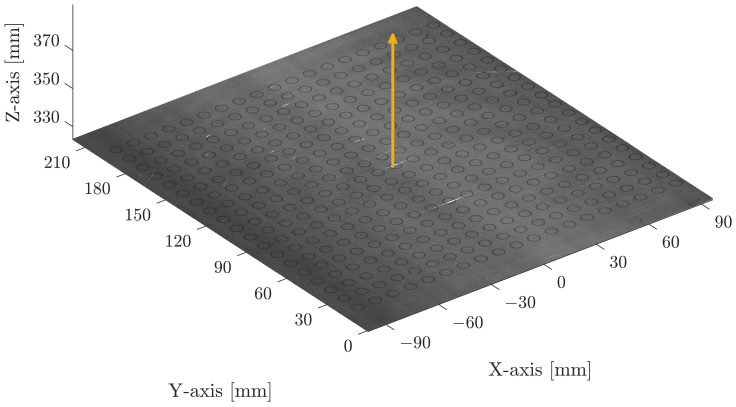

Fig. 5.9: The obtained point cloud of laser-marked fiducials. The determined surface normal used for 2D projection is indicated by the yellow arrow. Reprinted from [2], licensed under CC BY 4.0.

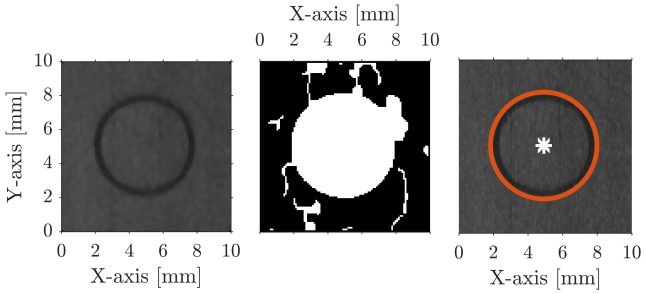

Fig. 5.10: The image processing steps to determine the actual positions of the marked fiducials. Initially, a median filter is employed to eliminate noise (left), followed by the Canny Edge Detection and morphology operations to isolate and enhance edges in the image (centre). Lastly, the Circle Hough Transform is applied to identify circles and extract their centre coordinates (right). Reprinted from [2], licensed under CC BY 4.0.

5.3.3 Results

The proposed method is tested and validated on a setup with the main components consisting of a 6-axis industrial manipulator, a commercial GLS system, a laser line scanner, and a fibre laser.

To ensure the validity of the measurement method, the measurement accuracy and uncertainty were assessed using a certified ceramic calibration plate. The standard uncertainty was found to be 0.0862 mm (k = 1), while acceptable repeatability and insignificant bias were observed; hence, suggesting that the measurement method was sufficient given the considerable measurement distance.

Training of the Radial Basis Function (RBF) network yielded an average prediction error of 0.047 mm with an average training time of 5.88 s.

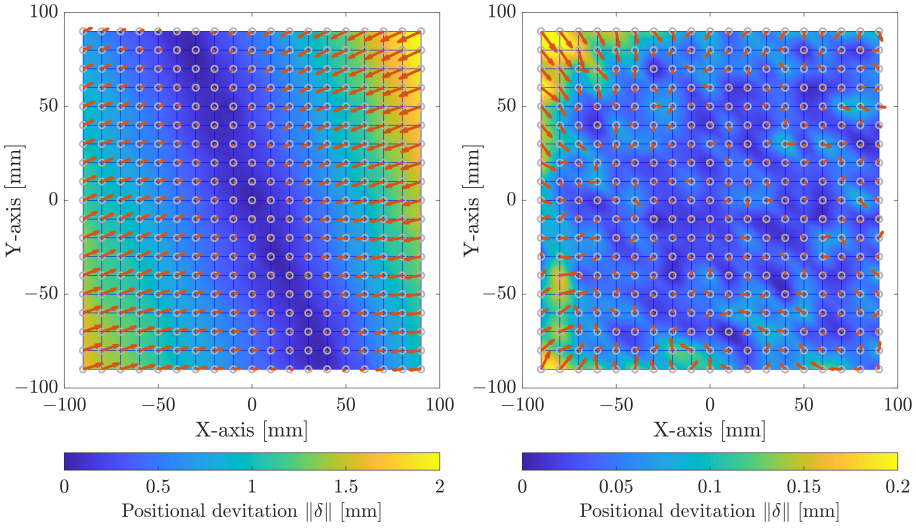

(a) Positional deviations prior to calibration.

(b) Positional deviations post-calibration.

Fig. 5.11: The results of the GLS system calibration. The grey circles indicate the target positions, while the red arrows indicate the direction and scale of the positional deviation. Note that the scaling of the colour bar is ten times larger in (**a**) compared to (**b**). Reprinted from [2], licensed under CC BY 4.0.

The entire calibration, which includes data and image processing as well as network training, had an overall duration of 62 s, with the RBF network completing a single iteration in 0.000055 s. This makes the RBF network suitable for real-time implementation. All computations were performed on an Intel Core i7-9750H CPU @ 2.6 GHz.

As observed in Fig. 5.11a, prior to calibration, the GLS system showed significant non-uniform scan field distortion, smallest at the centre and increasing towards the edges. The most significant overall deviation was measured to 2.08 mm, while the root mean square (RMS) deviation amounted to 0.85 mm, likely attributed to thermal influences or defects in the assembly. This distortion was considered unacceptable for practical applications.

After applying the proposed calibration method, the maximum deviation was reduced to 0.25 mm by 87.8%, whereas the RMS deviation was reduced to 0.071 mm by 91.7% with 80% of the deviation being below 0.08 mm. This can be seen in Fig. 5.11b. However, outliers in the lower right and upper left corners suggested measurement errors, which could be solved using a 3D scanner with an improved spatial resolution. Moreover, reducing the scan field by 15 mm around the border halved the maximum deviation to 0.135 mm. As excessive distortion along the border of the scan field is typical for GLS systems, reducing the scan field is common practice.

5.3.4 Conclusion

RO1.2 is addressed by combining a simplified geometrical model with an RBF network to predict and correct the GLS system's positional deviations. The RBF network is trained on measured positional deviations obtained using 3D scanning. The developed methodology offers a generic and flexible in situ solution which does not rely on exhaustive prior knowledge of the system and its relative positioning. This is achieved by employing 3D scanning to estimate the relative pose between the GLS system and the calibration plane. The experimental validation of the proposed method demonstrates a high resulting processing accuracy (<0.25 mm), hence, underlining its suitability for industrial use to improve the efficiency, accuracy, and flexibility of laser processing applications.

5.3.5 Implications

From an academic point of view, the study addresses a literature gap by focusing on the calibration of GLS systems for robotic manipulation, an area previously lacking research. Moreover, the study has shown that 3D scanning can successfully be used to acquire accurate data for calibrating GLS systems, supporting potential future research.

From an industrial perspective, the decrease in calibration time and human involvement leads to improved productivity and a reduction in the rate of errors. With the proposed system, calibration and validation can be carried out in under 10 min. As only limited prior positional information is required to obtain an accurate calibration, the increased flexibility allows the system to adapt to different working conditions and processing setups.

The proposed method is trivial to implement since only minimal information about the GLS system's optical design is required. Hence, it is potentially applicable in a wide range of commercial GLS systems with only minor adjustments. Additionally, downtime of the system can be reduced since re-calibration can rapidly be performed in case of modifications to the mechanical or optical design of the GLS system, improving the overall cost-effectiveness.

However, the proposed method has some limitations and potential error sources, underlining the need for further research to improve calibration accuracy. Using a simplified geometrical model results in significant positional deviations prior to calibration. By reducing the positional deviations prior to calibration, e.g. by improving the applied geometrical model, the post-calibration accuracy would potentially also be improved. Additionally, the thermal distortions affecting the assumed flatness of the calibration plate, the absolute positional errors from the robot's movements, and the inability to measure rotational errors around the Z-axis require focus to further improve the accuracy and reliability of the calibration.

5.4 Paper C: Approximating Local Changes in Surface Absorption for Laser Marking

The third paper in this thesis, Paper C [3], is titled "A Novel Method for Approximating Local Changes in the Surface Absorption for Laser Marking Using 3D Laser Scanning" has been submitted to and presented at the NOLAMP17 conference and published in the *IOP Conference Series: Materials Science and Engineering*, IOP Publishing, 2021. The paper relates to research question **RQ2** by addressing research objective **RO2.2**:

> **RO2.2:** Explore the potential of machine vision to identify local variations in surface absorption for improved quality control of laser marking.

Referring to the research classification, Section 5.1, Paper C [3] instead focuses on replacing the human operator for quality assurance of the workpiece before processing.

The paper is derived from the two patents Patent A [9] and Patent B [10], which both present the original idea of applying backscatter intensities from a laser scanner to determine the surface reflectivity. As such, the proposed method facilitates combining laser processes, Patent A [9], and process planning of the combined processes, Patent B [10].

The below section is based on Paper C [3], so phrasing, context, results, figures, and table may be repeated.

5.4.1 Introduction

Laser marking is a technique used to alter the colour of metal components for aesthetic or communicative purposes. One approach is to use laser heating to form an oxide layer on the metal's surface, modifying the optical properties of the surface. The resulting colour is then a result of the thickness and the refractive of the oxide layer as well as the order of interference [33]. The process heavily depends on the induced heat and, thereby, surface absorption, which is influenced by several factors, including surface contamination, existing oxidation, and roughness. The sensitivity of the process makes laser marking challenging to control in an industrial setting [39]. Therefore, knowledge of surface absorption is essential to achieve a stable process. However, current methods for determining surface absorption cannot provide a local estimation and are unsuitable for use in an industrial laser marking setup [70].

Consequently, this paper aims to address this gap by exploiting the backscatter intensities from a laser scanner to approximate local changes in surface reflectivity. The feasibility and effectiveness of this approach are tested through a series of experiments and validated by comparing with spectroscopy-measured values. As such, Paper C [3] answers research objective **RO2.2** of research question **RQ2**.

5.4.2 Method

The main component is the 3D laser line scanner which uses a blue laser (λ = 407nm). The 3D scanner operates based on the principles of laser triangulation, which exploits the geometric relationship between the projected laser line and the scanner's CMOS sensor to determine the distance to the surface. As a result, the projected laser line's incident angle changes across the scanning width; hence, the measured backscatter intensity will vary across a flat surface, especially in the case of specular surfaces like metals. Therefore, the raw backscatter intensities W_b do not alone reflect the local surface reflectivity accurately.

Therefore, to minimise the geometrical effects, the proposed method utilises a bi-directional reflectance distribution function (BRDF) model to compute the expected reflectance intensities, rendering a contaminant-free surface W_r as if acquired by the 3D scanner. The Cook-Torrance BRDF model has been selected as it is suitable for rendering metallic surfaces, can represent both diffuse and specular reflections, and provides a realistic estimation by considering physical laws, like energy conservation and the Helmholtz Reciprocity.

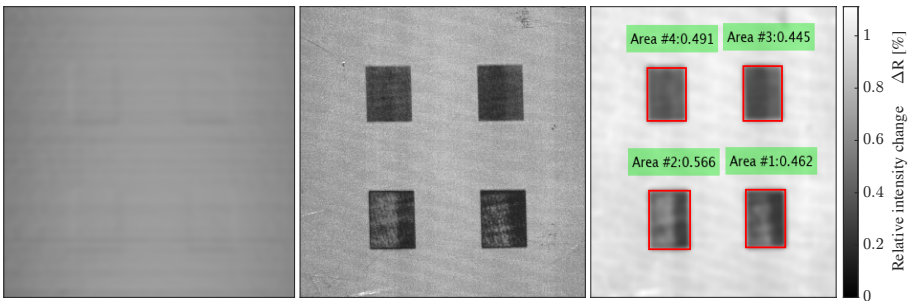

Fig. 5.12: Left: Rendered surface W_r using the Cook-Torrance BRDF model. Centre: Raw backscatter W_b intensities acquired by the 3D scanner. Note that the darker areas have been laser processed to change the reflectivity. Right: A visual representation of the estimated relative intensity change ΔR between the backscatter intensities and the rendered surface. Reprinted from [3], licensed under CC BY 3.0.

The applied model factors in various components such as the intensity, wavelength, angle of incidence, ambient light, and surface roughness. The wavelength of the scanner is known along with the angle of incidence, which is determined by computing the normals across the sample from the 3D scan. The main challenge lies in accurately determining the remaining and unknown parameters. This is overcome through a non-linear least square problem that estimates the unknown parameters by minimising the difference between the modelled reflectance intensities and the actual backscatter intensities from the 3D scan.

Hence, by utilising the estimated parameters in the BRDF model, the surface of the samples can be rendered. The rendered surface is then compared to the acquired backscatter intensities to determine the relative change in reflectivity ΔR. The principle is depicted in Fig. 5.12. Under the assumption that light is not transmitted through the material, the reflectivity represents the absorption.

5.4.3 Results

The method has been tested using a setup consisting of a laser line scanner, a single-mode fibre laser, and corresponding optics manipulated by a six-axis industrial robot. Subsequently, the results were validated using an integrated sphere spectrophotometer. The method was tested on six samples of standard industrial AISI 304L steel, with two being impregnated with WD40 oil, two ground with P80 grit sandpaper, and two left untreated. Each sample contained four regions that had been laser marked with varying parameters to alter the surface absorption. Based on the proposed method, the relative change in reflectivity ΔR, given by eq. 5.1, was approximated across all samples and compared to measurements performed by spectroscopy.

$$\Delta R = \frac{W_r}{W_b} \cdot 100 \tag{5.1}$$

As shown by figures 5.12 and 5.13, the results indicated that the proposed method could locally detect variations in reflectivity, showing a significant drop in ΔR in the processed areas. As the untreated sample best represents reality, its results are emphasised. Significant deviations were determined in ΔR for the untreated samples between the 3D scanner and spectroscopy measurements, from the lowest deviation at 1.6 p.p. (5.0%) to the highest at 18.5 p.p. (72.3%). Comparable deviations were observed for the samples impregnated with WD-40 and the ground samples.

When instead approximating the changes in reflectivity at the laser's wavelength (λ = 1076nm), different from the scanner's at λ = 407nm, the deviations were more significant. This was expected, as the reflectivity is known to be influenced by the wavelength. Hence, the laser used to measure the reflectivity should have a wavelength close to the processing laser to reduce approximation error.

The primary source of error may be a discrepancy in the areas evaluated by the spectrophotometer and the 3D scanner. The spectrophotometer measured the reflectivity in a loosely defined 3×3 mm^2 area, while the results from the 3D scanner were evaluated as average over the entire processed area of 20×25 mm^2. In addition, using standard AISI 304L samples to simulate an industrial setting resulted in surfaces that were not perfectly homogeneous. Consequently, the absorption varied locally within each processed area.

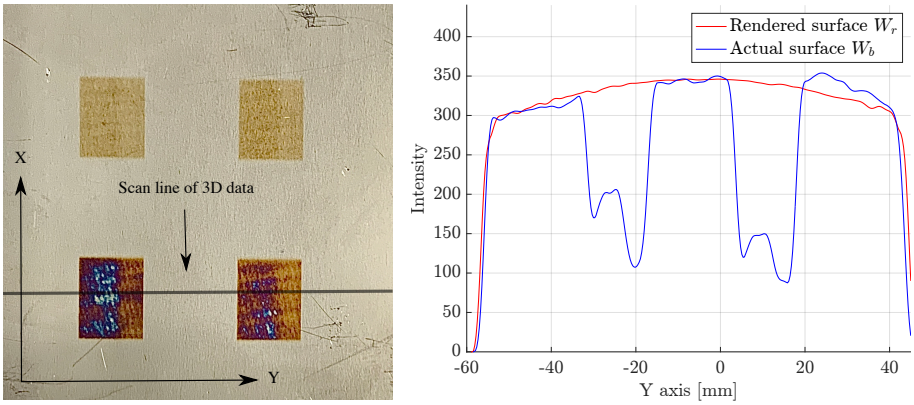

Fig. 5.13: Left: A sample after laser marking with the black line indicating the area of the sample used to generate the rendered profile on the right. Right: Profile rendered using the BRDF model and measured backscatter intensities. The intensity plot from the rendered surface W_r corresponds to the intensity plot from the actual surface W_b. Note that the scanner's sensor is placed at $y = 0$, while the laser line is projected and reflected with an increasing angle when moving away from the centre. Hence, the curvature of the line results from the reflectivity decreasing with an increasing angle of incidence. Reprinted from [3], licensed under CC BY 3.0.

Therefore, it is plausible that the spectrophotometer may have measured the reflectivity in an area with deviating absorption.

The proposed method was also evaluated using materials such as titanium, aluminium, and construction steel. These experiments showed promising results, although spectroscopy did not validate the findings. In addition, it was determined that the impact of ambient light on the results is negligible through experimental validation. This is likely due to the laser light being significantly more powerful than the ambient light.

5.4.4 Conclusion

This work addresses **RO2.2** by exploring the use of backscatter intensities from a 3D scanner to directly approximate local variations in the surface absorption for quality control in laser marking. The local variations are approximated by applying a BRDF model to render a perfectly clean reference surface and comparing it to the actual surface, represented by the measured backscatter intensities from the 3D scanner. Any deviations represent local changes in reflectivity.

However, a noticeable deviation was observed between the approximated reflectivity from the 3D scanner and the measured values from spectroscopy. Consequently, the investigated method is not industrially applicable in its current state; thus, the study acts as a proof of concept. As the existing solutions are either limited to global measurements or unsuitable for use

in an industrial laser marking setup, the proposed method overcomes their limitations. However, further research is required to improve the approximation accuracy.

5.4.5 Implications

From an academic standpoint, this study investigates the feasibility of using backscatter intensities to determine surface absorption for laser processing. As no existing method is able to determine the local surface absorption directly as a part of the laser processing setup, the proposed method fills out a gap in the literature. Furthermore, the novel approach supports future research in utilising the backscatter intensities to solve one of the main challenges in laser marking, i.e. varying surface absorption.

On an industrial level, accurate knowledge of local changes in surface absorption can significantly benefit the laser marking processes. Knowledge of local changes across the surface of the workpiece allows the industry to enhance the stability and quality of their laser marking processes, as the process parameters can be determined accordingly. Furthermore, the proposed method could potentially limit the requirements for the surface condition of the workpieces and identify insufficient workpieces prior to processing, reducing waste and improving the efficiency and feasibility of laser marking.

However, in its current state, the proposed method acts as a proof of concept and requires additional development, testing and validation before being widely implemented in the industry. As such, future developments could focus on the proposed method's ineffectiveness on highly reflective surfaces and samples tilted at excessive angles, along with improvements in the method's overall accuracy. Note that the limitation in the tilting angle results from the laser scanner's inability to measure the backscatter if the light is reflected away from the scanner. For untreated rolled stainless sheet metal and when using the specific laser scanner, the tilting angle is limited to 30°.

5.5 Paper D: Quality Inspection of Double-Curved Robotic Laser Welds

The fourth paper in this thesis, Paper D [4], is titled "Quality Inspection System for Robotic Laser Welding of Double-Curved Geometries". The paper has been submitted and presented at the NOLAMP17 conference and published in *Procedia Manufacturing*, Elsevier, 2019. The paper relates to research question **RQ2** by addressing research objective **RO2.3**:

> **RO2.3:** Study the application of machine vision for quality inspection in laser welding of double-curved geometries to enhance quality control.

Paper D [4] falls into the last category of the research classification, Section 5.1, focusing on quality control by extending the capabilities of the human operator.

The below section is based on Paper D [4], so phrasing, context, results, figures, and table may be repeated.

5.5.1 Introduction

High-power laser welding is widely used in industrial mass production, as it offers a highly flexible and accurate approach capable of producing high-speed welds. Nevertheless, due to the laser beam's small spot size, maintaining weld integrity necessitates precise tolerances in the joint alignment and the positioning of the laser beam's focal point [41]. The problem is further pronounced in robotic laser welding due to positional inaccuracies, primarily along complex double-curved trajectories. Various monitoring and control systems relying on machine vision have been developed to monitor the laser welding process [82, 40]. However, no method has been developed to determine the trajectory deviation of double-curved welds. Therefore, this paper introduces a quality inspection system that applies machine vision for quality inspection for laser welding of double-curved geometries. The aim is to obtain reliable process knowledge to determine errors in laser beam positioning and alignment to ensure consistent and satisfactory weld quality. Hence, Paper B answers research objective **RO2.3** of research question **RQ2**.

5.5.2 Methodology

The methodology takes offset in an automated laser welding cell, in which the laser optics have been mounted on a six-axis industrial manipulator to enable the welding of double-curved geometries. The proposed quality inspection system relies primarily on a CMOS camera, mounted to view through the laser optics, accompanied by external LED illumination and corresponding optical filters. Throughout the procedure, the camera captures an area around the moving laser beam's focal point, which acts as input for the system.

The proposed system performs two main objectives to determine errors in beam positioning:

1. **Locating the joint:** Initially, a visible region in all video frames is selected. Secondly, the region is extracted such that it only represents the joint. This is followed by using the Canny edge detector and a standard Hough transform to extract the outline and centre position of the joint. The process is illustrated in Fig. 5.14.

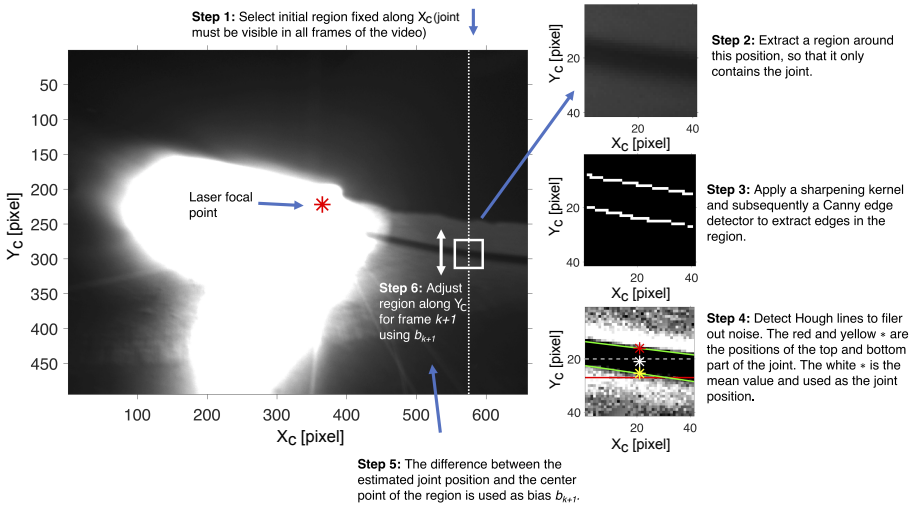

Fig. 5.14: Video frame captured during laser welding, detailing the five steps for locating the joint. Reprinted from [4], licensed under CC BY-NC-ND 4.0.

2. **Estimating the weld trajectory:** Using normalised cross-correlated template matching, the displacement field is computed between two consecutive video frames, representing the welding trajectory. The template matching is done based on the extracted region of the previous task. However, as this process is prone to significant noise from light disturbances, a Kalman filter in conjunction with a Radial Basis Function (RBF) neural network is used to refine the estimated trajectory. The purpose of the RBF network is to predict the displacement field in scenarios where it cannot be directly estimated, improving the accuracy of the proposed method.

5.5.3 Results

The effectiveness of the quality inspection system is empirically validated on 24 welds, performed in an automated robotic laser welding setup along double-curved trajectories. To verify the proposed system's ability to detect positional shifts in the process, the welding trajectory is purposely offset 1 mm along a single Cartesian axis in six of the 24 welds.

Using the proposed system makes it possible to visualise the welding trajectory relative to the joint location. This is done by extracting a fixed region from each video frame and combining them into a single image based on the estimated displacement field. The combined image is illustrated in Fig. 5.15, which also visualises the located joint and the computed welding trajectory.

The errors in laser beam positioning are evaluated by measuring the radial distance between the determined trajectory and the joint location.

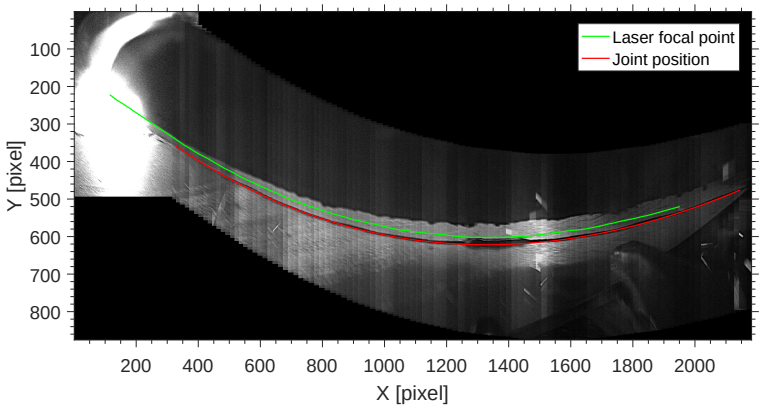

Fig. 5.15: A visualisation of the located joint and computed welding trajectory. The image is created by extracting a fixed region from each video frame and aligning them using the estimated displacement field. The green line marks the welding trajectory, while the red line represents the joint position. Reprinted from [4], licensed under CC BY-NC-ND 4.0.

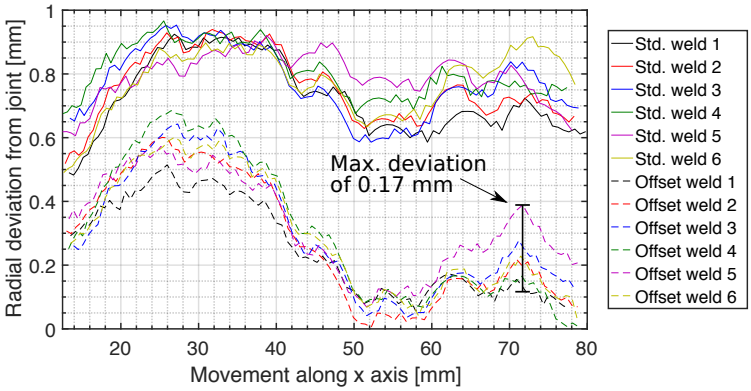

Fig. 5.16: Radial deviation of welding trajectories relative to the located joint. Note the clear positional shift between the standard and offset welds. Reprinted from [4], licensed under CC BY-NC-ND 4.0.

The results are depicted in Fig. 5.16, where a clear positional shift is observed between the standard and nominal samples, hence, validating the system's ability to detect positional shifts. Assuming that the robot is positionally accurate and the samples are perfectly aligned, which is unlikely to be the case, the observed maximum error in the system's estimation of the weld toe deviation is 0.17 mm. As a result, Fig. 5.16 provides an indication of the proposed system's accuracy.

Alternatively, the accuracy of the proposed system is determined by transforming the estimated errors in the laser beam positioning to the global coordinate system of the manipulating robot. Here, a trajectory deviation of 0.95 mm is observed on the offset samples. This is a 0.05 mm error from the expected value, underlining the system's accuracy. This slight error is likely due to positional inaccuracies in the robot or excessive image noise.

5.5.4 Conclusion

RO2.3 is addressed by developing a machine vision system that uses a co-axially mounted camera combined with prevalent image processing methods and a Kalman filter aided by a neural network. The proposed quality inspection system for robotic laser welding is designed for double-curved geometries. It aims to visualise the welding trajectory and detect errors in the laser beam positioning relative to the joint position. Experimental validation demonstrated promising results, showing that the system could detect a positional shift in the welding trajectory relative to the joint position. As a result, the proposed method enhances the overall quality control of laser welding, supporting its industrial applicability.

5.5.5 Implications

From an academic standpoint, the presented work significantly contributes to enhancing the quality control of laser welding. The proposed quality inspection system addresses a gap in the existing literature by emphasising laser welding of double-curved geometries, whereas previous methods to determine trajectory deviation focus mainly on linear or single-curved welds.

From an industrial perspective, implementing the developed system can offer substantial benefits, particularly in automated production setups where a six-axis robot manipulates the laser welding optics along complex 3D welding trajectories. The system's ability to detect changes in the welding trajectory relative to the joint position is essential in identifying defective welds and understanding the causes of process shifts. Moreover, by accurately identifying points of failure along the welding trajectory, adjustments can be made to improve the welding process's overall quality and reliability. This strengthened understanding of the process can also support the design stage of future components to avoid potential failures.

However, it is essential to note that the proposed machine vision system has its limitations. It is currently unable to identify undesirable changes in the robotic pose or distance relative to the part. Therefore, further research is needed to improve the monitoring accuracy of the system, possibly by utilising 3D scanning.

Chapter 6

Concluding Remarks

This chapter concludes the PhD thesis by summarising the research contributions from the associated papers, Part III, and the extended abstract from Chapter 5. In addition, the overall research implications are discussed, and the general direction of future work is presented.

In recent years, technological advancements and improved affordability of imaging components have expanded the use of machine vision systems to more advanced and complex applications. Therefore, this PhD study aimed to advance quality assurance and quality control of industrial manufacturing by exploiting the technological advances in machine vision. The Design Science Research (DSR) methodology guided the research to follow the six steps proposed by [43], combining theory and practice to develop generic solutions with real-world industrial applicability.

To limit the scope of the study and to emphasise the real-world applicability of the developed solutions, the work was centred around two industrial cases, CeJacket and INTERLASE. The industrial cases focused on automation and quality inspection of post-weld treatment and calibration and monitoring of laser processes. Based on the defined problems and conducted literature study, the PhD thesis identified several research gaps leading to the formulation of two research questions, **RQ1** and **RQ2**:

> **RQ1**: How can machine vision be applied to advance the quality assurance of manufacturing processes in the context of the industrial cases?
>
> **RQ2**: How can machine vision be applied to advance the quality control of manufacturing processes in the context of the industrial cases?

6.1 Summary of Research Contributions

RQ1 and **RQ2** were answered by addressing the associated research objectives through research in applied machine vision, resulting in significant contributions to quality assurance and quality control of industrial manufacturing.

6.1.1 Addressing RQ1: Quality Assurance

RO1.1 Investigate the application of machine vision to extract the location and geometry of the weld toe for automated and adaptive post-weld treatment.

In Paper A [1], machine vision was investigated to extract the weld toe location and geometry based on finite differences. The investigation led to developing an integrated and automated system, relying on 3D scanning to perform post-weld treatment of linear welds. The proposed system adapted the treatment to each weld, demonstrating a significant potential to eliminate operator bias, enhance process stability, and improve the overall quality assurance of HFMI treatment. Although, the system's limitation to linear welds and lack of validated fatigue performance of the treated samples provides opportunities for further research.

RO1.2 Develop a flexible and generalised methodology for automated calibration of galvanometric laser scanner (GLS) systems using machine vision.

In Paper B [2], machine vision is applied to develop a methodology for automated calibration of GLS systems. The developed methodology offers a flexible and generic calibration approach by employing 3D scanning, a simplified geometrical model, and an RBF network, relying on limited prior knowledge of the GLS system and its relative positioning. The proposed solution provides a high calibration accuracy with a trivial implementation suitable for various industrial applications. However, further research is required to optimise the resulting calibration accuracy.

6.1.2 Addressing RQ2: Quality Control

RO2.1 Research the use of machine vision to evaluate the quantitative metrics for automated quality control of post-weld treatment.

In Paper A [1], 3D scanning was applied to automatically evaluate the quantitative metrics of post-weld treatment based on finite differences. The proposed method contributed to the automated system for

post-weld treatment **(RO1.1)**, enhancing its capabilities to perform automated quality inspection. The method proved accurate and efficient in evaluating the quantitative metrics to automatically generate extensive technical documentation of the treatment for enhanced quality control. Nevertheless, as is the case for the automated treatment, the proposed method is currently limited to treatment of linear welds.

RO2.2 Explore the potential of machine vision to identify local variations in surface absorption for improved quality control of laser marking In Paper C [3], backscatter intensities from a 3D scanner combined with a reflectance model were used to directly approximate the local surface absorption as a part of an industrial laser marking setup. Though promising, the proposed approach currently serves as a proof of concept to enhance the process stability and quality control of laser marking. However, further research is required to improve the approximation accuracy and realise the full potential of the proposed approach.

RO2.3 Study the application of machine vision for quality inspection in laser welding of double-curved geometries to enhance quality control In Paper D [4], the combination of a 2D camera and a Kalman filter aided by an RBF network was explored to determine the laser welding trajectory and its relative positioning to the joint. The investigation led to the development of a quality inspection system for laser welding of double-curved geometries, which was experimentally proven to detect variations in the welding trajectory. The promising results could allow the proposed system to play an essential role in process optimisation and quality control when welding double-curved geometries. Although, the system cannot detect changes in the welding orientation or processing distance, warranting further research.

6.2 Implications

In summary, the PhD thesis has investigated and developed machine vision applications to advance quality assurance and quality control in industrial manufacturing, specifically focusing on post-weld treatment and laser processes. The study has demonstrated that machine vision is a practical approach to acquiring dense and accurate process knowledge, supporting the digital transformation and the realisation of Industry 4.0.

From an academic perspective, the PhD thesis presents a significant contribution to the field of machine vision, filling research gaps and supporting future research within automated post-weld treatment, calibration of GLS systems, and quality inspection of laser marking and laser welding. In developing the proposed solutions, the study has demonstrated that relying on prevalent

image and point cloud processing techniques can provide flexible, generic, and robust solutions that are trivial to implement. Although, careful consideration must be placed on the data acquisition and pre-processing aspects to reduce acquisition noise, especially when using 3D scanning to represent reflective and complex surfaces.

From an industrial viewpoint, the PhD thesis has demonstrated the broad applicability of machine vision systems to either replace the human operator or extend human capabilities, leading to enhanced working conditions for operators and improved productivity, process stability, and product quality. In conclusion, the collaboration between academia and industry aids in ensuring the real-world applicability of the developed solutions. In addition, the collaboration provides the industry with insight into state-of-the-art developments within industrial manufacturing, thereby paving the way for future developments.

6.3 Future Work

In addition to the future work presented in the extended abstracts, Chapter 5, one general direction for future work is industrial implementation. Although the presented solutions have been developed with robustness and reliability in mind, they are yet to be tested and validated in the real world. Therefore, the proposed solutions should be tested in harsh industrial environments during extended periods, where the equipment is subjected to contamination, varying temperatures and lighting, and other external influences. Moreover, the usability of operators without extensive training in operating the developed systems should be tested further. Lastly, also related to industrial implementation, the computational efficiency could be optimised, especially in cases where real-time implementation may be relevant, e.g. quality inspection of laser welding.

The applicability of artificial intelligence (AI) to address the presented research questions should also be further investigated. As stated in Section 4.2.4, the use of AI in its current state has purposely been avoided, primarily due to data availability and transparency concerns. However, AI is rapidly progressing, and its use has significant potential, which could result in approaches that could overcome the drawbacks of the proposed solutions. As mentioned in Section 5.2.4, machine learning may be used to identify the weld toe in the point cloud to improve the stability of the proposed methodology.

As a final remark, it should be noted that this PhD study has merely touched upon a few selected processes, namely aspects of post-weld treatment and laser processing. However, the potential of machine vision from both an academic and industrial perspective is considerable. As technology continues to advance, opportunities for novel applications are constantly presented.

References

[1] A. F. Mikkelstrup, M. Kristiansen, and E. Kristiansen, "Development of an automated system for adaptive post-weld treatment and quality inspection of linear welds," *International Journal of Advanced Manufacturing Technology*, vol. 119, pp. 3675–3693, 2022. [Online]. Available: https://doi.org/10.1007/s00170-021-08344-0

[2] A. F. Mikkelstrup, G. N. Nikolov, and M. Kristiansen, "Three-Dimensional Scanning Applied for Flexible and In Situ Calibration of Galvanometric Scanner Systems," *Sensors*, vol. 23, no. 2142, pp. 1–19, 2023. [Online]. Available: https://doi.org/10.3390/s23042142

[3] A. F. Mikkelstrup, A. N. Thomsen, and M. Kristiansen, "A novel method for approximating local changes in the surface absorption for laser marking using 3D laser scanning," *IOP Conference Series: Materials Science and Engineering*, vol. 1135, no. 012002, pp. 1–11, 2021. [Online]. Available: http://doi.org/10.1088/1757-899x/1135/1/012002

[4] A. Mikkelstrup, M. Thomsen, K. Stampe, B. Endelt, J. Boll, E. Kristiansen, and M. Kristiansen, "Quality inspection system for robotic laser welding of double-curved geometries," *Procedia Manufacturing*, vol. 36, pp. 50–57, 2019. [Online]. Available: https://doi.org/10.1016/j.promfg.2019.08.008

[5] A. F. Mikkelstrup and M. Kristiansen, "Integrated digital reconstruction of welded components: Supporting improved fatigue life prediction," *arXiv preprint arXiv:2307.15604*, 2023, submitted to the IEEE International Conference on Imaging Systems and Techniques (IST2023). [Online]. Available: https://doi.org/10.48550/arXiv.2307.15604

[6] M. Kristiansen, R. Darula, B. Endelt, A. F. Mikkelstrup, J. Schjødt-Thomsen, J. H. Andreasen, F. Farrokhi, P. K. Hansen, P. B. W. Jensen, E. Putnam, and N. Hansen, "Improving the fatigue life of large offshore foundations," *Marine Structures*, vol. 87, no. 103314, pp. 1–13, 2023. [Online]. Available: https://doi.org/10.1016/j.marstruc.2022.103314

[7] G. N. Nikolov, A. N. Thomsen, A. F. Mikkelstrup, and M. Kristiansen, "Computer-aided process planning system for laser forming: from cad to part," *International Journal of Production Research*, pp. 1–18, 2023. [Online]. Available: https://doi.org/10.1080/00207543.2023.2241565

[8] S. E. Schrøder, U. L. Christensen, M. Hessellund, A. L. Enevoldsen, A. F. Mikkelstrup, and M. Kristiansen, "Object detection and colour evaluation of multicoloured waste textiles using machine vision," in *Proceedings of the 16th International Conference on PErvasive Technologies Related to Assistive Environments*, ser. PETRA '23. New York, NY, USA: Association for Computing Machinery, 2023, p. 543–549. [Online]. Available: https://doi.org/10.1145/3594806.3596583

[9] M. Kristiansen, E. Kristiansen, B. Endelt, S. Villumsen, A. Thomsen, and A. Mikkelstrup, "A method for processing elements into final elements," Jan. 2022, wO 2022/002338 A1; G05B 19/4097 2006.1.

[10] M. Kristiansen, E. Kristiansen, A. Thomsen, B. Endelt, A. Mikkelstrup, and G. Nikolov, "A planning method for processing an element into a final element," Jan. 2022, wO 2022/002339 A1; G05B 19/4097 2006.1.

[11] Z. Shi, Y. Xie, W. Xue, Y. Chen, L. Fu, and X. Xu, "Smart factory in Industry 4.0," *Systems Research and Behavioral Science*, vol. 37, no. 4, pp. 607–617, 2020. [Online]. Available: https://doi.org/10.1002/sres.2704

[12] S. S. Fernández-Miranda, M. Marcos, M. E. Peralta, and F. Aguayo, "The challenge of integrating Industry 4.0 in the degree of Mechanical Engineering," *Procedia Manufacturing*, vol. 13, pp. 1229–1236, 2017. [Online]. Available: https://doi.org/10.1016/j.promfg.2017.09.039

[13] K. Zhou, T. Liu, and L. Zhou, "Industry 4.0: Towards future industrial opportunities and challenges," *2015 12th International Conference on Fuzzy Systems and Knowledge Discovery, FSKD 2015*, pp. 2147–2152, 2016. [Online]. Available: https://doi.org/10.1109/FSKD.2015.7382284

[14] R. R. Rajkumar, I. Lee, L. Sha, and J. Stankovic, "Cyber-physical systems," in *Proceedings of the 47th Design Automation Conference on - DAC '10*, vol. 19, no. 3. New York, New York, USA: ACM Press, 2010, p. 731. [Online]. Available: https://doi.org/10.1145/1837274.1837461

[15] M. Javaid, A. Haleem, R. P. Singh, S. Rab, and R. Suman, "Exploring impact and features of machine vision for progressive industry 4.0 culture," *Sensors International*, vol. 3, no. August 2021, p. 100132, 2022. [Online]. Available: https://doi.org/10.1016/j.sintl.2021.100132

[16] Z. Ren, F. Fang, N. Yan, and Y. Wu, *State of the Art in Defect Detection Based on Machine Vision*. Korean Society for Precision Engineering, 2022, vol. 9, no. 2. [Online]. Available: https://doi.org/10.1007/s40684-021-00343-6

[17] Global Industry Analysts Inc., "Machine Vision Systems: Global Strategic Business Report," October 2022, ID: 338506.

[18] P. Pierleoni, A. Belli, L. Palma, and L. Sabbatini, "A versatile machine vision algorithm for real-time counting manually assembled pieces," *Journal of Imaging*, vol. 6, no. 6, 2020. [Online]. Available: https://doi.org/10.3390/jimaging6060048

[19] D. P. Penumuru, S. Muthuswamy, and P. Karumbu, "Identification and classification of materials using machine vision and machine learning in the context of industry 4.0," *Journal of Intelligent Manufacturing*, vol. 31, no. 5, pp. 1229–1241, 2020. [Online]. Available: https://doi.org/10.1007/s10845-019-01508-6

[20] L. Pérez, Í. Rodríguez, N. Rodríguez, R. Usamentiaga, and D. F. García, "Robot guidance using machine vision techniques in industrial environments: A comparative review," *Sensors (Switzerland)*, vol. 16, no. 3, 2016. [Online]. Available: https://doi.org/10.3390/s16030335

[21] S. Catalucci, A. Thompson, S. Piano, D. T. Branson, and R. Leach, "Optical metrology for digital manufacturing: a review," *International Journal of Advanced Manufacturing Technology*, vol. 120, pp. 4271–4290, 2022. [Online]. Available: https://doi.org/10.1007/s00170-022-09084-5

[22] European Factories of the Future Reserach Association, "Factories 4.0 and beyond," 2016. [Online]. Available: https://www.effra.eu/sites/default/files/factories40_beyond_v31_public.pdf

[23] A. Saihi, M. Awad, and M. Ben-Daya, "Quality 4.0: leveraging Industry 4.0 technologies to improve quality management practices – a systematic review," *International Journal of Quality and Reliability Management*, vol. 40, no. 2, pp. 628–650, 2023. [Online]. Available: https://doi.org/10.1108/IJQRM-09-2021-0305

[24] M. M. Pedersen, O. Ø. Mouritsen, M. R. Hansen, J. G. Andersen, and J. Wenderby, "Comparison of post-weld treatment of high-strength steel welded joints in medium cycle fatigue," *Welding in the World*, vol. 54, no. 7, pp. R208–R217, 2010. [Online]. Available: https://doi.org/10.1007/BF03263506

[25] H. C. Yildirim, G. B. Marquis, and Z. Barsoum, "Fatigue assessment of high frequency mechanical impact (hfmi)-improved fillet welds by local approaches," *International Journal of Fatigue*, vol. 52, pp. 57–67, 2013. [Online]. Available: https://doi.org/10.1016/j.ijfatigue.2013.02.014

[26] H. C. Yıldırım, M. Leitner, G. B. Marquis, M. Stoschka, and Z. Barsoum, "Application studies for fatigue strength improvement of welded structures by high-frequency mechanical impact (hfmi) treatment," *Engineering Structures*, vol. 106, pp. 422–435, 2016. [Online]. Available: https://doi.org/10.1016/j.engstruct.2015.10.044

[27] I. Weich, T. Ummenhofer, T. Nitschke-Pagel, K. Dilger, and H. Eslami Chalandar, "Fatigue behaviour of welded high-strength steels after high frequency mechanical post-weld treatments," *Welding in the World*, vol. 53, no. 11, pp. R322–R332, 2009. [Online]. Available: https://doi.org/10.1007/BF03263475

[28] E. Harati, L.-E. Svensson, L. Karlsson, and K. Hurtig, "Effect of hfmi treatment procedure on weld toe geometry and fatigue properties of high strength steel welds," *Procedia Structural Integrity*, vol. 2, pp. 3483–3490, 2016, 21st European Conference on Fracture, ECF21, 20-24 June 2016, Catania, Italy. [Online]. Available: https://doi.org/10.1016/j.prostr.2016.06.434

[29] G. B. Marquis and Z. Barsoum, *IIW Recommendations for the HFMI Treatment: For Improving the Fatigue Strength of Welded Joints*, ser. IIW Collection. Singapore: Springer Singapore Pte. Limited, 2016.

[30] R. Aldén, Z. Barsoum, T. Vouristo, and M. Al-Emrani, "Robustness of the HFMI techniques and the effect of weld quality on the fatigue life improvement of welded joints," *Welding in the World*, vol. 64, no. 11, pp. 1947–1956, 2020. [Online]. Available: https://doi.org/10.1007/s40194-020-00974-4

[31] DNV-RP-C203:2019, "Fatigue design of offshore steel structures," DNV, Høvik, NO, Recommended Practice, Sep. 2019, accessed: 21/03/2023.

[32] M. Safari, R. A. de Sousa, and J. Joudaki, "Recent advances in the laser forming process: A review," *Metals*, vol. 10, no. 11, pp. 1–19, 2020. [Online]. Available: https://doi.org/10.3390/met10111472

[33] H. Liu, W. Lin, and M. Hong, "Surface coloring by laser irradiation of solid substrates," *APL Photonics*, vol. 4, no. 5, 2019. [Online]. Available: https://doi.org/10.1063/1.5089778

[34] J. Stavridis, A. Papacharalampopoulos, and P. Stavropoulos, "Quality assessment in laser welding: a critical review," *International Journal of Advanced Manufacturing Technology*, vol. 94, pp. 1825–1847, 2018. [Online]. Available: https://doi.org/10.1007/s00170-017-0461-4

[35] W. M. Steen, *Laser Material Processing*, 4th ed. London: Springer-Verlag London, 2010.

[36] N. B. Dahotre and S. P. Harimkar, *Laser Fabrication and Machining of Materials*, 1st ed. New York, NY: Springer-Verlag, 2008.

[37] K. Godineau, S. Lavernhe, and C. Tournier, "Calibration of galvanometric scan heads for additive manufacturing with machine assembly defects consideration," *Additive Manufacturing*, vol. 26, pp. 250–257, 2019. [Online]. Available: https://doi.org/10.1016/j.addma.2019.02.003

[38] Q. Zhong, X. Y. Tian, X. K. Huang, Z. Q. Tong, Y. Cao, and D. C. Li, "High-accuracy calibration for multi-laser powder bed fusion via in situ detection and parameter identification," *Advances in Manufacturing*, 2022. [Online]. Available: https://doi.org/10.1007/s40436-022-00392-3

[39] A. J. Antończak, B. Stępak, P. E. Kozioł, and K. M. Abramski, "The influence of process parameters on the laser-induced coloring of titanium," *Applied Physics A: Materials Science and Processing*, vol. 115, no. 3, pp. 1003–1013, 2014. [Online]. Available: https://doi.org/10.1007/s00339-013-7932-8

[40] M. Nilsen, F. Sikström, A. K. Christiansson, and A. Ancona, "Monitoring of Varying Joint Gap Width during Laser Beam Welding by a Dual Vision and Spectroscopic Sensing System," *Physics Procedia*, vol. 89, pp. 100–107, 2017. [Online]. Available: https://doi.org/10.1016/j.phpro.2017.08.014

[41] J. Reiner, W. Cieszyński, M. Sidorowicz, M. Wiercioch, and E. Chlebus, "Examples of laser processing control with machine vision feedback," *Solid State Phenomena*, vol. 223, pp. 325–332, 2015.

[42] H. A. Simon, *The sciences of the artificial*, 1st ed. [Cambridge] SE -: [M.I.T. Press], 1969.

[43] K. Peffers, T. Tuunanen, M. A. Rothenberger, and S. Chatterjee, "A design science research methodology for information systems research," *Journal of Management Information Systems*, vol. 24, no. 3, pp. 45–77, 2007. [Online]. Available: https://doi.org/10.2753/MIS0742-1222240302

[44] A. Dresch, D. P. Lacerda, and J. A. V. T. A. T. T. Antunes Jr, "Design Science Research : A Method for Science and Technology Advancement," Cham, 2015.

[45] D. Denyer, D. Tranfield, and van Aken J.E., "Developing design propositions through research synthesis ," pp. 393–413, 2008. [Online]. Available: https://doi.org/10.1177/0170840607088020

[46] J. E. Van Aken, "Management research as a design science: Articulating the research products of mode 2 knowledge production in management," *British Journal of Management*, vol. 16, no. 1, pp. 19–36, 2005.

[47] H. A. Simon, *The sciences of the artificial*, 3rd ed. Cambridge, Massachusetts SE -: The MIT Press, 1996.

[48] A. R. Hevner, S. T. March, J. Park, and S. Ram, "Design Science in Information Systems Research," *MIS Quarterly*, vol. 28, no. 1, pp. 75–105, jul 2004. [Online]. Available: https://doi.org/10.2307/25148625

[49] N. Bayazit, "Investigating Design: A Review of Forty Years of Design Research," *Design Issues*, vol. 20, no. 1, pp. 16–29, 2004.

[50] G. L. Geerts, "A design science research methodology and its application to accounting information systems research," *International Journal of Accounting Information Systems*, vol. 12, no. 2, pp. 142–151, 2011. [Online]. Available: https://doi.org/10.1016/j.accinf.2011.02.004

[51] C. Ernould, J. Schubnell, M. Farajian, A. Maciolek, D. Simunek, M. Leitner, and M. Stoschka, "Application of different simulation approaches to numerically optimize high-frequency mechanical impact (hfmi) post-treatment process," *Welding in the World*, vol. 63, no. 3, pp. 725–738, 2019. [Online]. Available: https://doi.org/10.1007/s40194-019-00701-8

[52] M. Leitner, D. Simunek, S. F. Shah, and M. Stoschka, "Numerical fatigue assessment of welded and HFMI-treated joints by notch stress/strain and fracture mechanical approaches," *Advances in Engineering Software*, vol. 120, pp. 96–106, 2016. [Online]. Available: https://doi.org/10.1016/j.advengsoft.2016.01.022

[53] D. Simunek, M. Leitner, and M. Stoschka, "Numerical simulation loop to investigate the local fatigue behaviour of welded and HFMI treated joints," *IIW Document XIII-WG2–136-13*, pp. 1–14, 2013.

[54] R. Tehrani Yekta, K. Ghahremani, and S. Walbridge, "Effect of quality control parameter variations on the fatigue performance of ultrasonic impact treated welds," *International Journal of Fatigue*, vol. 55, pp. 245–256, 2013. [Online]. Available: https://doi.org/10.1016/j.ijfatigue.2013.06.023

[55] K. Ghahremani, M. Safa, J. Yeung, S. Walbridge, C. Haas, and S. Dubois, "Quality assurance for high-frequency mechanical impact (HFMI) treatment of welds using handheld 3D laser scanning technology," *Welding in the World*, vol. 59, no. 3, pp. 391–400, 2015. [Online]. Available: https://doi.org/10.1007/s40194-014-0210-3

[56] G. Le Quilliec, H. P. Lieurade, M. Bousseau, M. Drissi-Habti, G. Inglebert, P. Macquet, and L. Jubin, "Mechanics and modelling of high-frequency mechanical impact and its effect on fatigue," *Welding in the World*, vol. 57, no. 1, pp. 97–111, 2013. [Online]. Available: https://doi.org/10.1007/s40194-012-0013-3

[57] P. Hammersberg, M. Technology, and H. Olsson, "Statistical evaluation of welding quality in production," *Proceedings of the Swedish Conference on Light Weight Optimized Welded Structures*, pp. 148–162, 2010.

[58] T. Stenberg, Z. Barsoum, E. Åstrand, A. E. Öberg, C. Schneider, and J. Hedegård, "Quality control and assurance in fabrication of welded structures subjected to fatigue loading," *Welding in the World*, vol. 61, no. 5, pp. 1003–1015, 2017. [Online]. Available: https://doi.org/10.1007/s40194-017-0490-5

[59] L. Yang, E. Li, T. Long, J. Fan, Y. Mao, Z. Fang, and Z. Liang, "A welding quality detection method for arc welding robot based on 3D reconstruction with SFS algorithm," *International Journal of Advanced Manufacturing Technology*, vol. 94, pp. 1209–1220, 2018. [Online]. Available: https://doi.org/10.1007/s00170-017-0991-9

[60] H. H. Chu and Z. Y. Wang, "A vision-based system for post-welding quality measurement and defect detection," *International Journal of Advanced Manufacturing Technology*, vol. 86, pp. 3007–3014, 2016. [Online]. Available: https://doi.org/10.1007/s00170-015-8334-1

[61] Y. Han, J. Fan, and X. Yang, "A structured light vision sensor for on-line weld bead measurement and weld quality inspection," *International Journal of Advanced Manufacturing Technology*, vol. 106, no. 5-6, pp. 2065–2078, 2020. [Online]. Available: https://doi.org/10.1007/s00170-019-04450-2

[62] J. Xie, S. Huang, Z. Duan, Y. Shi, and S. Wen, "Correction of the image distortion for laser galvanometric scanning system," *Optics and Laser Technology*, vol. 37, no. 4, pp. 305–311, 2005. [Online]. Available: https://doi.org/10.1016/j.optlastec.2004.04.012

[63] M. F. Chen and Y. P. Chen, "Compensating technique of field-distorting error for the CO2 laser galvanometric scanning drilling machines," *International Journal of*

Machine Tools and Manufacture, vol. 47, pp. 1114–1124, 2007. [Online]. Available: https://doi.org/10.1016/j.ijmachtools.2006.09.015

[64] M. A. Ortega Delgado and A. F. Lasagni, "Reducing field distortion for galvanometer scanning system using a vision system," *Optics and Lasers in Engineering*, vol. 86, pp. 106–114, 2016. [Online]. Available: https://doi.org/10.1016/j.optlaseng.2016.05.016

[65] J. Tu and L. Zhang, "Effective data-driven calibration for a galvanometric laser scanning system using binocular stereo vision," *Sensors (Switzerland)*, vol. 18, no. 1, 2018. [Online]. Available: https://doi.org/10.3390/s18010197

[66] A. Manakov, H. P. Seidel, and I. Ihrke, "A mathematical model and calibration procedure for galvanometric laser scanning systems," *VMV 2011 - Vision, Modeling and Visualization*, pp. 207–214, 2011. [Online]. Available: https://doi.org/10.2312/PE/VMV/VMV11/207-214

[67] V. T. Le and Y. Quinsat, "In situ calibration of galvanometric scanning head for laser powder bed fusion machines based on a vision system," *International Journal of Advanced Manufacturing Technology*, vol. 111, pp. 1767–1783, 2020. [Online]. Available: https://doi.org/10.1007/s00170-020-06189-7

[68] J. Tu and L. Zhang, "Rapid on-site recalibration for binocular vision galvanometric laser scanning system," *Optics Express*, vol. 26, no. 25, p. 32608, 2018. [Online]. Available: https://doi.org/10.1364/oe.26.032608

[69] T. Wissel, B. Wagner, P. Stüber, A. Schweikard, and F. Ernst, "Data-driven learning for calibrating galvanometric laser scanners," *IEEE Sensors Journal*, vol. 15, no. 10, pp. 5709–5717, 2015. [Online]. Available: https://doi.org/10.1109/JSEN.2015.2447835

[70] R. Indhu, V. Vivek, S. Loganathan, A. Bharatish, and S. Soundarapandian, "Overview of Laser Absorptivity Measurement Techniques for Material Processing," *Lasers in Manufacturing and Materials Processing*, vol. 5, no. 4, pp. 458–481, 2018. [Online]. Available: https://doi.org/10.1007/s40516-018-0075-1

[71] P. Drude, "Zur Elektronentheorie der Metalle," *Annalen der Physik*, vol. 306, no. 3, pp. 566–613, 1900. [Online]. Available: https://doi.org/10.1002/andp.19003060312

[72] E. Hagen and H. Rubens, "Über Beziehungen des Reflexions- und Emissionsvermögens der Metalle zu ihrem elektrischen Leitvermögen," *Annalen der Physik*, vol. 316, no. 8, pp. 873–901, 1903. [Online]. Available: https://doi.org/10.1002/andp.19033160811

[73] L. K. Ang, Y. Y. Lau, R. M. Gilgenbach, and H. L. Spindler, "Analysis of laser absorption on a rough metal surface," *Applied Physics Letters*, vol. 70, no. 6, pp. 696–698, 1997. [Online]. Available: https://doi.org/10.1063/1.118242

[74] M. S. K. Blidegn and F. O. Olsen, "Investigation into the absorptivity change in metals with increased laser power," *XI International Symposium on Gas Flow and Chemical Lasers and High-Power Laser Conference*, vol. 3092, p. 615, April 1997. [Online]. Available: https://doi.org/10.1117/12.270146

[75] J. T. Wang, C. I. Weng, J. G. Chang, and C. C. Hwang, "The influence of temperature and surface conditions on surface absorptivity in laser surface treatment," *Journal of Applied Physics*, vol. 87, no. 7, pp. 3245–3253, 2000. [Online]. Available: https://doi.org/10.1063/1.372331

[76] H. Wang, Y. Kawahito, R. Yoshida, Y. Nakashima, and K. Shiokawa, "A model to calculate the laser absorption property of actual surface," *International Journal of Heat and Mass Transfer*, vol. 118, pp. 562–569, 2018. [Online]. Available: https://doi.org/10.1016/j.ijheatmasstransfer.2017.11.023

[77] D. Bergström, "The absorption of laser light by rough metal surfaces," Ph.D. dissertation, Luleå University of Technology, 2008.

[78] H. Kügler and F. Vollertsen, "Determining Absorptivity Variations of Multiple Laser Beam Treatments of Stainless Steel Sheets," *Journal of Manufacturing and Materials Processing*, vol. 2, no. 4, p. 84, 2018. [Online]. Available: https://doi.org/10.3390/jmmp2040084

[79] K. Ikeuchi and K. Sato, "Determining reflectance properties of an object using range and brightness images," *IEEE transactions on pattern analysis and machine intelligence*, vol. 13, no. 11, pp. 1139–1153, 1991. [Online]. Available: https://doi.org/10.1109/34.103274

[80] X. Li and Y. Liang, "Remote measurement of surface roughness, surface reflectance, and body reflectance with LiDAR," *Applied Optics*, vol. 54, no. 30, p. 8904, 2015. [Online]. Available: https://doi.org/10.1364/ao.54.008904

[81] ——, "Surface characteristics modeling and performance evaluation of urban building materials using LiDAR data," *Applied Optics*, vol. 54, no. 15, p. 4750, 2015. [Online]. Available: https://doi.org/10.1364/ao.54.004750

[82] W. Huang and R. Kovacevic, "Development of a real-time laser-based machine vision system to monitor and control welding processes," *International Journal of Advanced Manufacturing Technology*, vol. 63, no. 1-4, pp. 235–248, 2012. [Online]. Available: https://doi.org/10.1007/s00170-012-3902-0

[83] ——, "A laser-based vision system for weld quality inspection," *Sensors*, vol. 11, no. 1, pp. 506–521, 2011. [Online]. Available: https://doi.org/10.3390/s110100506

[84] M. de Graaf, R. Aarts, B. Jonker, and J. Meijer, *Real-Time Trajectory Generation for Sensor-Guided Robotic Laser Welding*. IFAC, 2006, vol. 39, no. 15. [Online]. Available: https://doi.org/10.3182/20060906-3-IT-2910.00065

[85] ——, "Real-time seam tracking for robotic laser welding using trajectory-based control," *Control Engineering Practice*, vol. 18, no. 8, pp. 944–953, 2010. [Online]. Available: https://doi.org/10.1016/j.conengprac.2010.04.001

[86] W. Cieszyński, M. Zięba, and J. Reiner, "Real time trajectory correction system of optical head in laser welding," *Acta Mechanica et Automatica*, vol. 9, no. 4, pp. 265–269, 2015. [Online]. Available: https://doi.org/10.1515/ama-2015-0042

[87] X. Gao, X. Zhong, D. You, and S. Katayama, "Kalman filtering compensated by radial basis function neural network for seam tracking of laser welding," *IEEE Transactions on Control Systems Technology*, vol. 21, no. 5, pp. 1916–1923, 2013. [Online]. Available: https://doi.org/10.1109/TCST.2012.2219861

[88] R.-K. Zäh, B. Mosbach, J. Hollwich, and B. Faupel, "Modelling and control for laser based welding processes: modern methods of process control to improve quality of laser-based joining methods," *High-Power Laser Materials Processing: Applications, Diagnostics, and Systems VI*, vol. 10097, p. 100970A, 2017. [Online]. Available: https://doi.org/10.1117/12.2248909

[89] S. Portnov, I. Israfilov, A. Perestoronin, A. Grigoryants, and V. Zvezdin, "A system for automatic control of precision laser welding in engineering," *Welding International*, vol. 29, no. 10, pp. 801–804, 2015. [Online]. Available: https://doi.org/10.1080/09507116.2014.986884

[90] D. Hoyle, *Automotive Quality Systems Handbook : ISO/TS 16949:2002 Edition*. Oxford, UNITED KINGDOM: Elsevier Science and Technology, 2005.

[91] M. L. Smith, L. N. Smith, and M. F. Hansen, "The quiet revolution in machine vision - a state-of-the-art survey paper, including historical review, perspectives, and future directions," *Computers in Industry*, vol. 130, p. 103472, 2021. [Online]. Available: https://doi.org/10.1016/j.compind.2021.103472

[92] V. Alonso, A. Dacal-Nieto, L. Barreto, A. Amaral, and E. Rivero, "Industry 4.0 implications in machine vision metrology: An overview," *Procedia Manufacturing*, vol. 41, pp. 359–366, 2019. [Online]. Available: https://doi.org/10.1016/j.promfg.2019.09.020

[93] E. N. Malamas, E. G. Petrakis, M. Zervakis, L. Petit, and J. D. Legat, "A survey on industrial vision systems, applications and tools," *Image and Vision Computing*, vol. 21, no. 2, pp. 171–188, 2003. [Online]. Available: https://doi.org/10.1016/S0262-8856(02)00152-X

[94] H. Golnabi and A. Asadpour, "Design and application of industrial machine vision systems," *Robotics and Computer-Integrated Manufacturing*, vol. 23, no. 6, pp. 630–637, 2007. [Online]. Available: https://doi.org/10.1016/j.rcim.2007.02.005

[95] C. R. H. Barbosa, M. C. Sousa, M. F. L. Almeida, and R. F. Calili, "Smart Manufacturing and Digitalization of Metrology: A Systematic Literature Review and a Research Agenda," *Sensors*, vol. 22, no. 16, 2022. [Online]. Available: https://doi.org/10.3390/s22166114

[96] J. Beyerer, F. P. León, and C. Frese, *Machine vision: Automated visual inspection: Theory, Practice and Applications*, 1st ed. Springer Publishing Company, Inc., 2015.

[97] A. Haleem, M. Javaid, R. P. Singh, S. Rab, R. Suman, L. Kumar, and I. H. Khan, "Exploring the potential of 3D scanning in Industry 4.0: An overview," *International Journal of Cognitive Computing in Engineering*, vol. 3, pp. 161–171, August 2022. [Online]. Available: https://doi.org/10.1016/j.ijcce.2022.08.003

[98] L. Fan, F. Zhang, H. Fan, and C. Zhang, "Brief review of image denoising techniques," *Visual Computing for Industry, Biomedicine, and Art*, vol. 2, no. 1, p. 7, dec 2019. [Online]. Available: https://doi.org/10.1186/s42492-019-0016-7

[99] M.-J. Rakotosaona, V. La Barbera, P. Guerrero, N. J. Mitra, and M. Ovsjanikov, "Pointcleannet: Learning to denoise and remove outliers from dense point clouds," *Computer Graphics Forum*, vol. 39, no. 1, pp. 185–203, 2020. [Online]. Available: https://doi.org/10.1111/cgf.13753

[100] G. Kumar and P. K. Bhatia, "A detailed review of feature extraction in image processing systems," *International Conference on Advanced Computing and Communication Technologies, ACCT*, pp. 5–12, 2014. [Online]. Available: https://doi.org/10.1109/ACCT.2014.74

[101] L. Kabbai, M. Abdellaoui, and A. Douik, "Image classification by combining local and global features," *Visual Computer*, vol. 35, no. 5, pp. 679–693, 2019. [Online]. Available: https://doi.org/10.1007/s00371-018-1503-0

[102] S. U. Rehman, K. F. Thang, and N. S. Lai, "Automated PCB identification and defect-detection system (APIDS)," *International Journal of Electrical and Computer Engineering*, vol. 9, no. 1, pp. 297–306, 2019. [Online]. Available: https://doi.org/10.11591/ijece.v9i1.pp297-306

[103] R. S. Peres, X. Jia, J. Lee, K. Sun, A. W. Colombo, and J. Barata, "Industrial Artificial Intelligence in Industry 4.0 -Systematic Review, Challenges and Outlook," *IEEE Access*, pp. 220 121–220 139, 2020. [Online]. Available: https://doi.org/10.1109/ACCESS.2020.3042874

[104] L. Wendler, D. Löschner, I. Engelhardt, G. Telljohann, C. Große-Soetebier, T. Sigmund, and M. Neher, "Automatisierte schweißnahtnachbehandlung durch höherfrequentes hämmern," *Stahlbau*, vol. 92, no. 7, pp. 418–426, 2023. [Online]. Available: https://doi.org/10.1002/stab.202300021

Part III

Papers

Paper A

Development of an Automated System for Adaptive Post-weld Treatment and Quality Inspection of Linear Welds

Anders Faarbæk Mikkelstrup, Morten Kristiansen, and Ewa Kristiansen

The paper has been published in the
International Journal of Advanced Manufacturing Technology, vol. 119,
pp. 3675–3693, 2022.

The International Journal of Advanced Manufacturing Technology (2022) 119:3675–3693
https://doi.org/10.1007/s00170-021-08344-0

ORIGINAL ARTICLE

Development of an automated system for adaptive post-weld treatment and quality inspection of linear welds

Anders F. Mikkelstrup[1] · Morten Kristiansen[1] · Ewa Kristiansen[1]

Received: 2 July 2021 / Accepted: 3 November 2021 / Published online: 8 January 2022

Abstract

High-frequency mechanical impact (HFMI) treatment is a well-documented post-weld treatment to improve the fatigue life of welds. Treatment of the weld toe must be performed by a skilled operator due to the curved and inconsistent nature of the weld toe to ensure an acceptable quality. However, the process is characterised by noise and vibrations; hence, manual treatment should be avoided for extended periods of time. This work proposes an automated system for applying robotised 3D scanning to perform post-weld treatment and quality inspection of linear welds. A 3D scan of the weld is applied to locally determine the gradient and curvature across the weld surface to locate the weld toe. Based on the weld toe position, an adaptive robotic treatment trajectory is generated that accurately follows the curvature of the weld toe and adapts tool orientation to the weld profile. The 3D scan is reiterated after the treatment, and the surface gradient and curvature are further applied to extract the quantitative measures of the treatment, such as weld toe radius, indentation depth, and groove deviation and width. The adaptive robotic treatment is compared experimentally to manual and linear robotic treatment. This is done by treating 600-mm weld toe of each treatment type and evaluating the quantitative measures using the developed system. The results showed that the developed system reduced the overall treatment variance by respectively 26.6% and 31.9%. Additionally, a mean weld toe deviation of 0.09 mm was achieved; thus, improving process stability yet minimising human involvement.

Keywords Weld toe treatment · 3D scanning · Point cloud processing · Computer vision · Process automation · Robotics

Nomenclature

Symbol	Description	Units
$\boldsymbol{u}$	Scanned 2D profile of the weld (x, y, z)	mm
$\boldsymbol{U}$	Point cloud of the scanned weld (x, y, z)	mm
n	Number of points per scanned profile $\boldsymbol{u}$	1
m	Number of scanned profiles $\boldsymbol{u}$	1
$\boldsymbol{\theta}'$	Local gradients of point cloud	1
$\boldsymbol{\theta}''$	Local curvatures of point cloud	mm^{-1}
$\boldsymbol{w}_\theta$	Penalisation weights for curvature	1
$\tilde{\boldsymbol{w}}_\theta$	Normalised penalisation weights for curvavture	1
$\hat{\boldsymbol{\theta}}''$	Penalised local curvatures	mm^{-1}
ψ	Travelling angle relative to direction of travel	°
ϕ	Working angle relative to surface of weld	°
$\boldsymbol{\Omega}$	Weld toe positions (x, y, z)	mm
$\boldsymbol{\Gamma}_w$	Groove edge position matrix (weld side)	mm
$\boldsymbol{\Gamma}_b$	Groove edge position matrix (base meta side)	mm
γ_w	Groove edge position (weld side)	mm
γ_b	Groove edge position (base metal side)	mm
W	Groove width	mm
D_w	Indentation depth (weld side)	mm
D_b	Indentation depth (base metal side)	mm
R	Weld toe radius	mm
ϵ	Groove deviation from weld toe	mm

✉ Anders F. Mikkelstrup
afm@mp.aau.dk

Morten Kristiansen
morten@mp.aau.dk

Ewa Kristiansen
ewa.kristiansen@yahoo.com

[1] Department of Materials and Production, 9220 Aalborg, Denmark

1 Introduction

Welded regions in metal structures have a lower fatigue life than the base material. This is mainly caused by local stress concentrations along the weld toe arising from high tensile residual stresses appearing when the weld solidifies and cools down. Additionally, stress concentrations can be caused by notches appearing from the weld geometry, and weld imperfections [1]. Various post-weld techniques have been invented to improve the fatigue life of welds. These techniques apply standard industrial processes, such as burr grinding, tungsten inert gas (TIG) dressing, shot peening, laser peening and high-frequency mechanical impact (HFMI) techniques as ultrasonic impact treatment (UIT) and pneumatic impact treatment (PIT) [1–8]. The working principles of the treatment techniques are different, but in general they have one or more of the following aims;

- relieving the weld's tensile residual stress zones or even turning them into compressive stress zones,
- smoothening notches,
- suppressing or removing weld defects.

This paper focuses on HFMI treatment of welds for the offshore industry. The method can be adapted to other applications such as the automotive industry and other post-weld techniques, e.g. burr grinding. Burr grinding removes material on a pass along the weld toe, and by doing this, weld defects are removed and concurrently, the stress concentration factor is reduced. By using a burr grinder, the resulting grinding marks are parallel to the load direction, making them act as a prevention for crack initiation [1]. HFMI treatment works by hammering a pin in the weld toe region along the weld at a frequency of > 90 Hz causing plastic deformation of the weld toe, as illustrated in Fig. 1. This process reshapes notches into a smooth geometry along the weld toe and additionally relieves tensile residual stresses in the area and builds up compressive residual stresses [9]. HFMI has been proven to significantly increase fatigue life, regardless of the level of treatment [10]. In a study by E. Harati et al. [11], it was concluded that HFMI treatment could increase fatigue life by 26% in welds of ultra-high-strength steels, while other studies have found similar benefits in mild and high-strength steels [9, 12, 13].

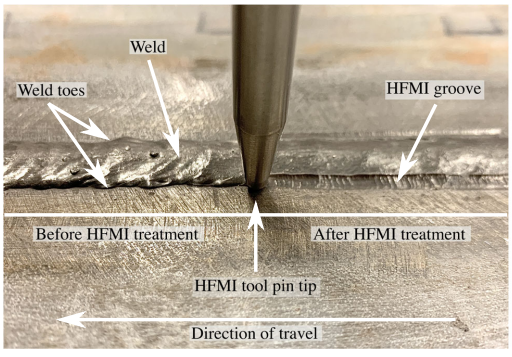

Fig. 1 Weld seen before and after HFMI treatment. It is observed how the treatment has plastically deformed the weld toe into a smooth path, removing sharp notches

The typical industrial way of applying burr grinding and HFMI treatment is manual and based on user experience. Treating more complex geometries, including curvilinear weld toes, has proven to be very demanding and requires more expertise than treating linear welds to ensure an acceptable quality that adheres to the guidelines of G. Marquis and Z. Barsoum [14]. The HFMI treatment tool vibrates, the process is very noisy, and the tool is heavy; therefore, the working environment is not very pleasant for an operator through a continuous eight-hour work shift. Even though operation for eight continuous hours is generally permitted depending on the tool manufacturer, hearing and eye protection is mandatory. An automated solution for post-weld treatment would be highly interesting for the industry to overcome the working environment concerns, and could potentially be economically profitable [15].

Robotising the post-weld treatment is expected to result in higher reliability, repeatability and improved control of the process parameters when compared to manual treatment [16]. Moreover, robotising the treatment could in itself lead to a more efficient treatment as clamping the tool, or mounting it onto a robot, has shown to result in a scatter band of compressive forces that are 50% narrower than manual operation while maintaining or improving the impact force [16–18]. Utilising a robot further enables maintaining a constant speed and controlled impact angle along the weld.

Studies on robotising the post-weld treatment are yet limited. The authors of R. Yekta et al. [10] and K. Ghahremani et al. [19] compared robotic treatments along straight trajectories to manual reference treatments. The purpose of robotising the treatment was, in this case, not focused on improving treatment quality but to minimise bias in the treatments. The results showed that the measured radius of the treated area, the indentation depth (base metal side) and indentation depth (weld side) of the robotic treatment of R. Yekta et al. [10] had a scatter that was respectively $\approx 145\%$, $\approx 197\%$ and $\approx 80\%$ larger than that of the manual treatment. A similar result was achieved by K. Ghahremani et al. [19], where the scatter of the measured radius of the robotically treated area was more than 100% larger than the comparable manual treatment. This more considerable scatter is in both cases believed to be a result of the robot's inability to adapt to the inconsistency of the

weld like a manual operator would, which negatively affects the quality of the post-treatment.

Not adapting to the weld profile can further result in treating perpendicular to the base material. Therefore, hitting the sides of the weld creates folds, thus further degrading the fatigue performance of the weld [20]. Hence, the current solution for robotic HFMI treatment is inferior to manual treatment, indicating why a robotic solution has not yet been developed. By adapting to the weld and thereby not following a generic straight trajectory, it is possible to develop a solution that can reduce scatter in the treatments and achieve process stability comparable to or better than manual treatment. Improved process stability is here defined as a reduction in the variance of the quantitative measures, e.g. indent depth and groove width and radius of the treated area.

Several researchers have investigated methods for automatic trajectory generation to treat parts with nonconformities using a range of vision methodologies and setups. The authors of O. Gurdal et al. [21] have developed a solution for robotic finishing of friction stir-welded corner joints that utilises a laser line scanner mounted to an industrial robot to generate a 3D model of the part. The 3D model is further used to locate the workpiece and automatically generate a robot path to treat the component. H. Zhang et al. [22] have developed a hybrid approach that utilises a 2D camera in combination with a force sensor to automatically generate robot programs that can follow a free-form surface for manufacturing tasks. However, none of these methods have been utilised for automatic post-treatment of welds.

Performing the automated post-weld treatment itself is one challenge; performing automated quality assurance is another. For quality assurance of post-weld treatment, methods and guidelines for recommended execution exist, such as G. Marquis and Z. Barsoum [14] and G. Marquis and Z. Barsoum [15]. These guidelines for HFMI treatment include recommendations related to, e.g. working speed and travelling and working angles.

The quantitative measures are typically evaluated using simple manual gauges and follow the same principles that are applied, when evaluating weld geometries. These gauges can only measure a single point at a time and are often associated with significant variance. P. Hammersberg and H. Olsson [23] studied the resulting variance when using a gauge for measuring throat thickness and depth of undercut in welds. The authors was concluded that the gauge itself contributed to almost 60% of the total variance due to manual operation. When making binary Go/No Go decisions, a standard requirement states that the measurement system should not contribute with more than 9% of the total variation [24]. Hence, the need for a measurement system that does not rely on a simple manual gauge for accurate quality assurance of post-treated welds is clear.

Several researchers have studied methods for non-contact measurements of treated and non-treated welds with the purpose of quality assurance. L. Yang et al. [25] proposed a method for determining weld quality by state vector machine (SVM) classification on 3D images that have been reconstructed using the shape from shading (SFS) algorithm. This method does not perform any direct weld measurements but classifies the overall quality, e.g. incomplete fusion and inadequate penetration. T. Stenberg et al. [24] proposed a system for online quality control and assurance of welds using a laser line scanner. The system showed a significant improvement in measurement variation when compared to manual measuring methods. Other authors have applied laser line scanners to measure weld profiles and detect weld defects by extracting feature points using various methods, e.g. through second-order differentiation of the weld profile [26–28]. However, the above methods are only designed for quality assurance of welds and do not focus on post-treatment of welds and quality assurance thereof.

K. Ghahremani et al. [19] have utilised a handheld 3D scanner as a method for quality assurance of HFMI treatment to evaluate the quantitative measures as defined by G. Marquis and Z. Barsoum [15]. The authors found that point cloud based measurements of the indentation depth could successfully be used to determine the treatment level: undertreated, properly treated or overtreated. However, the proposed method is based on manual processing of the point cloud data to perform the measurements, which is unsuitable for an automated solution.

It can be concluded from the literature review that automated HFMI treatment shows excellent potential as a method for improving the stability of the post-weld treatment and the reliability of the subsequent quality assurance. However, the current solutions for robotic HFMI treatment are inferior to manual HFMI treatment. This is mainly due to the robotic treatment trajectory not being adapted to the weld but performed along a straight line with constant travelling and working angles. Automatic robotic trajectory generation has to the authors' knowledge, currently not been developed for HFMI treatment of welded components. It can additionally be concluded that there exists a research gap in automated quality assurance for HFMI treatment, as the current methods rely either on simple manual gauges or manual processing of 3D point clouds of the weld surface. Nevertheless, methods have been proposed for evaluating the quality of the weld itself, however, not for post-weld treatment.

To overcome the challenges of the current solutions, this paper proposes an integrated software and hardware system that can automatically perform robotic post-weld

treatment and post-treatment quality assurance based on 3D scanning. The intended purpose of the developed system is to perform automated flexible post-weld treatment of welds in an industrial setting which allows for improved process stability and quality assurance.

There are two main contributions of this paper. The first contribution is the development of an algorithm that can accurately and automatically locate the weld toe based on 3D surface information of the weld, such as the weld profile's gradient and curvature. This information is used to generate an adaptive robotic trajectory for performing post-weld treatment, which follows the inconsistencies of the weld toe and adapts the travelling and working angle to the weld profile. The second contribution is further research of the algorithm such that it can locate the treated area and evaluate the treatment quality by determining the quantitative quality measures, such as indentation depth, groove width and deviation from the weld toe. The developed algorithm is implemented in a generalised software and hardware framework that combines automated post-weld treatment and quality assurance in a flexible production setup.

The proposed solution was experimentally verified by performing post-weld treatment on 600 mm of weld toe based on the adaptive robotic treatment trajectory generated by the developed system. To evaluate the performance of the system, comparable treatments were performed manually and using a linear robotic trajectory. As the developed system accurately followed and adapted the treatment trajectory to the weld toe, it showed a significant improvement in the overall process stability compared to the linear robotic treatment. Only moderate quality improvements were shown compared to the manual treatment performed by a human operator. However, due to the robot performing the treatment, the working environment was vastly improved for the human operator.

The paper is structured as follows: Section 2 gives an introduction to the developed system and architecture. Section 3 presents the methodology for filtering the raw point cloud from the 3D scanner for data processing. Section 4 presents the first main contribution; the method for locating the weld toe and generating the adaptive treatment trajectories. Section 5 presents the second main contribution; the proposed approach for determining the quantitative measures for the treated weld toe. Section 6 presents the experimental setup that is used to test and validate the developed system. Section 7 presents and discusses the obtained results, while Section 8 summarises the conclusions and reflects upon future work.

2 System description and architecture

The developed system relies on a combination of software and hardware operations, as shown in the flow chart, Fig. 2. The system takes the welded part as input and follows the five main steps, as described below:

I A 3D scanner mounted onto an industrial manipulator is utilised to acquire a point cloud of the weld along a linear, manually programmed trajectory. The result is a 3D point cloud representing the surface of the sample as a closely spaced grid of x, y and z coordinates.

II The acquired point cloud is analysed to locate the weld toes to treat. This information is used to generate a set of process instructions, such that the treatment is adapted to the inconsistencies of the weld and adheres to the guidelines for recommended execution [14].

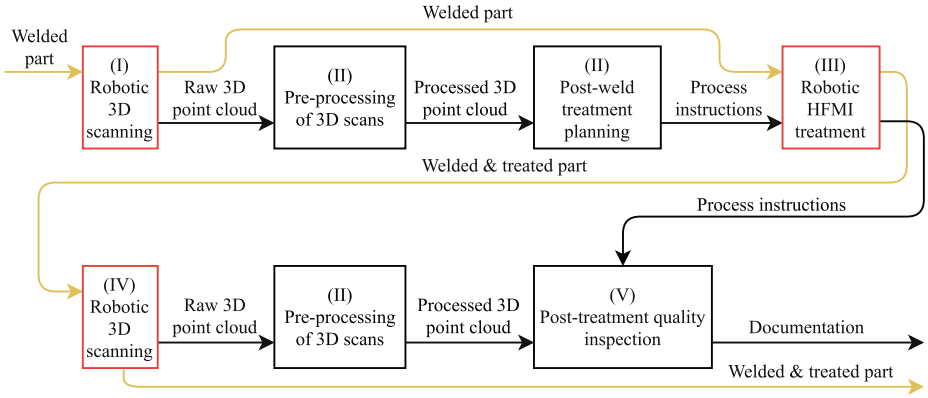

Fig. 2 Architecture of the developed system. Yellow arrows indicate flow of material. Black arrows indicate flow of data. Red boxes represent physical operations. Black boxes represent software for data processing

III Based on the generated process instructions, the post-weld treatment is automatically performed using an industrial manipulator.
IV Following the treatment, the weld is rescanned using the same linear robotic trajectory as in step I.
V The acquired point cloud is analysed to locate the treated groove. The quantitative measures of the treated groove, i.e. indentation depth, weld toe radius and deviation from weld toe, are evaluated, and quality documentation is generated.

Therefore, the system's output is the treated part, documentation of the treatment and quantitative quality measures. The individual steps will be further described in the following sections.

3 Pre-processing of 3D scans

The system requires the scanned data to be arranged in a 2D grid form. Furthermore, the scan must be performed so that the grid lines are parallel or perpendicular to the weld. For this reason, a line scanner that works by applying the principles of laser triangulation is utilised. In the case of the line scanner, the scan should be performed along a linear trajectory at a constant speed. The scanner should be oriented such that the scan line (x-direction) is perpendicular to the length of the weld, while the scanning direction (y-direction) should be parallel to the length of the weld. The resulting z-direction is normal to the surface of the weld. An example of a scan is seen in Fig. 3.

Due to the nature of the line scanner, the data is acquired as m number of scanned profiles, each consisting of n number of points with a distance between each point of dx; defined as the x-resolution. All of the scan lines are parallel with a homogeneous spacing of dy, defined as the y-resolution. As the grid does not determine the z-values, the spacing is continuous. To accurately locate the weld toe, the required x- and z-resolution of the system is <50 µm, while the required resolution in the y-direction is <1000 µm to compare the irregularities of the weld toe.

This means that each of the scan lines represents a 2D profile $\boldsymbol{u}$ of the weld, as illustrated by the red line in Fig. 3, which combined constitute the entire point cloud of the scan $\boldsymbol{U}$. Finally, the scans have been performed such that each scan contains a single, continuous weld with both welds toes. To remove noise and outlying points from the point cloud, a 2D median filter is applied. The 2D median filter is a well known non-linear filter known to preserve edges while removing noise. It works by sliding a window over a neighbouring region and returning the median value of that region. To reduce numerical noise in the succeeding steps, a low-pass Butterworth filter is used independently on each acquired line to smooth the data further.

4 Developed algorithm for post-weld treatment planning

The weld toe, as seen in Fig. 1, is defined as the junction of base material to weld face, which can be empirically observed as a sudden change in the surface gradient along

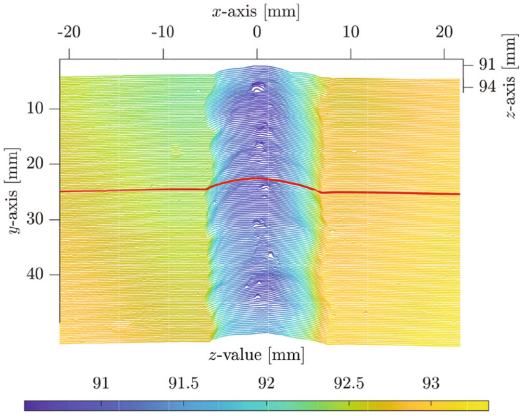

Fig. 3 Point cloud from a scanned weld before treatment consisting of closely spaced 2D weld profiles. A random weld profile is highlighted as the red line. Note that the parts of the point cloud that do not contain the weld have been removed; hence, the y-axis does not start from 0. Furthermore, the distance values of the z-axis indicate the distance to the origin of the scanner

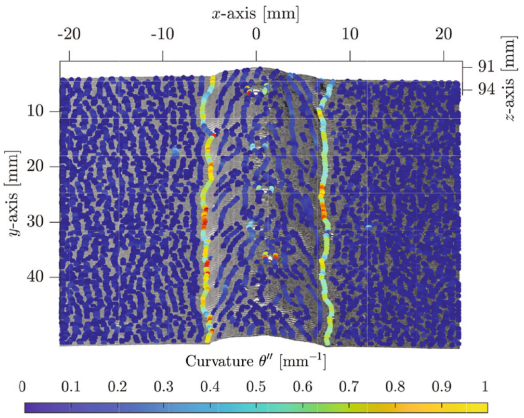

Fig. 4 The local peaks of the curvature $\boldsymbol{\theta}''$ plotted across the entire point cloud. Scan noise and other surface irregularities will present themselves as randomly distributed points, while the distinct lines of connected and semi-clustered points in the scan are the weld toes and other distinct regions

with the profile of the weld. To locate the weld toe in the point cloud of the scan, the gradients $\boldsymbol{\theta}'$ and curvatures $\boldsymbol{\theta}''$ along and between each of the weld profiles are determined. This approach is inspired by Y. Li et al. [26] and Y. Han et al. [27], who both apply second-order information to perform weld bead measurement.

As each scan line represents a weld profile, each weld profile is described as a discrete set of points; therefore, $\boldsymbol{\theta}'$ and $\boldsymbol{\theta}''$ are vectors that can be mathematically expressed by first and second-order finite approximations, defined by Eqs. 1 and 2. To minimise noise and acquire as much information as possible, central difference approximations using a 3-point 1D stencil are applied.

$$\theta'_{i,j} = \frac{U_{i+1,j} - U_{i-1,j}}{2dx} + \frac{U_{i,j+1} - U_{i,j-1}}{2dy}$$
$$\text{for} \quad i = 2, 3, \ldots, n-1, \; j = 2, 3, \ldots, m-1 \tag{1}$$

$$\theta''_{i,j} = \frac{U_{i+1,j} - 2U_{i,j} + U_{i-1,j}}{dx^2} + \frac{U_{i,j+1} - 2U_{i,j} + U_{i,j-1}}{dy^2}$$
$$\text{for} \quad i = 2, 3, \ldots, n-1, \; j = 2, 3, \ldots, m-1 \tag{2}$$

As the point cloud consists of a set of closely spaced weld profiles, j defines the index of the weld profile in the y-direction, such that U_{j+1} is the adjacent weld profile to U_j. i defines the index of the point in the x-direction along with the weld profile of U_j. The coordinate system is presented in Fig. 3. In the following, the proposed methods will focus on a single weld profile $\boldsymbol{u}$ at a random index j. However, these methods will be applied for all weld profiles $\boldsymbol{U}$ for $j = 2, 3, \ldots, m-1$, unless otherwise specified. Hence, the index j will be omitted for the sake of simplicity.

In an optimal case, the two weld toes will be represented as the two global negative peaks of the curvature $\boldsymbol{\theta}''$ along with the weld profile. Though, as the weld quality, notches and other surface variations affect the weld toes' prominence, these can result in a peak curvature more significant than that at the weld toes. The same problem applies for multi-pass welds, where the curvature at the interpasses can also be more significant than that at the weld toes. This issue is illustrated in Fig. 4, where the local peaks of the curvature $\boldsymbol{\theta}''$ are plotted onto the scan of the weld.

The challenge associated with determining which peak curvatures belong to the weld toes is further apparent from Fig. 4. The first step to resolve this issue is to assume that the gradient $\boldsymbol{\theta}'$ of the weld profile near the weld toe approaches zero. This is a valid approach, as it has been observed through more than 50 scanned weld toes following the above-mentioned scanning approach, that the weld toe has a semi-circular geometry in which the gradient of its tangent at some point along the weld toe geometry approaches zero. It has further been observed, that the approach is insensitive

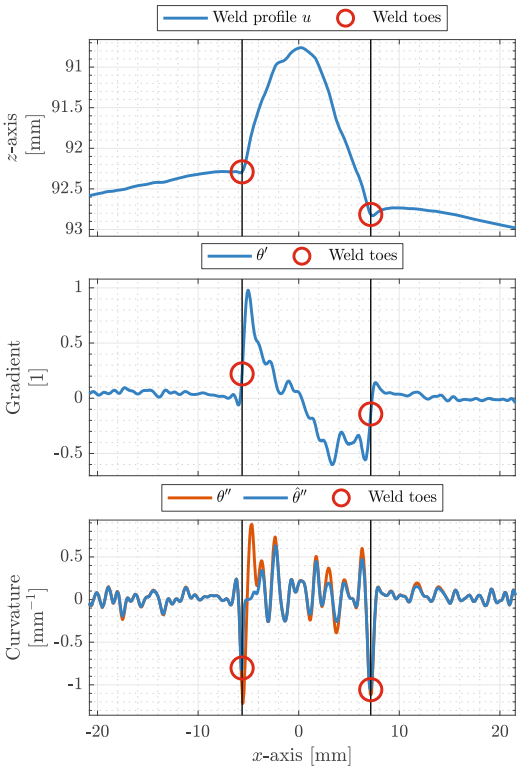

Fig. 5 The processing stages of each of the scanned profiles. The weld toe location is illustrated on the weld profile as the circled points, which lie at the local negative peaks of the penalised curvature $\hat{\boldsymbol{\theta}}''$. Note that using the largest peaks of the curvature $\boldsymbol{\theta}''$ itself would lead to an incorrect estimation of the weld toe

to small rotations around the y-axis of the local coordinate system (Fig. 4) of the point cloud.

The extracted weld profile further illustrates this in Fig. 5, middle graph, where it can be seen, that the gradient $\boldsymbol{\theta}'$ approaches zero, as we move closer to the weld toe. Using a normal probability density function, Eq. 3, it is possible to determine a set of weights $\boldsymbol{w}_\theta$ to penalise the curvature values according to their associated gradients.

$$\boldsymbol{w}_\theta = f\,(\boldsymbol{\theta}|\mu_0, \sigma) = \frac{1}{\sigma\sqrt{2\pi}} \exp \frac{-(\boldsymbol{\theta}' - \mu_0)^2}{2\sigma^2} \tag{3}$$

In Eq. 3, μ_0 is mean of the applied density function, which is set to 0, as this is the gradient $\boldsymbol{\theta}'$ to aim for. σ is the standard deviation or spread of the density function, that determines how the gradients are penalised. As the total area under the probability density curve is equal to 1, the penalty values of $\boldsymbol{w}_\theta$ must be normalised to ensure that a gradient of 0 is not

penalised (see Eq. 4):

$$\tilde{\boldsymbol{w}}_\theta = \frac{\boldsymbol{w}_\theta}{\sigma\sqrt{2\pi}} \tag{4}$$

the penalised curvature $\hat{\boldsymbol{\theta}}''$ can therefore be expressed by Eq. 5

$$\hat{\boldsymbol{\theta}}'' = \|\tilde{\boldsymbol{w}}_\theta\| \circ \boldsymbol{\theta}'' \tag{5}$$

The bottom graph of Fig. 5 represents the penalised curvature $\hat{\boldsymbol{\theta}}''$ as the blue line, where the two most significant negative peaks have been circled. In an optimal case, the most significant penalised curvature peaks will represent the weld toes. Though, due to scan noise and local surface variations, this is not always the case. Based on the assumption that the weld toe forms a continuous line in the y-direction of the scan, the peak penalised curvatures representing the weld toe should likewise form a continuous line in the scan. As some scanned profiles will not correctly represent the location of the weld toes due to noise, these must be omitted.

To ensure continuity in the determined peak penalised curvatures, several continuous reference regions (blue regions of Fig. 6) must be established to define in which areas the weld toes should be located. This is initially done by dividing the scan into several sections (divided by the red lines of Fig. 6), each having q number of weld profiles depending on the y-resolution of the scan. Computing the mean of the q number of weld profiles in each section will result in a mean profile of each section, where non-continuous local peak curvatures such as notches and other local surface variations are filtered out as a result.

A search algorithm based on the principles proposed by E. Moore [29] that finds the shortest path in a weighted graph is applied. Through this approach, it is possible to select the most significant peak curvatures of the mean profiles that form continuous lines through the scan with the smallest x-offset between them. The selected peak curvatures will act as the centres ρ (yellow lines of Fig. 6) of the reference regions. The results are illustrated in Fig. 6, where five continuous reference regions have been found. Curvatures $\hat{\boldsymbol{\theta}}''$ outside of the reference regions will be ignored, as these are assumed to be a result of noise.

As each weld toe can be described by a point on the weld profile, a single point within each of the reference regions across each weld profile must be determined. In the case of Fig. 6, a total of five points per profile $\boldsymbol{u}$ must be located, as five continuous lines have been found through the scan. These five points are selected based on a weighting of the peak curvatures in each reference region and their corresponding distances Δp to the centre of that region, computed as a Euclidean norm. The weights are based on Δp and estimated following the same principles as Eq. 3, again setting $\mu_0 = 0$, as this is the distance to

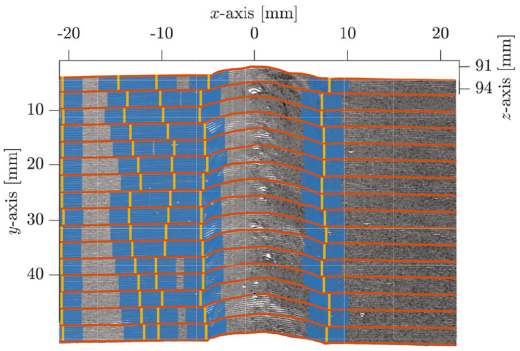

Fig. 6 The scan divided by the red lines into separate sections of $q = 10$ weld profiles. The vertical yellow lines define the continuous peaks of the curvature between the mean profiles. The blue areas are the reference regions in which the weld toes should be located

approach. As a result, the five points that have the best balance between penalised curvature $\hat{\boldsymbol{\theta}}''$ and distance to the reference centres are selected. This operation is performed for all weld profiles $\boldsymbol{U}$ for $j = 2, 3, \ldots, m-1$, such that five continuous lines are located through the weld.

As there are only two weld toes, the remaining three obsolete lines must be removed. The mean values of the curvatures $\hat{\boldsymbol{\theta}}''$ for all $j = 2, 3, \ldots, m-1$ are determined. Initially, the lines with a mean curvature below a predetermined threshold value are removed. These are typically the lines in the inherently flat base material, as the curvature here will be low. The remaining lines will hence lay in or at the edge of the weld material. As the weld toe

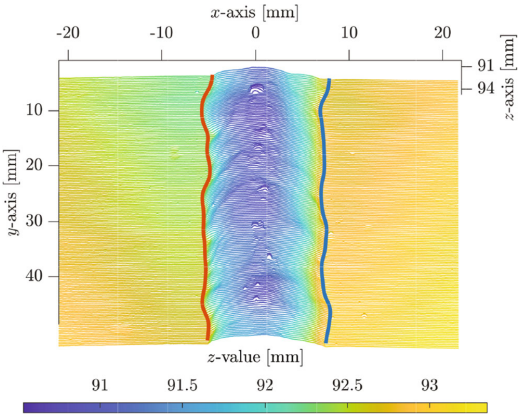

Fig. 7 The determined continuous lines through the scan. The blue and red lines are the determined weld toes that have been smoothed using a smoothing spline. Identical colour notation is used throughout the remainder of the paper, such that the red lines refer to the left weld toe, while the blue lines refer to the right

is characterised as the transition between base and weld material, the two lines that are the furthest away from the centre of the weld, one on each side of the weld, are considered the two weld toes. The result is plotted as the red and blue lines in Fig. 7. Smoothing splines are applied on the estimated positions to filter and further improve the robustness and accuracy of the algorithm, resulting in a $m - 1 \times 3$ vector $\boldsymbol{\Omega}$ of (x, y, z) coordinates for each weld toe for all weld profiles $\boldsymbol{U}$. The result is plotted as the blue and oranges lines in Fig. 7.

4.1 Treatment trajectory generation

According to the guidelines proposed by G. Marquis and Z. Barsoum [15], the treatment must also be performed with a specified set of angles that have been defined relative to the surface of the weld and travelling direction (Fig. 8).

Therefore, the surrounding points around the weld toes are used to determine the required tool orientation along the treatment trajectory. The travelling angle ψ is defined with respect to the direction of travel and computed based on the change in curvature of the along with the weld toe (see Eq. 6). As the treatment must be performed with a travelling angle ψ within a specified interval, a reference angle ψ_0 is set. The reference angle is based on operator experience and does generally not vary between similar welds.

$$\psi_i = \psi_0 + \text{atan2}\left(\frac{\Omega.x_i - \Omega.x_{i-1}}{\Omega.y_i - \Omega.y_{i-1}}\right) \quad i = 2, 3 \ldots m - 2 \quad (6)$$

$$\phi_i = \eta_{b_i} + \eta_{w_i} - \phi_0 \quad \text{for} \quad i = 1, 2 \ldots m - 2 \quad (7)$$

The working angle ϕ is defined with respect to the surface of the base metal is computed by fitting two linear lines starting from the weld toe and pointing in the opposite direction; one line in the direction of the base material and the other line in the direction of the weld. Each line is fitted with the number of points that transverse across a distance equivalent to the HFMI tool pin tip radius. This is done to ensure that the fitted lines represent the area of which the tool hits the weld. A reference angle of $\phi_0 = 90°$ relative to the surface is used, as this is the angle to apply for a completely flat surface. The working angle is then computed as Eq. 7.

η_b is the angle of the fitted line across the base metal, while η_w is the angle of the fitted line across the weld metal. The computed angle ϕ_i is further constrained by the recommended range stated by the IIW recommendations [14]. The computed angles can be seen in Fig. 9.

The computed working angles and travelling angles have been smoothed using a smoothing spline. This is done to minimise rapid changes in the angles during treatment that will be difficult for the robot to follow.

In order to generate the HFMI trajectory for the robot, the estimated positions of the weld toes and the treatment angles are transformed using a transformation matrix from the local coordinate system of the scanner to the global coordinate system of the robot. The required transformation matrix is determined through a simple calibration based on global reference points from the robot and local reference points from the scanner. By touching a set of reference points with the TCP of the HFMI tool on the robot and subsequently scanning the same points and locating them in the 3D scan, it is possible to apply a non-linear least-square optimisation to compute the transformation. The HFMI tool is also calibrated to the robot, which is done by applying

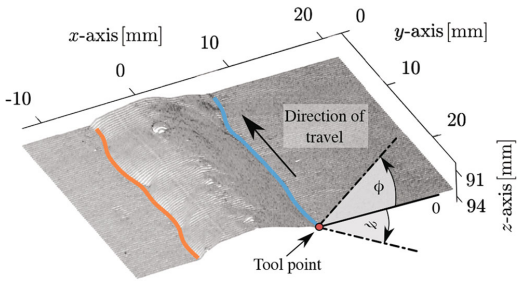

Fig. 8 Illustration of the treatment angles. The working angle ϕ is defined with respect to the surface of the base metal. The travelling angle ψ is defined with respect to the direction of travel

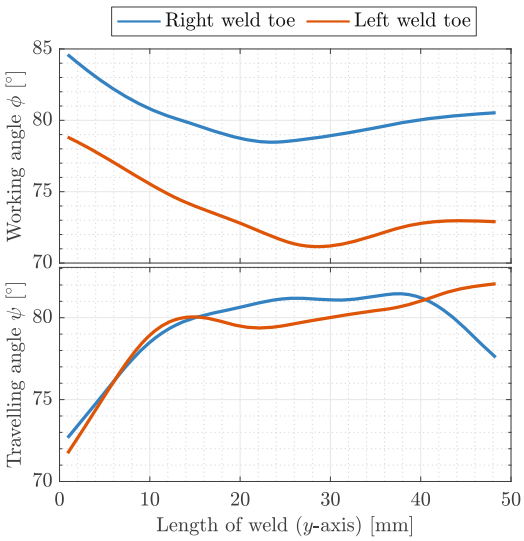

Fig. 9 The generated treatment angles based on the surface of the weld and the curvature of the weld toe. The computed working angle ϕ and travelling angle ψ for the two weld toes

a 4-point calibration procedure implemented in the robot's controller.

This calibration operation must be performed, when changes or maintenance have been done to the scanner or tool. Having determined the global coordinates of the weld toe, a robot program can automatically be generated, hence limiting the amount of manual programming.

5 Developed algorithm for post-weld treatment quality inspection

As defined by G. Marquis and Z. Barsoum [15], the quality of the treatment and the resulting groove can be assessed based on two measures: qualitative (I) and quantitative (II).

I The qualitative measures are based on a visual inspection and evaluate the quality of the groove. E.g. the groove must be continuous, smooth and shiny and without a visual presence of the original fusion line. These are clear visual differences between the levels of treatment: under, over and properly treated R. Yekta et al. [10]. Flaking type damage can also be observed in cases of high coverage rates, i.e. two passes or low-speed [20].

II The quantitative measures, as illustrated in Fig. 14, are directly measurable. These include the indentation depth (base metal side) D_b and groove width W, where the indentation depth has proven to be an excellent measure for quality assurance [19]. The optimal indentation depth (base metal side) D_b and groove width W depend on the material and tool, but should be between 0.2 and 0.6 mm in depth and 3 and 6 mm in width. However, the minimum D_b should be between 0.1 and 0.2 mm to ensure a complete HFMI treatment. Similar guidelines apply for the HFMI treatment groove location, which must be placed such that 25–75% of its width is in the weld material. It should be noted, that the recommendations serve as guidelines and depend on several factors, including the yield strength of the welded steel. [14].

The focus will be placed on the quantitative measures, as these can be directly measured using a 3D scanner. The weld is therefore rescanned post-treatment, utilising the same scanning trajectory and principles as the pre-treatment scan.

The scans must be aligned in the same coordinate system to compare the weld before and after treatment. Aligning two point clouds is done using the iterative closest point algorithm (ICP), originally proposed by K. Arun et al. [30], which searches for a set of reference points between two point clouds. A non-linear optimisation then follows to determine the transformation between the two 3D point clouds.

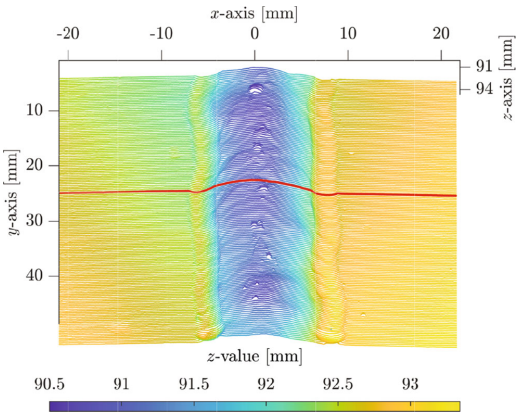

Fig. 10 Point cloud from a scanned weld post-treatment. A profile of the treated weld is highlighted as the red line. Note that the scanned section is that same as for the untreated weld in Fig. 7

Pre-processing of the scan for determining the quantitative measures follows the same methods, as described in Section 3. The resulting scan of a peened weld is presented in Fig. 10.

On an extracted single profile $\boldsymbol{u}$, illustrated in Fig. 11, the peened grooves can be identified as two semi-circles, constrained by sharp edges on each side of the grooves. Mathematically, the edges are described as a sudden change

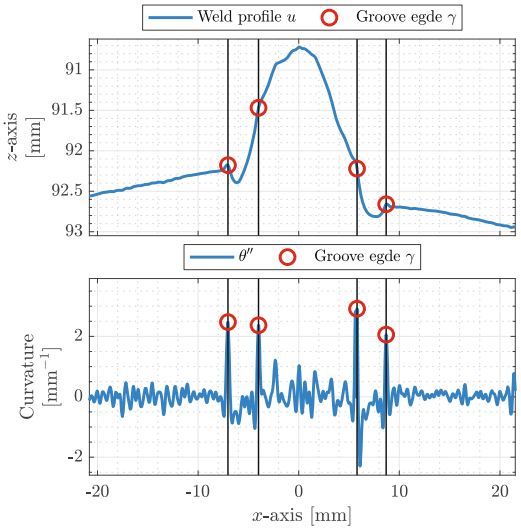

Fig. 11 The processing stages of each of the scanned profiles. The groove edges' locations are highlighted on the weld profile with red cirlces and can be associated with the local peak of the curvature at the indicated points

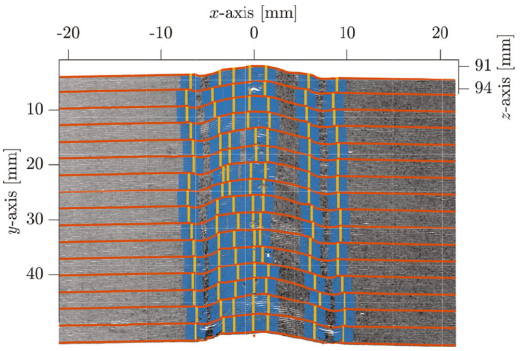

Fig. 12 The scan divided into separate sections of weld profiles by the red lines. The yellow lines define the continuous peaks of the curvature between the mean profiles, while the blue area is the reference region in which the groove edges should be located. In this case, there are seven references regions

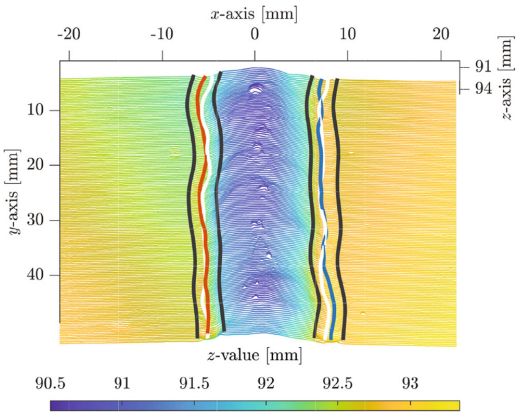

Fig. 13 The located HFMI treatment grooves in the scanned point cloud. The black lines indicate the positions of each of the groove edges. The red and blue lines are the located groove positions used to determine the error ϵ for respectively the left and right weld toe. The whites line are the positions of the weld toes Ω before treatment

in the surface gradient perpendicular to the length of the groove. Applying Eq. 1 to determine the curvature across the scanned surface is, therefore, the first step. However, as the curve that forms the groove edge points away from the weld, the curvature will have the opposite sign than the weld toe. Therefore, the aim is to find the most significant positive curvatures. In this case, the gradient is not used as a weighting parameter, as this has been shown to influence the results negatively.

As with the weld toes, the four largest peak curvatures would represent the four edges of the two grooves in an optimal case. Yet, due to notches and other surface noise, the four largest peak curvatures might not always represent the peened grooves' edges. The approach for selecting the correct peak curvatures on each weld profile follows the same method as for the weld toes, described in Section 4; hence a number of reference regions that form continuous lines through the scan are determined and then used to constrain the area in which the curvature peaks should be located. The result can be seen in Fig. 12.

In this instance, seven continuous lines are formed through the reference regions. As there are only four edges for the two grooves, three lines must therefore be removed. The approach again follows the same principles as for the weld toes. In this case, it is the four lines furthest away from the weld with mean curvatures above a pre-determined threshold that define the groove edges; two on each side of the weld. Therefore, each peened groove will have $m-1\times 3$ Γ_w and $m-1\times 3$ Γ_b matrices containing the groove edge positions γ_w and γ_b for respectively the weld side and base metal side. These are plotted as the black lines in Fig. 13. The estimated groove positions, further described in Section 5.1, are plotted as the blue lines in Fig. 13. The position of the weld toes before treatment are plotted as the white lines in Fig. 13.

5.1 Determining the quantitative measures

Having located each groove of the treated weld toes, the quantitative measures can be determined. The quantitative measures are illustrated in Fig. 14 and determined for all weld profiles $\boldsymbol{U}$ and both peened grooves. The groove for

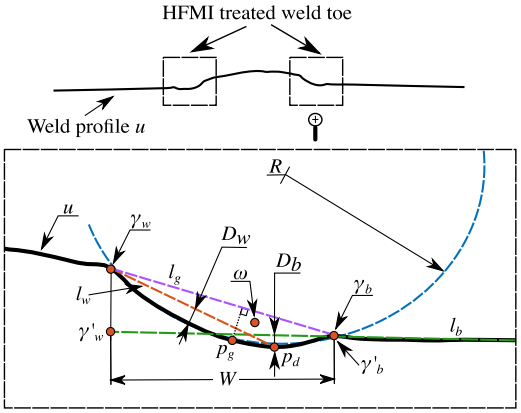

Fig. 14 The quantitative measures based on the IIW recommendation, G. Marquis and Z. Barsoum [14], for HFMI treatment and the measures proposed by K. Ghahremani et al. [19]. The measurements are performed on both the left and right cut out just mirrored. W is the groove width, D_b the Indentation depth (base metal side), D_w the indentation depth (weld side), R is the weld toe radius and ω is the position of the weld toe before treatment

each weld toe is found on the weld profile $\boldsymbol{u}$ between the indexes I_w and I_b which, respectively, define the groove edge (weld side) and groove edge (base metal side).

Groove width W: The indentation width is computed by fitting a line l_b to the surface of the base metal and projecting the positions of the groove edge (weld side) γ_w and the groove edge (base metal side) γ_b onto the fitted line. If l_b is described by two points, p_0 and p_1, the point γ_w can be projected onto I_b using a vector projection, presented by Eq. 8. The same principle applies to the projection of γ_b.

$$\gamma_w' = p_0 + \frac{\overrightarrow{p_0\gamma_w} \cdot \overrightarrow{p_0p_1}}{\overrightarrow{p_0p_1} \cdot \overrightarrow{p_0p_1}} \cdot \overrightarrow{p_0p_1} \tag{8}$$

The Euclidean distance between the two projected points is, therefore, the groove width W (see Eq. 9).

$$W = \|\gamma_w' - \gamma_b'\| \tag{9}$$

Indentation depth (base metal side) D_b: The Euclidean distance from the point p_d in the groove at index I_d with the largest perpendicular distance to the fitted line l_b is used as the indentation depth D_b of the base metal side. The perpendicular distances $\boldsymbol{S}$ for all points in the groove is determined through Eq. 10.

$$\boldsymbol{S} = \frac{\sqrt{|\overrightarrow{p_0p_1}|^2|\overrightarrow{p_0u_i}|^2 - (\overrightarrow{p_0p_1} \cdot \overrightarrow{p_0u_i})^2}}{\|\overrightarrow{p_0p_1}\|} \quad \text{for} \quad i = 1, \ldots, n-1 \tag{10}$$

Therefore, the indentation depth D_b of the base metal side can be expressed by Eq. 11, while the corresponding index I_d and point p_d can be expressed by Eq. 12.

$$D_b = \max_i\{S_i : I_b, \ldots, I_w\} \tag{11}$$

$$I_d = \arg\max_i\{S_i : I_b, \ldots, I_w\} \implies p_d = S_{I_d} \tag{12}$$

Indentation depth (weld side) D_w: The indentation depth (weld side) is based on the metric presented in K. Ghahremani et al. [19]. A line l_w is spanned between the point p_d in the groove and the groove edge on the weld side γ_w. The Euclidean distance from the point in the groove, constrained by p_d and γ_w, that has the largest perpendicular distance to l_w is used as the indentation depth D_s of the weld side. Computation follows the same methods as for the indentation depth on the base metal sides; hence the indentation depth is expressed through Eq. 13.

$$D_w = \max_i\{S_i : I_d, \ldots, I_w\} \tag{13}$$

Weld toe radius R: The weld toe radius R is determined by applying the Hyper fit method to fit a circle to the points along with the weld profile $\boldsymbol{u}$, that constitutes the groove constrained by γ_w and γ_b. The Hyper fit method, proposed by Ali Al-Sharadqah and Nikolai Chernov [31], is an algebraic fit that is computationally inexpensive and not subject to divergence, opposite to a geometric fit. Additionally, the method benefits from having a higher accuracy and lower sensitivity to noise than other competing methods [31].

Groove vs weld toe (error) ϵ: To establish the groove deviation from the weld toe, a reference position for the groove must be determined. It is assumed that the contact point of the tool tip constitutes the deepest point p_g in the groove, measured as the largest perpendicular distance from the line l_g spanned by γ_w and γ_b. Determining p_g follows the same principles as p_d, and it is based on Eqs. 10, 11 and 12. By projecting both p_g and the position of the corresponding weld toe ω onto the line l_g, based on Eq. 8, the treatment deviation from the weld toe can be expressed as the difference between the two projected points p_g' and ω' (see Eq. 14).

$$\epsilon = \|p_g' - \omega'\| \cdot \text{sgn}(p_g'.x - \omega'.x) \tag{14}$$

As the quantitative measures are automatically determined, a documentation report for the treatment is further automatically generated.

6 Experimental setup

The adaptive robotic HFMI treatment is evaluated by being compared to a linear robotic treatment and to a manual treatment. The adaptive HFMI treatment uses the developed system to automatically generate the treatment trajectory, such that the treatment accurately follows the weld toe and varies the working angle ϕ and travelling angle ψ along the trajectory. The linear HFMI treatment was programmed manually; therefore, the HFMI tool follows a linear trajectory based on the weld toe position at the start and end of the weld. For the linear trajectory, the travelling and working angles were kept constant throughout the treatment. All trajectories were programmed so that the robot moves in a continuous forward motion at a constant velocity.

The manual treatment is performed by a trained human operator with varying speed, treatment and working angles according to the operator's assessment, who simultaneously aims to stay within the recommended limits stated by IIW [14]. Unlike the robot, the human operator moves in a back and forward motion when performing the treatment. It should be noted, that the chosen speed for all treatments was

Table 1 Parameters for scanning and HFMI treatment

Scanning				
Parameter	Axis	Working range [mm]	Resolution [µm]	Speed [mm s^{-1}]
Scan width	*x*	30–52	17–26	
Scan length	*y*	50	300	
Scan height	*z*	70–130	2–4.9	
Acquisition	*xyz*			50
HFMI treatment				
Parameter	Pin radius [mm]	Treatment angle [°]	Working angle [°]	Speed [mm s^{-1}]
Adaptive robotic	2	70†	15†	2.5
Linear robotic	2	70*	15*	2.5
Manual	2	∼60	∼20	∼2.5

†Treatment angle is based on the given reference angle and adjusted in relation to the surface around the weld toe

*Fixed reference angle

below the IIW recommendation, as it was concluded to be necessary to ensure a proper treatment depth.

The experimental setup for testing the system consists of a KUKA KR60-3 industrial robot used to manipulate both the 3D scanner and the PITEC Weld Line 10-06 HFMI tool. The 3D scanner is a Wenglor MLWL131 laser line scanner and works based on the principles of laser triangulation. The scans are performed along a linear trajectory parallel to the weld with a constant speed, orientation and distance to the workpiece. The equipment and parameters for the experiments are specified in Table 1.

The treatments are performed on a sample of two S355 300 × 1500 mm steel plates, each with a thickness of 20 mm, that have been welded together using gas metal arc welding in a double-sided joint configuration. This creates a 1500-mm weld with two weld toes, each split into 50-mm sections with a spacing of 10 mm. The workpiece and welding equipment are further detailed in Table 2. The

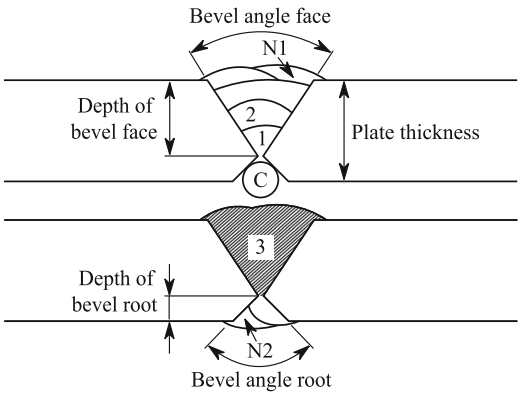

Fig. 15 The welding sequence along with the groove geometry. Note that (C) specifies the ceramic backing. Further details are outlined in Table 3

Table 2 Workpiece and equipment

Parameter	Specification
Workpiece	
Material	S355NL/ML
Plate thickness	20 mm
Plate width	300 mm
Plate length	1500 mm
Groove	V
Bevel angle face	50°
Bevel angle root	50°
Depth of bevel face	15 mm
Depth of bevel root	5 mm
Resulting weld toes	2
Welding position	Upside down
Welding equipment	
Welding machine	Migatronic Sigma 500
Manipulation	Welding tractor
Gas nozzle diameter	14 - 16 mm
Gas mixture	82/18 Ar/CO_2
Gas flow rate	18 - 22 l min^{-1}
Wire type	NITTETSU SF-3AM
Wire diameter	1.2 mm
Backing	Ceramic Ø8
Scanning and HFMI equipment	
Manipulator	KUKA KR 60-3
Scanner	Wenglor MLWL131
HFMI tool	PITEC Weld Line 10-06

Table 3 Welding process parameters

Run	Arc	Pole	Current [A]	Voltage [V]	Stickout [mm]	Travel speed [mm s^{-1}]	Max. weaving [mm]	Heat input [kJ mm^{-1}]
1	Spray	DC+	250	24	15–20	120	13	2.40
2-N1	Spray	DC+	250	24	15–20	200	12	1.44
3-N2	Spray	DC+	250	24	15–20	200	12	1.44

welding parameters are given in Table 3 along with the welding sequence, illustrated in Fig. 15. Each treatment type was performed on the two weld toes of six sections, resulting in 300 mm of weld or 600 mm of weld toe per treatment type. As the weld toes were less prominent on the root side of the weld, the treatments were performed on the root side making it more challenging for the developed system to correctly identify and locate the weld toes.

The experimental setup is illustrated in Figs. 16 and 17.

7 Results and discussion

Application of the developed system results in a significant decrease in programming time for the robot than manually programming the HFMI treatment path. The proposed system only requires programming the robot scanning trajectory, which is identical pre- and post-treatment. Programming can be done through both online and offline programming based on a CAD model of the part. The total programming time per treated weld sample with the developed system was around 2 min, while manually programming the linear trajectory was more than 10 min for both toes of the weld. In cases where there are similar parts, the scanning trajectories for the developed system can be reused and thus the programming time is reduced further. This is not the case for the manually programmed treatment trajectory as no individual weld is unique; thus, the treatment trajectories must be reprogrammed for each weld.

Figure 18 shows an example of a weld, that has been treated using the developed system. It can be observed that the HFMI tool has adapted to the weld toe along the treatment trajectory. Figure 19 shows the resulting

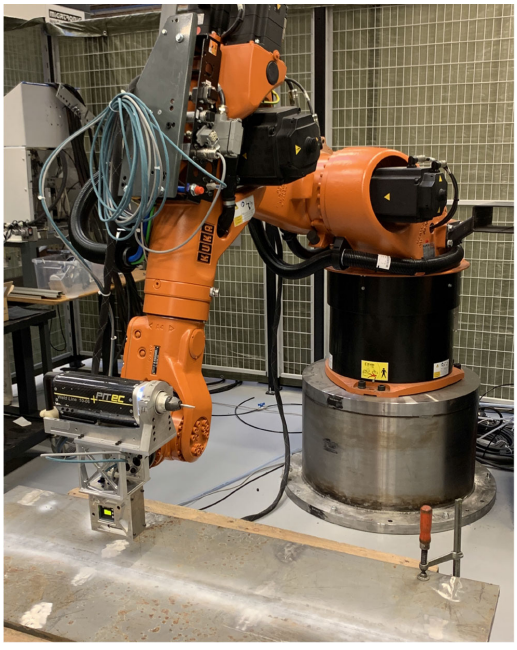

Fig. 16 Scanning of the weld using an industrial robot. This is done before and after the treatment

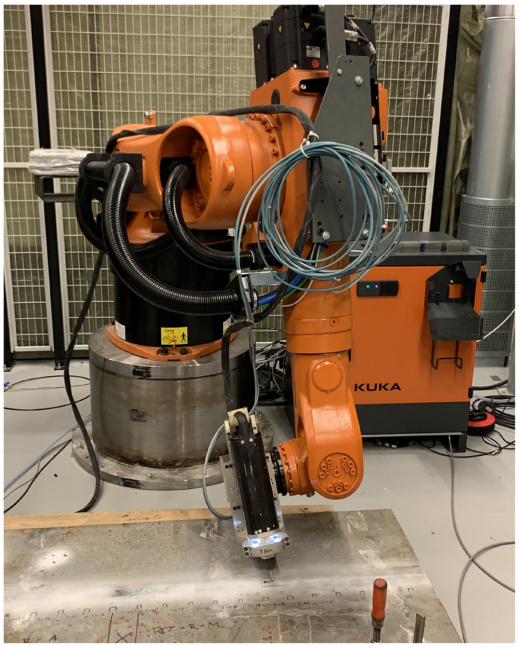

Fig. 17 Performing robotised HFMI treatment of the welded sample

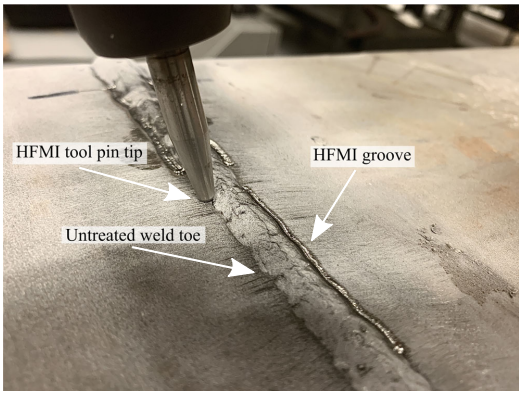

Fig. 18 HFMI treated weld using an automatically generated treatment trajectory. Note how the the robot has adapted to the curvature of the weld using the information from the 3D scan. This acts as empirical validation for the performance of the developed system

quantitative measures for the treated weld, which act as documentation for the treatment quality. It should be noted, that in this case, the indentation depth (base metal side) is not within the recommended limits set by IIW [14]. However, this problem could be solved by performing the treatment at a lower speed.

7.1 Quantitative measurements of the treatments

The quantitative measurements have been evaluated based on scans before and after adaptive robotic, linear robotic and manual post-weld treatment.

ANOVA analysis combined with Tukey's Honest Significant Difference (HSD) have been performed for each of the five quantitative measures across the three treatment types: adaptive robotic, linear robotic and manual, all scanned before and after treatment. The results show a statistically significant difference in the means across the treatments when comparing the quantitative measures (e.g. indentation depth and groove width). The only case where two groups were not statistically significant is the linear robotic treatment and the manual treatment, when observing the indentation depth (base metal side). Thus, the measured distribution of the indentation depth (base metal side) is comparable for the manual and linear robotic treatment. However, this could be due to the relatively large variance in the indentation depth (base metal side) of the linear treatment, as presented in the box plot, Fig. 20 and Table 4. Based on the ANOVA analysis, it can be concluded that the treatment types generally lead to different results and can, therefore, be further evaluated.

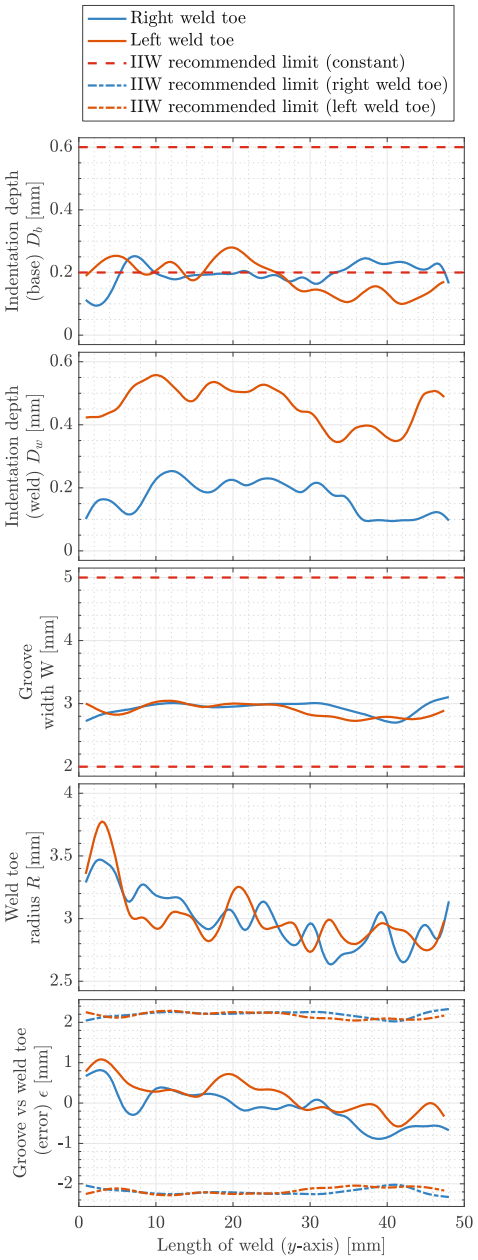

Fig. 19 The quantitative measures plotted along the length of a random weld along with the associated IIW recommendation limits [14]. The IIW recommendation limits for the error ϵ are defined based on the position of the HFMI groove, which varies for the right and left weld toe. Twenty-five to 75% of the total groove width must be in the base metal, which is indicated by the upper and lower limits on the lowest graph

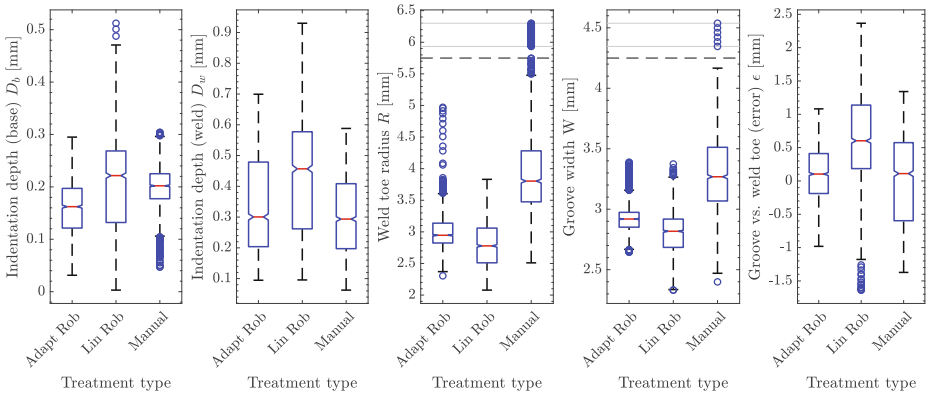

Fig. 20 Box plot of the quantitative measures, illustrating the variance and median of each treatment type. Note the smaller variance of Adapt Rob (adaptive robotic) compared to Lin Rob (linear robotic) across the majority of metrics. This is a clear result of the robot successfully adapting to the weld toe. The circular points are statistical outliers

Figure 20 illustrates a box plot that compares the quantitative measures between the three treatment types. The red line within each box illustrates the median values of the group, while the lower and upper bound of the boxes illustrate, respectively, the first quartile (25th percentile) and the third quartile (75th percentile). The box plot data have automatically been generated using the developed system and is composed of the combined data from all 600 mm of treated weld per treatment type as described in Section 6. Therefore, some of the variances in the measurements can be explained by the natural variance in the welds. The data, that is used to generate Fig. 20, is further summarised in Table 4, while related observations are presented below.

R. Yekta et al. [10] generally observed a significantly lower variance of the manual treatment across all metrics compared to a linear robotic treatment. K. Ghahremani et al. [19] also observed a significant scatter in the measured weld toe radius of the linear robotic treatments compared to the manual treatment. However, in the case of this paper, the standard deviation (square root of variance) of the weld toe radius and groove width of the linear robotic treatment is approximately reduced 50% compared to the manual treatment, as presented in Table 4. This could be explained by the homogeneity and linearity of the treated welds. As the adaptive robotic treatment adapts to the irregularity of the weld toe and adjusts the working and travelling angles relative to the weld profile, the adaptive robotic treatment achieves the lowest variance across almost all metrics except for the indentation depth (base metal and weld side), where the resulting standard deviation is, respectively, 25% and 15.3% higher compared to the manual treatment. Conversely, the absolute difference in the standard deviation of indentation depth (base metal and weld side) is 0.01 mm and 0.02 mm, which is deemed insignificant.

A relatively large mean value and scatter is observed in both the weld toe radius and groove width for the manual treatment. The back-and-forth motion that the operator performs when treating the weld can possibly explain this; hence treating the same area more than once results in an uneven treatment. The vibrations of the tool make it challenging to control, and as a result, the operator might not follow the same trajectory, when moving over a previously treated area.

According to the IIW recommendation for HFMI treatment, G. Marquis and Z. Barsoum [14], the minimum indentation depth (base metal side) should be between 0.1 and 0.2 mm to ensure a complete HFMI treatment. Although, the optimum HFMI treatment indentation depth (base metal side) is between 0.2 and 0.6 mm, while the groove depth should be between 3 and 6 mm. It must be noted that the recommendation stated by G. Marquis and Z. Barsoum [14] serve as guidelines and depend on several factors, including the yield strength of the welded steel. In Fig. 20 it can be observed, that the mean indentation depth (base metal side) for the adaptive robotic treatment of 0.16 mm is within the minimum limits.

As stated by R. Yekta et al. [10], directing the tool at a too high degree towards the weld, opposed to the base metal, equates to a lower indentation depth (base metal side) of the treatment. Reducing the treatment speed could furthermore result in a larger indentation depth (base metal side) of the treatment. The mean groove width of 2.92 mm of the adaptive robotic treatment (Table 4) is marginally below the recommended interval. This could probably be solved by using a larger tool pin tip radius. Factors that influence the measurements, such as the z-axis resolution and pooling of scanning coating in the treated groove, could also affect the results.

Table 4 Results for comparison of adaptive robotic versus linear robotic and manual treatment

Quantitative measures	Mean [mm]			Std. Dev. [mm]			Num. data points		
	Adaptive robotic	Linear robotic	Manual	Adaptive robotic	Linear robotic	Manual	Adaptive robotic	Linear robotic	Manual
Indentation depth (base metal side) D_b	0.16	0.20	0.20	0.05	0.09	0.04	1872	1807	1896
Indentation depth (weld side) D_w	0.34	0.42	0.30	0.15	0.17	0.13	1872	1804	1896
Weld toe radius R	3.00	2.78	4.01	0.28	0.36	0.97	1888	1888	1896
Groove width W	2.92	2.81	3.30	0.11	0.17	0.30	1888	1888	1896
Groove vs weld toe (error) ϵ	0.09	0.65	0.02	0.39	0.72	0.64	1888	1888	1896

From Table 4, it can be observed that the mean error ϵ in the position of the groove vs the weld toe for the adaptive robotic, linear robotic and manual treatment are, respectively, 0.09, 0.65 and 0.02 mm. As the mean error for the adaptive robotic treatment is below 0.1 mm with a standard deviation of 0.39 mm, it is considered acceptable. This further underlines, that the adaptive robotic treatment precisely follows the weld toe. Comparing the mean error and standard deviation (Table 4) of the adaptive robotic to that of the linear robotic treatment illustrates that adaptive robotic treatment results in a significant mean error reduction of 86.2% (0.56 mm) and a reduction in the standard deviation of 45.8% (0.33 mm). As expected, the linear robotic trajectory does not follow the irregularity of the weld toe, which naturally results in positional errors. The mean error of the adaptive robotic treatment compared to the manual treatment is 350% (0.07 mm) larger, while the standard deviation is 64.1% (0.25 mm) lower. The larger mean error in the adaptive robotic treatment could result from calibration tolerances and be lowered with an improved calibration routine. However, the decrease in the error variance when comparing adaptive robotic to manual treatment indicates improved process stability. As an overall summary, the comparison of standard deviation across all metrics is averaged; indicating that the adaptive robotic treatment has a 26.6% and 31.9% overall lower standard deviation compared to, respectively, the manual treatment and the linear robotic treatment. In the case of a more consistent weld of improved appearance and quality it is expected that the standard deviation across all metrics of the adaptive robotic treatment would be further reduced.

It should be noted that the error measurements are based on the computed weld toe positions from the developed system and hence on the assumption that the calculated weld toe positions are correct. Furthermore, assuming that a trained operator can treat the weld toe accurately, a mean error of 0.02 mm would indicate that both the weld toes and the treated grooves are correctly located. Based on these assumptions, the performance of the developed system is validated.

In summary, the adaptive robotic treatment showed substantial improvements compared to the manually programmed linear robotic treatment, as both the mean error ϵ and the variance across all metrics were improved. The adaptive robotic treatment showed considerable potential compared to the manual treatment as the treatment variance across most metrics was improved. Determining the quantitative parameters using 3D scanning has been proven to be a fast and efficient method compared to manually determining the metrics. A large amount of measurements points (> 1000) is achieved with a single pass of the scanner across the weld (pre- and post-treatment) with minimum

human interference. As the measurements are automatically evaluated based on the 3D scan, human bias is further eliminated.

8 Conclusion

An integrated software and hardware system has been developed for performing automated post-weld treatment and post-treatment quality inspection using 3D scanning. A 3D point cloud of the weld was used to compute the gradient and curvature across the weld surface, forming the basis for locating the weld toe. Knowledge of the weld toe position and the surrounding weld surface was used to generate an adaptive robotic treatment trajectory, that accurately follows the curvature of the weld toe and adapts the tool orientation to changes in the weld profile, hence improving process stability. Rescanning the weld post-treatment and further utilising the surface gradient and curvature allowed for extracting the quantitative measures of the treatment: indentation depth (base metal and weld side), groove width and weld toe radius. In addition to the quantitative measures as defined by IIW, G. Marquis and Z. Barsoum [14], the HFMI groove deviation from the located weld toe was further computed to evaluate the accuracy of the system.

The developed system was experimentally tested on welds of S355 mild construction steel. The results were compared to similar treatments performed manually by a human operator and by a robot following a manually programmed linear treatment trajectory. Each treatment type being applied on 600 mm of weld toe. The experimental results were evaluated using statistical metrics and ANOVA analysis in conjunction with Tukey's HSD based on which the following conclusions can be made:

- The ANOVA analysis and Tukey's HSD indicate that the quantitative measurements from the treatment types are generally statistically significant; hence, they result in treatments that statistically differ.
- The automatically generated treatment trajectory that is adapted to the weld toe resulted in a treatment variance, which was the lowest in the majority of the quantitative metrics. The exception was the indentation depth (base metal and weld side), where the standard deviation was 0.01 and 0.02 mm higher, which is deemed insignificant. The averaged standard deviation across all metrics was, respectively, 26.6% and 31.9% lower than manual and linear robotic treatment. In conclusion, the adaptive robotic treatment improved the process stability.
- The manual treatment had a relatively large mean and scatter for both the weld toe radius and groove width. This could be attributed to the operator's back and forth motion during treatment, resulting in uneven treatment and lower process stability.
- The mean groove width for the adaptive robotic treatment was 2.92 mm, which is marginally below the 3 mm recommendation by IIW [14]. The groove width could likely be increased by using a larger tool pin tip radius.
- The trajectory deviation (error) from the weld toe was respectively 0.09 mm, 0.65 mm and 0.02 mm for the adaptive robotic, linear robotic and manual treatment. As the operator is trained, the small error in the manual treatment is used as validation for the developed system's ability to evaluate the quantitative measurements accurately. Additionally, it can be concluded that the adaptive trajectory follows the weld toe as the error is significantly smaller than that of the linear treatment trajectory.

Furthermore, it can be concluded that automatically generating the treatment trajectories based on the developed system is far more efficient than manual programming. The developed system only requires manual programming of the linear scanning program, which is the same for all comparable welds. The system performs as intended and shows an excellent potential for performing post-weld treatment and quality insurance with minimal human involvement.

For future work, it could be interesting to evaluate the quantitative measurements further to identify tool wear and weld defects.

Acknowledgements The authors would like to acknowledge Radoslav Darula for designing the robotic fixture for the HFMI tool.

Author contribution Anders Mikkelstrup: writing, investigation, development, experimental work, methodology and conceptualisation; Morten Kristiansen: conceptualisation, supervision, reviewing and funding acquisition; Ewa Kristiansen: supervision and reviewing.

Funding This study was supported by the Innovation Fund Denmark, project: CeJacket - Create Disruptive solutions for Design and Certification of Offshore Wind Jacket foundations, project number 6154-00017B. The Wenglor MLWL131 3D scanner used for this system was supported by Ørsted A/S.

Availability of data and material The datasets generated and applied to support the findings of this study are available in the Mendeley Data repository with the identifier:
https://doi.org/10.17632/ktcsh7sykv.1

Code availability The code for the developed system is available per request.

Declarations

Conflict of interest The authors declare no competing interests.

References

1. Pedersen MM, Mouritsen OØ, Hansen MR, Andersen JG, Wenderby J (2010) Comparison of post-weld treatment of high-strength steel welded joints in medium cycle fatigue. Weld World 54(7):R208–R217. https://doi.org/10.1007/BF03263506
2. Malaki M, Ding H (2015) A review of ultrasonic peening treatment. Mater Des 87:1072–1086. https://doi.org/10.1016/j.matdes.2015.08.102
3. Yildirim HC, Marquis GB, Barsoum Z (2013) Fatigue assessment of high frequency mechanical impact (hfmi)-improved fillet welds by local approaches. Int J Fatigue 52:57–67. https://doi.org/10.1016/j.ijfatigue.2013.02.014
4. Yildirim HC, Marquis GB (2012) Fatigue strength improvement factors for high strength steel welded joints treated by high frequency mechanical impact. Int J Fatigue 44:168–176. https://doi.org/10.1016/j.ijfatigue.2012.05.002
5. Gerster P, Schäfers F., Leitner M Pneumatic impact treatment (pit)–application and quality assurance. IIW Document XIII-WG2-138-13 pp 2013
6. Mikkola E, Marquis G, Lehto P, Remes H, Hänninen H (2016) Material characterization of high-frequency mechanical impact (hfmi)-treated high-strength steel. Mater Des 89:205–214. https://doi.org/10.1016/j.matdes.2015.10.001
7. Cheng X, Fisher JW, Prask HJ, Gnäupel-Herold T, Yen BT, Roy S (2003) Residual stress modification by post-weld treatment and its beneficial effect on fatigue strength of welded structures. Int J Fatigue 25(9):1259–1269. https://doi.org/10.1016/j.ijfatigue.2003.08.020
8. Gujba A, Medraj M (2014) Laser peening process and its impact on materials properties in comparison with shot peening and ultrasonic impact peening. Materials 7:7925–7974. https://doi.org/10.3390/ma7127925
9. Marquis GB, Mikkola E, Yildirim HC, Barsoum Z (2013) Fatigue strength improvement of steel structures by high-frequency mechanical impact: proposed fatigue assessment guidelines. Weld World 57(6):803–822. https://doi.org/10.1007/s40194-013-0075-x
10. Tehrani Yekta R, Ghahremani K, Walbridge S (2013) Effect of quality control parameter variations on the fatigue performance of ultrasonic impact treated welds. Int J Fatigue 55:245–256. https://doi.org/10.1016/j.ijfatigue.2013.06.023
11. Harati E, Svensson L.-E., Karlsson L, Hurtig K (2016) Effect of hfmi treatment procedure on weld toe geometry and fatigue properties of high strength steel welds, Procedia Structural Integrity 2 (2016) 3483–3490, 21St European Conference on Fracture, ECF21, 20-24 June Catania, Italy. https://doi.org/10.1016/j.prostr.2016.06.434
12. Yıldırım HC, Leitner M, Marquis GB, Stoschka M, Barsoum Z (2016) Application studies for fatigue strength improvement of welded structures by high-frequency mechanical impact (hfmi) treatment. Eng Struct 106:422–435. https://doi.org/10.1016/j.engstruct.2015.10.044
13. Weich I, Ummenhofer T, Nitschke-Pagel T, Dilger K, Eslami Chalandar H (2009) Fatigue behaviour of welded high-strength steels after high frequency mechanical post-weld treatments. Weld World 53(11):R322–R332. https://doi.org/10.1007/BF03263475
14. Marquis GB, Barsoum Z (2016) IIW Recommendations for the HFMI treatment: for improving the fatigue strength of welded joints, IIW collection, springer Singapore pte. Limited, Singapore
15. Marquis G, Barsoum Z (2014) Fatigue strength improvement of steel structures by high-frequency mechanical impact: proposed procedures and quality assurance guidelines. Weld World 58(1):19–28. https://doi.org/10.1007/s40194-013-0077-8
16. Ernould C, Schubnell J, Farajian M, Maciolek A, Simunek D, Leitner M, Stoschka M (2019) Application of different simulation approaches to numerically optimize high-frequency mechanical impact (hfmi) post-treatment process. Weld World 63(3):725–738. https://doi.org/10.1007/s40194-019-00701-8
17. Leitner M, Simunek D, Shah SF, Stoschka M (2018) Numerical fatigue assessment of welded and hfmi-treated joints by notch stress/strain and fracture mechanical approaches. Adv Eng Softw 120:96–106. https://doi.org/10.1016/j.advengsoft.2016.01.022
18. David Simunek MS, Leitner M (2013) Numerical simulation loop to investigate the local fatigue behaviour of welded and hfmi-treated joints, IIW Doc XIII-WG2-136-13 57
19. Ghahremani K, Safa M, Yeung J, Walbridge S, Haas C, Dubois S (2015) Quality assurance for high-frequency mechanical impact (hfmi) treatment of welds using handheld 3d laser scanning technology. Weld World 59(3):391–400. https://doi.org/10.1007/s40194-014-0210-3
20. Le Quilliec G, Lieurade H-P, Bousseau M, Drissi-Habti M, Inglebert G, Macquet P, Jubin L (2013) Mechanics and modelling of high-frequency mechanical impact and its effect on fatigue. Weld World 57(1):97–111. https://doi.org/10.1007/s40194-012-0013-3
21. Gurdal O, Rae B, Zonuzi A, Ozturk E (2019) Vision-assisted robotic finishing of friction stir-welded corner joints. Procedia Manufact 40:70–76. https://doi.org/10.1016/j.promfg.2020.02.013
22. Zhang H, Chen H, Xi N (2006) Automated robot programming based on sensor fusion. Indust Robot An Int J 33(6):451–459. https://doi.org/10.1108/01439910610705626
23. Hammersberg P, Olsson H (2010) Statistical evaluation of welding quality in production. In: Proceedings of the Swedish Conference on Light Weight Optimized Welded Structures, pp 1–17
24. Stenberg T, Barsoum Z, Åstrand E, Öberg AE, Schneider C, Hedegård J (2017) Quality control and assurance in fabrication of welded structures subjected to fatigue loading. Weld World 61(5):1003–1015. https://doi.org/10.1007/s40194-017-0490-5
25. Yang L, Li E, Long T, Fan J, Mao Y, Fang Z, Liang Z (2018) A welding quality detection method for arc welding robot based on 3d reconstruction with sfs algorithm. Int J Adv Manufact Technol 94(1):1209–1220. https://doi.org/10.1007/s00170-017-0991-9
26. Li Y, Li YF, Wang QL, Xu D, Tan M (2010) Measurement and defect detection of the weld bead based on online vision inspection. IEEE Trans Instrum Meas 59(7):1841–1849. https://doi.org/10.1109/TIM.2009.2028222
27. Han Y, Fan J, Yang X (2020) A structured light vision sensor for on-line weld bead measurement and weld quality inspection. Int J Adv Manufact Technol 106(5):2065–2078. https://doi.org/10.1007/s00170-019-04450-2

28. Chu H-H, Wang Z-Y (2016) A vision-based system for post-welding quality measurement and defect detection. Int J Adv Manufact Technol 86(9):3007–3014. https://doi.org/10.1007/s00170-015-8334-1
29. Moore EF (1959) The shortest path through a maze. In: Proceedings of an International Symposium on the Theory of Switching, Harvard University Press. Cambridge, Massachusetts, pp 285-292
30. Arun KS, Huang TS, Blostein SD (1987) Least-squares fitting of two 3-d point sets. IEEE Trans Pattern Anal Mach Intell 9(5):698–700. https://doi.org/10.1109/TPAMI.1987.4767965
31. Al-Sharadqah A, Chernov N (2009) Error analysis for circle fitting algorithms. Electron J Stat 3(none):886–911. https://doi.org/10.1214/09-EJS419

Paper B

Three-Dimensional Scanning Applied for Flexible and In Situ Calibration of Galvanometric Scanner Systems

Anders Faarbæk Mikkelstrup, Georgi Nikolaev Nikolov, and Morten Kristiansen

The paper has been published in
Sensors, vol. 23, no. 2142, pp. 1-19, 2023.

sensors

MDPI

Article

Three-Dimensional Scanning Applied for Flexible and In Situ Calibration of Galvanometric Scanner Systems

Anders Faarbæk Mikkelstrup *, Georgi Nikolaev Nikolov and Morten Kristiansen

Department of Materials and Production, Aalborg University, 9220 Aalborg, Denmark
* Correspondence: afm@mp.aau.dk

Abstract: Galvanometric laser scanner (GLS) systems are widely used for materials processing due to their high precision, processing velocity, and repeatability. However, GLS systems generally suffer from scan field distortions due to joint and task space relationship errors. The problem is further pronounced in robotic applications, where the GLS systems are manipulated in space, as unknown errors in the relative pose of the GLS can be introduced. This paper presents an in situ, data-driven methodology for calibrating GLS systems using 3D scanning, emphasising the flexibility, generalisation, and automated industrial integration. Three-dimensional scanning serves two primary purposes: (1) determining the relative pose between the GLS system and the calibration plate to minimise calibration errors and (2) supplying an image processing algorithm with dense and accurate data to measure the scan field distortion based on the positional deviations of marked fiducials. The measured deviations are used to train a low-complexity Radial Basis Function (RBF) network to predict and correct the distorted scan field. The proposed method shows promising results and significantly reduces the scan field distortion without the use of specialised calibration tools and with limited knowledge of the optical design of the GLS system.

Keywords: three-dimensional scanning; machine vision; automated calibration; galvanometric scanner system; neural network; laser processing

Citation: Mikkelstrup, A.F.; Nikolov, G.N.; Kristiansen, M. Three-Dimensional Scanning Applied for Flexible and In Situ Calibration of Galvanometric Scanner Systems. *Sensors* **2023**, *23*, 2142. https://doi.org/10.3390/s23042142

Academic Editor: Chunhua Yang

Received: 5 January 2023
Revised: 10 February 2023
Accepted: 10 February 2023
Published: 14 February 2023

1. Introduction

Galvanometric laser scanning (GLS) systems allow for the rapid reflection of the laser spot, with high positional repeatability and accuracy. As a result, GLS systems are common within a wide range of applications, including automotive collision avoidance [1], medical imaging [2], and materials processing [3]. This work focuses on robotic laser processing applications, i.e., remote laser cutting, forming, welding, or marking, that require an expanded workspace and more degrees of freedom than what the GLS systems offer.

Typically, GLS systems consist of one or two limited rotatable servo-driven mirrors (galvanometers) and a focusing device. Based on the application, the objective is placed before or after the scanning system, known as pre- and post-objective scanning systems. The pre-objective system utilises an f-theta objective lens to achieve a flat focal plane. The post-objective scanning system employs a dynamic focusing module (DFM) to control the focal length, such that the focus can be maintained in a limited 3D volume [4].

With either scanning system, the relationship between the mirror positions (joint space) and the Cartesian position in the workspace (task space) must be established. However, accurately mapping the joint and task space through the calibration is challenging due to the unknown geometrical, dynamical, optical, and thermal defects of the GLS system [5,6]. The influence of the individual defects varies; however, the thermal effects and the defects from mirrors and their rotary axes are commonly identified as the most significant contributors to laser beam drift [4,5].

Mounting the GLS system on an industrial manipulator adds further complexity to the calibration methodology as the relative pose between the GLS system and the calibration

plane is no longer constant [7]. The overall result is undesirable positioning errors between the nominal and actual positions in the task space, even with a well-designed optical system with low manufacturing tolerances.

Robotised material processing setups are typically equipped with sensor systems for in-line inspection and monitoring. An example of such systems is the use of 3D scanning to ensure that manufactured parts comply with the required geometrical tolerances. Exploiting existing sensor setups for calibrating GLS systems not only serves a practical purpose but also allows for an in situ calibration approach. By performing measurements directly as part of the setup, external measurements that are time-consuming, challenging to automate, and error-prone are avoided [8].

The conventional approach to calibrate GLS systems is to establish the correction or look-up tables (LUT) that define the relationship between the task and joint space. Several variations of the LUT-based approach have been proposed [4,8,9]. The authors of [9] calibrated a pre-objective GLS system for laser drilling by applying Lagrange polynomials to obtain correction tables based on experimental data. The proposed method achieved a calibration accuracy with maximum deviations below 0.05 mm in a 2D setup with a limited work plane of 30 $\times$ 30 mm^2. The authors of [8] instead proposed an in situ calibration method relying on a co-axially coupled vision system. The proposed method was validated using a pre-objective GLS system with a 100 $\times$ 100 mm^2 work plane in a specialised experimental setup. The authors achieved a calibration accuracy of 0.014 mm at a specific reference point through six iterations. However, the applications are limited as the proposed method requires modifications to the existing optical design. The general issue with LUT-based methods is a high computational cost and sensitivity to the amount, and the properties of the experimental data [5,10].

Another approach is constructing a physical model of the GLS system [5,6,11,12]. These methods are categorised as model-driven approaches and generally rely on parameter optimisation based on accurate experimental data acquired either manually or through vision systems. In [5,11], comprehensive physical models were constructed, containing up to 26 fitting parameters that include optical, geometrical, and assembly errors. Relying on the physical model proposed by [5], the authors of [12] developed a vision-based in situ method was developed to calibrate a GLS system for additive manufacturing. The authors achieved a calibration accuracy with maximum deviations below 0.075 mm in a 350 $\times$ 350 mm^2 work plane. It is noted that the ample parameter space often required to construct an accurate physical model leads to computationally heavy, non-convex numerical problems and sensitivity to minor changes in the optical design [13]. The numerical solution is, furthermore, commonly highly dependent on the initial value for the optimiser, requiring strong prior knowledge of the optical and mechanical design of the GLS system [13]. Limited knowledge of the optical design of some commercial GLS systems thereby presents itself as a problem.

Additionally, calibrating GLS systems directly based on traditional camera calibration methods is not possible due to the absence of a single projection centre [11]. Therefore, [14] adapted the camera model to calibrate GLS systems by introducing 12 fitting coefficients. Nevertheless, this approach suffers from similar optimisation problems and relies on the similarity between the GLS system and a camera [7]. It is possible to reduce the modelling complexity while maintaining the calibration accuracy; however, this entails the use of costly high-precision components [15].

Several data-driven methodologies have been proposed that rely on supervised statistical learning methods, such as artificial neural networks (ANN) [7,10,13]. Data-driven methods offer flexibility and depend less on the specific hardware configuration and application. Where model-driven approaches attempt to identify and eliminate sources of variance in the system by constructing a physical model representing said system, data-driven approaches instead aim to compensate for the system variance based on grey/black box models [13]. Data-driven methods have been developed to calibrate GLS systems and have proven to outperform both LUT-based and model-based approaches, both in terms

of the accuracy and practicality [13]. However, the proposed data-driven methods have been used to calibrate GLS systems designed for measurement purposes, which operate under different conditions than industrial GLS systems for material processing. Studies aimed directly towards the data-driven calibration of GLS systems for material processing are limited, and the existing literature has strict requirements for the placement of the calibration plate. Moreover, none of the literature utilises the 3D scanning systems that commonly exist as a part of robotised material processing setups.

Therefore, this paper proposes a generalised and flexible in situ calibration method of GLS systems using 3D scanning, where the emphasis is placed on robotic applications. Initially, 3D scanning is applied to minimize the calibration error by determining and correcting the relative pose between the GLS system and the calibration plane. Using a simple geometrical model to map the joint and task space, fiducials can be laser marked on a calibration plate. By employing 3D scanning to supply accurate and high-density data to a set of image processing techniques, it is possible to determine the positional deviations of the marked fiducials and, thereby, the scan field distortion. Based on the measured positional deviations, a Radial Basis Function (RBF) neural network is trained to predict the necessary positional corrections across the scan field. This allows the nominal positions sent to the scanner to be corrected to compensate for the scan field distortion. The proposed methodology is developed with industrial, focusing on practicality, automation capabilities, and integration into existing systems. Therefore, the method is developed based on a generic GLS system and validated on an industrial robotic laser processing setup.

The advantages of the proposed method can be presented as follows:

- The data acquisition and subsequent calibration of the GLS system can be carried out directly as a part of the setup. The in situ calibration significantly reduces the calibration time and human involvement. The complete calibration and subsequent validation can be performed in less than 10 min.
- The use of 3D scanning to determine the relative pose between the GLS system and the calibration plate entails that only limited prior information related to the placement of the calibration plate is required, offering increased flexibility.
- The use of a simple RBF network allows for a trivial and efficient implementation with a low computational load into the controller of the GLS system. Additionally, the training times are low (≈6 s), allowing for rapid re-calibration.
- The simplified geometrical model relies on limited prior knowledge of the GLS system, underlining the generalisation ability of the proposed method. Moreover, in the case of significant changes to the optical or hardware design of the system, the geometrical model only requires minor adjustments.
- The in situ approach is highly suitable for industrial integration; it offers practicality and presents the achievable in-process accuracy of the system.

This paper is organised as follows: The calibration methodology is provided in Section 2, detailing the data acquisition, the geometrical model used for the task to joint space mapping, the image processing approach employed to identify marked fiducials, and the neural network for predicting and correcting the positional deviations. Section 3 presents the industrial setup on which the proposed method is validated. The resulting calibration accuracy is presented in Section 4, along with a discussion of the contributions and limitations of the proposed method. Finally, the work is concluded in Section 5, and future works are presented.

2. Calibration Methodology

An overview of the proposed generalised and flexible in situ calibration methodology is presented in Figure 1 and summarised below:

1. A plain sheet metal plate serving as the calibration plate is manually placed roughly within the system's workspace. A specialised calibration plate or reference is, hence, not required.

2. A point cloud $\boldsymbol{G_c}$ of the calibration plate is acquired through 3D scanning. The c subscript indicates that the points are given in the coordinate system of the measurement scanner. See Section 2.1.
3. The surface normal $\boldsymbol{V_s}$ and position $\boldsymbol{Y_s}$ of the calibration plate are computed by fitting a plane to the acquired points $\boldsymbol{G_c}$ representing the calibration plate. The s subscript indicates that the points are given in the coordinate system of the GLS system. The overall purpose is to minimise the risk of common calibration errors due to unknown deviations in the relative pose between the GLS system and the calibration plane [8]. Moreover, the need for strict positioning of the calibration plate is avoided. See Section 2.2.
4. To visualise and measure the scan field distortion, a uniform calibration grid of n circular fiducials along with their Cartesian target positions $\boldsymbol{Q_s}$ is established.
5. If the calibration is applied, and training data exist, the trained RBF network is employed to predict the scan field deviation. The predicted deviation is then used to compute the corrected target positions $\boldsymbol{K_s}$. Due to the low computational complexity of the RBF kernel, the corrections are performed directly on the industrial PC (IPC) controlling the GLS system. Integrating the RBF kernel on the IPC allows for a fully automatic in situ calibration, reducing calibration time and human error. See Section 2.8.
6. The joint and task space of the GLS system are mapped utilising a simplified geometrical model. The purpose is here to establish a relationship between the control input to the scanner $\boldsymbol{B}$ and Cartesian points in the workspace of the scanner. The simple model limits the need for prior knowledge of the optical design of the GLS system and can easily be adapted to significant changes in hardware configuration. See Section 2.3.
7. The fiducials are laser marked onto the calibration plate at a robotic pose based on the computed surface normal $\boldsymbol{V_s}$ and position $\boldsymbol{Y_s}$ of the calibration plate.
8. The marked calibration plate is scanned again, following the same scanning trajectory as in Step 3. See Section 2.1.
9. Image processing is used to locate the fiducial centres $\boldsymbol{P_c}$ in the coordinate system of the measurement scanner to determine their actual positions. See Section 2.4.
10. The actual positions of the marked fiducials are transformed to the coordinate system of the GLS system $\boldsymbol{P_s}$. Thus, a direct comparison can be made to their corresponding nominal target positions $\boldsymbol{Q_s}$. See Section 2.5.
11. The positional deviations δ between the nominal and target positions are determined, representing the required corrections to undistort the scan field. The maximum and root mean square (RMS) of the deviations δ are computed to indicate the scan field distortion. If the RMS of the deviation δ is above a predefined tolerance δ_{tol}, the calibration is run. Otherwise, the process is stopped. See Section 2.6.
12. If the calibration is performed, the positional deviations δ are used to train a low-complexity RBF network. The trained RBF network is then used to predict the required positional corrections to undistort the scan field. The purpose of using an RBF network is to offer a simple and generalised solution with low training times. See Section 2.7.

In the below sections, the primary elements of the proposed methodology are further elaborated.

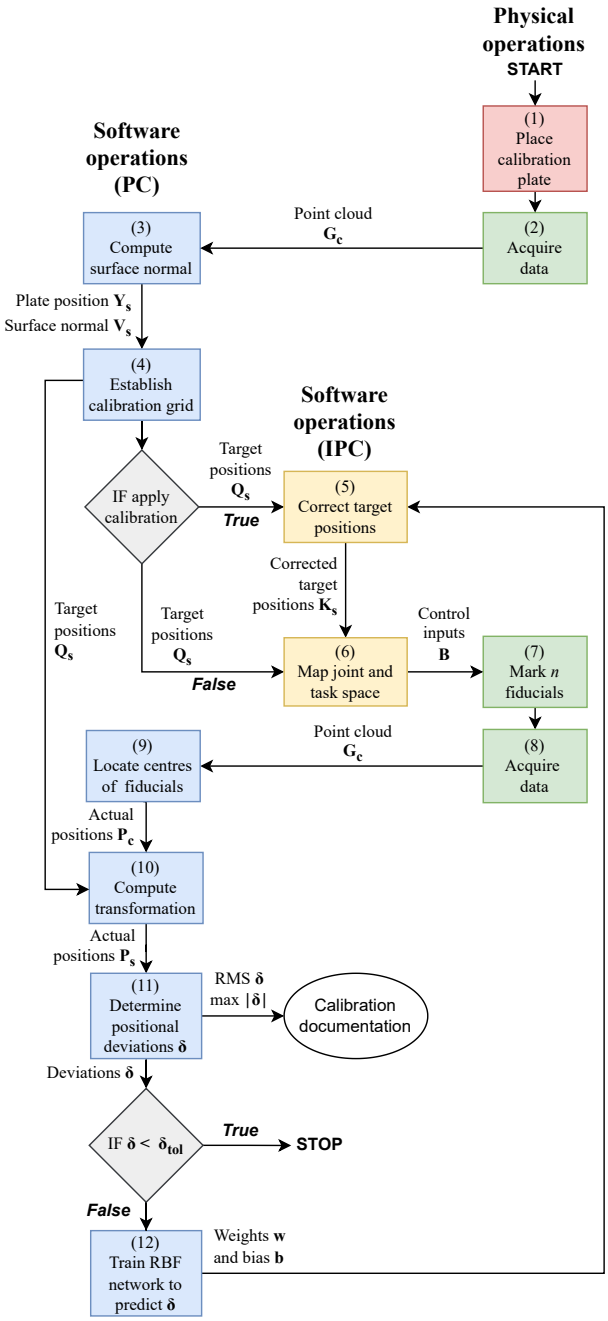

Figure 1. Flowchart providing an overview of the software and physical operations in the calibration methodology. The blue boxes indicate a software operation performed on the PC that handles the heavier computations. The yellow boxes indicate a software operation performed directly on the IPC controlling the GLS system. The red and green boxes represent manual and automatic physical operations.

2.1. Data Acquisition

Data-driven methods are known to be sensitive to the quality of the training data [7]. Thus, the data acquisition and data processing stages are essential. There are several approaches for acquiring accurate three-dimensional data, including non-contact and contact methods. As neutral networks commonly require large data sets, contact methods are considered out of scope for this paper. Non-contact-based methods rely on a range of different principles based on the application in which they are applied, i.e., stereo vision, structured light, and laser triangulation [16]. Laser line scanning based on laser triangulation is selected for its applicability in applications where rapid acquisition, high-density information, and accurate surface representation are required while maintaining a relatively low cost. Laser line scanning can further represent the reflectivity or colour of the scanned surface by measuring the amount of reflected backscatter.

As laser line scanning works by observing a projected laser profile, only 2D range data are acquired by the scanner. Therefore, the measurement scanner or object must be manipulated to achieve a full three-dimensional scan; hence, the accuracy and resolution of the acquired data depend on both the scanner and the manipulator. To achieve the highest possible robustness and accuracy of the acquired data, careful consideration of the environment, selection of scanning parameters, and planning of the scanning trajectory are necessary.

Laser speckle noise and spurious reflections are well-known challenges. A wide dynamic range of the backscattered light intensity [17,18] as well as the colour, intensity, and variation in ambient lighting can significantly affect the quality of the acquired data [19,20]. Scanning noise is especially problematic when scanning reflective surfaces such as sheet metal, presenting itself as false detections, over-saturated pixels, missing points, and a lack of accuracy.

The acquired data from the measurement scanner consists of a structured point cloud of $\boldsymbol{G_c} = [\boldsymbol{x_c}, \boldsymbol{y_c}, \boldsymbol{z_c}, \boldsymbol{i_c}]$ points, representing a 3D Cartesian point with an associated backscatter pixel intensity i_c in the coordinate system of the 3D scanner $O_c - X_c Y_c Z_c$. It should be noted that the transformation between the tool centre points (TCP) of the 3D scanner and the GLS system are determined based on CAD data to align their coordinate systems.

2.2. Computing Surface Normal and Position of Calibration Plate

Knowledge of the relative pose between the GLS system and calibration plate is essential, as any unknown deviations in the working distance or from orthogonality will result in calibration errors. The surface normal vector $\boldsymbol{V_s}$ of the calibration plate is determined by fitting a plane [21] to the acquired points representing the calibration plate. This permits computation of the rotation matrix $\boldsymbol{R}$ that rotates the normal vector $\boldsymbol{U_s} = [0, 0, 1]$, representing the Z-axis of the scanner coordinate system $O_s - X_s Y_s Z_s$ onto $\boldsymbol{V_s}$. $\boldsymbol{R}$, hence, aligns $\boldsymbol{V_s}$ with the Z-axis of the GLS system so that orthogonality can be ensured between the GLS system and the calibration plate upon marking the calibration fiducials. The working distance is corrected based on the position of the calibration plate $\boldsymbol{Y_s}$, defined as its centre. Following the above approach, it is ensured that the calibration plate and the focal plane of the GLS system are coincident and parallel during calibration.

The same method can be further used when processing materials with the system to ensure that the relative pose between the GLS system and the working plane corresponds to the calibration.

2.3. Mapping the Task and Joint Space

Generally, the galvanometers of GLS systems consist of a motor, a mirror mounted on the rotational axis of the motor, and an encoder. The proposed method assumes a post-objective system in which the ingoing laser beam initially passes through the dynamic focus module (DFM). Afterwards, the laser beam continues through the objective and is then reflected by the X-mirror and, lastly, the Y-mirror. A simplified pre-objective GLS system is illustrated in Figure 2. While the DFM and the X- and Y-mirrors are in their

respective zero positions, the outgoing beam hits the origin of the scanner's coordinate system $O_s - X_s Y_s Z_s$, placed at the centre of the workspace.

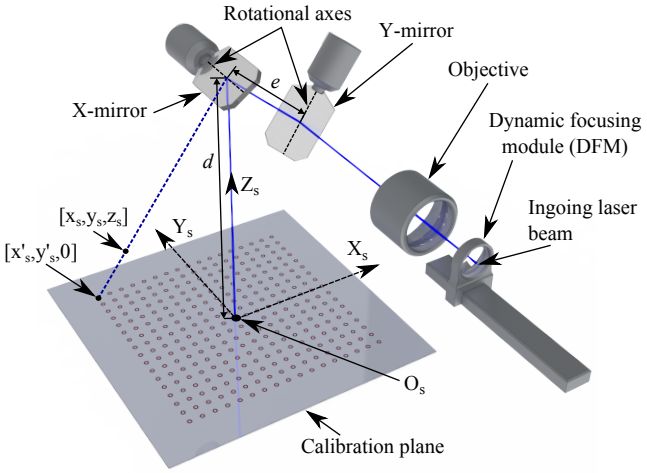

Figure 2. The optical chain of a pre-objective dual galvanometric system on which the geometrical model is based. The blue line indicates the path of the laser beam.

As a result, manipulation of the laser beam is performed in the joint space by controlling the angles of the galvanometers and the displacement of the DFM. Nonetheless, in most practical applications, processing is performed based on Cartesian points in the task space and, therefore, the joint and task space relationship must be mapped. To limit the necessary knowledge of the optical and mechanical design of the GLS system, the mapping between the task space and joint space is based on a simplified geometrical model adapted from [4]. Resulting from the use of a simplified model, the following general assumptions apply:

- The mirrors are placed perpendicular to each other.
- The ingoing and reflected laser beam hits the mirrors on their rotational axes.
- The diameter of the laser beam does not exceed the mirror dimensions.

The simplified model is widely applicable as the only parameters related to the optical and mechanical design of the GLS system are the distance between the rotational axes of the X- and Y-mirrors, given as e, and the perpendicular distance d from the X-mirror to the centre of the calibration plane.

The forward kinematic equations, employed to compute a Cartesian position in the task space from a position in the joint space, are given by Equations (1) and (2).

$$x_s = (d - z_s)\tan(\theta_x) \tag{1}$$

$$y_s = (e + \frac{(d - z_s)}{\cos(\theta_x)})\tan(\theta_y) \tag{2}$$

Based on Equations (1) and (2), the inverse kinematic equations are obtained. These are presented in Equations (3)–(5). The inverse kinematic equations are used to compute the required position in the joint space to reach a specified position in the task space.

$$\alpha_x = \frac{1}{2}\theta_x = \frac{1}{2}\arctan\left(\frac{x_s}{(d - z_s)}\right) \tag{3}$$

$$\alpha_y = \frac{1}{2}\theta_y = \frac{1}{2}\arctan\left(\frac{y_s}{e + \sqrt{(d - z_s)^2 + x_s^2}}\right) \tag{4}$$

$$\Delta f_r = \sqrt{\left(e + \sqrt{(d - z_s)^2 + x_s^2}\right)^2 + y_s^2} - (e + (d - z_s)) \tag{5}$$

where α_x, α_y, and Δf_r define the control inputs to the scanner, representing the mechanical angles of the X- and Y-mirrors and the displacement of the DFM in relation to its zero position. A set of control inputs $\boldsymbol{B} = [\alpha_x, \alpha_y, \Delta f_r]$, therefore, correspond to a nominal Cartesian position $\boldsymbol{Q_s} = [x_s, y_s, z_s]$ in the task space, and vice versa.

It is expected that the use of a simplified geometrical model will result in some scan field distortion, as the majority of GLS systems will invalidate the above assumptions due to mechanical misalignment, laser beam drift, thermal effects, optical path errors, mount offset errors, or other unknown factors [4].

Therefore, the proposed calibration methodology, presented in the following sections, aims to compensate for the scan field distortion. The general approach relies on correcting the nominal target positions $\boldsymbol{Q_s}$ based on the measured scan field distortion. The proposed methodology exploits that any given point $\boldsymbol{Q_s}$ in the workspace will have a corresponding point $\boldsymbol{Q'_s} = [x'_s, y'_s, 0]$ on the calibration plane, as illustrated in Figure 2. As such, correcting any point $\boldsymbol{Q'_s}$ on the focal plane will result in an adapted correction of the corresponding point $\boldsymbol{Q_s}$ in the workspace. This permits the calibration to be performed on the focal plane while allowing for the positional corrections to be effective, even when processing outside the calibration plane.

As a result, z_c is omitted in the following sections as all points lie on the calibration plane during calibration ($z_c = 0$), and hence $\boldsymbol{Q'_s} = \boldsymbol{Q_s}$.

2.4. Locating Fiducial Centres

Locating the centres of the marked circular fiducials in the acquired point cloud, illustrated in Figure 3, relies on several common image processing operations:

1. **The 3D → 2D projection:** The point cloud is projected to 2D, such that the calibration plate is represented as a two-dimensional image $\boldsymbol{I_c}$, i.e., $\mathbb{R}^3 \mapsto \mathbb{R}^2$. The projection is made based on the rotation matrix $\boldsymbol{R}$ (Section 2.2) and utilising the captured backscatter intensities $\boldsymbol{i_c}$ as the pixel intensity of the image $\boldsymbol{I_c}$. Subsequently, a median filter is employed to $\boldsymbol{I_c}$ to reduce noise. See Figure 4, left.
2. **Edge detection and morphology:** The Canny edge detection operator [22] is applied to highlight the marked circles. This operation is succeeded by morphological closing and filling operations to remove noise from the binary edge image resulting from the Canny operation; Figure 4, centre.
3. **Circle detection:** The Circular Hough Transformation (CHT) [23] is used to identify and locate circles in the processed image. See Figure 4, right. Additionally, this method offers sub-pixel accuracy, improving the detection accuracy of the circles.
4. **The 2D → 3D projection:** Lastly, the located centre coordinates are projected back into 3D to form the matrix $\boldsymbol{P_c} = [\boldsymbol{x_c}, \boldsymbol{y_c}]$ of actual positions in the $O_c - X_c Y_c Z_c$ coordinate system.

Locating all existing circles is beneficial to achieve the highest calibration accuracy. Excessive scratches or contamination can lead to noise, although these have been observed to be limited on plates of rolled steel directly from the supplier.

2.5. Computing the Transformation

To compare the measured actual positions $\boldsymbol{P_c}$ with the target positions $\boldsymbol{Q_s}$, the actual positions $\boldsymbol{P_c}$ must be accurately transformed to the $O_s - X_s Y_s Z_s$ coordinate system of the GLS system. A rigid Euclidean transformation is used for this purpose.

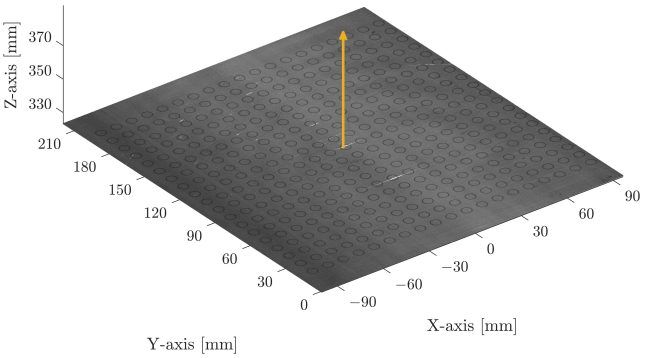

Figure 3. Acquired point cloud of n marked fiducials. The yellow arrow indicates the computed surface normal vector $\boldsymbol{V_s}$ of the calibration plate.

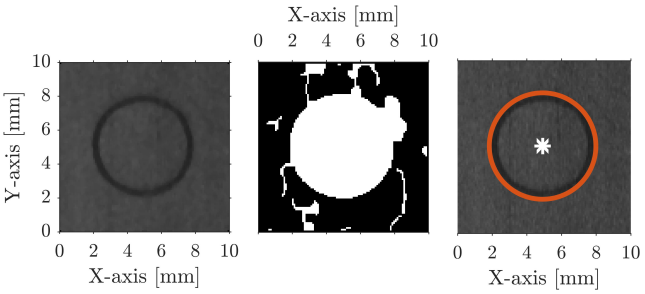

Figure 4. Cropped out circular fiducial of the projected point cloud, illustrating the image processing steps to locate the fiducials. A median filter is applied to the image (**left**), Canny edge detection and morphology (**centre**), and identification of circular patterns using CHT (**right**).

Due to the optical design of the system, the distortion is limited directly on the X-axis and Y-axis, i.e., when either of the mirrors is in its respective zero position, and the other is moving. Furthermore, the distortion increases with the distance to the centre of the workspace. These properties are exploited when computing the transformation. It is assumed that the scanned calibration plate has a maximum in-plane rotation of $\pm 15°$. An even number of points l are selected on each axis, ordered from smallest to largest, starting with their X-values and, secondly, their Y-values. This operation is performed for both the measured actual positions $\boldsymbol{P_c} = [\boldsymbol{x_c}, \boldsymbol{y_c}]$ and nominal target positions $\boldsymbol{Q_s} = [\boldsymbol{x_c}, \boldsymbol{y_c}]$. A set of paired points from each coordinate system is thereby created.

The paired points form the foundation to compute the Euclidean transformation, formulated as a least square optimisation problem to obtain the required rotation $\boldsymbol{R_c}$ and translation $\boldsymbol{T_c}$. The final rotation and translation are applied to $\boldsymbol{P_c} = [\boldsymbol{x_c}, \boldsymbol{y_c}]$, resulting in the actual positions $\boldsymbol{P_s} = [\boldsymbol{x_s}, \boldsymbol{y_s}]$ in $O_s - X_s Y_s Z_s$.

2.6. Determining Positional Deviations

By pairing the points of $\boldsymbol{P_s}$ with $\boldsymbol{Q_s}$ using the nearest neighbour approach, the positional deviations $\boldsymbol{\delta}$ can then be computed as the difference between the nominal target positions $\boldsymbol{Q_s} = [\boldsymbol{x_s}, \boldsymbol{y_s}]$ and the actual positions $\boldsymbol{P_s} = [\boldsymbol{x_s}, \boldsymbol{y_s}]$, Equation (6).

$$\boldsymbol{\delta} = \boldsymbol{Q_s} - \boldsymbol{P_s} \tag{6}$$

The measured positional deviations $\boldsymbol{\delta}$ can also serve as a means to detect drifts in the GLS system, e.g., due to wear or thermal distortions, indicating a need for calibrating or

maintenance. The maximum absolute deviation and the RMS of the deviation serve as means to evaluate the accuracy of the GLS system.

However, applying the positional deviations to calibrate the system by correcting the target positions and, thereby, compensating for the measured scan field distortion presents a problem: experimentally determining the positional deviations with a high density throughout the entire scan field is impractical and time-consuming. As a result, a neural network is used to predict the positional deviations at any point across the scan field.

2.7. The RBF Neural Network

The Radial Basis Function (RBF) network, initially introduced by [24], can be characterised as a feed-forward neural network consisting of three layers. The RBF network is illustrated in Figure 5. RBF networks have a vast number of applications, e.g., classification [25] and function approximation [26], and are known for their simplicity and ability to generalise while maintaining a low computational complexity [27,28]. Compared to other neural networks, such as the common Multi-Layer Perceptrons (MLP) network, the RBF network further excels in increased reliability, reduced extrapolation errors, and faster convergence [29].

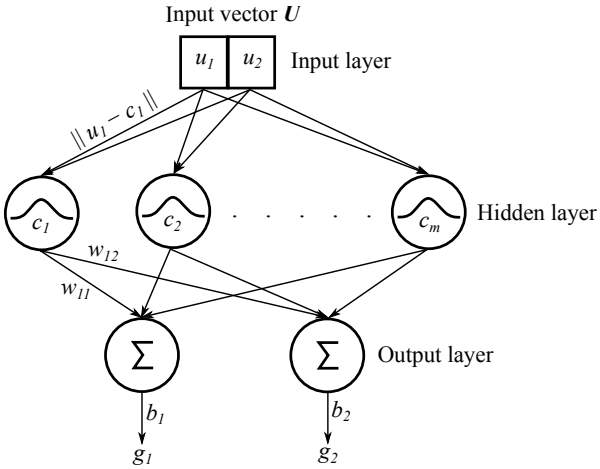

Figure 5. Structure of the applied RBF network.

The RBF network is specifically selected as its characteristics make it advantageous for a robust and efficient implementation directly on the IPC that controls the GLS system. The low computational complexity is beneficial for real-time implementation, while the mathematical simplicity of the network permits native integration on IPCs, commonly limited to basic mathematical operations. Integrating the network directly on the IPC forms the basis for a fully automated calibration.

The RBF network is constructed such that it takes an input vector $\boldsymbol{U} = [u_1, u_2]$, here equal to a nominal position $\boldsymbol{Q_s} = [x_s, y_s]$. The output of the network $\boldsymbol{G} = [g_1, g_2]$ will then be equal to $\hat{\boldsymbol{\delta}} = [\hat{\delta}_x, \hat{\delta}_y]$, which is the predicted positional deviation along the *X*- and *Y*-axis in the given position.

$$\phi_j(\|U - c_j\|) = \exp\left(-\frac{\|U - c_j\|^2}{2\sigma_j^2}\right) \tag{7}$$

$$g_k = \sum_{j=1}^{m} w_{jk}\phi_j(U) + b_k \tag{8}$$

The working principle of the RBF network can be summarised as follows:

1. **Input layer:** The input vector $\boldsymbol{U}$ is fed into the network and connects the input vector to all neurons of the hidden layer.
2. **Hidden layer:** Consists of $j = 1 \dots m$ RBF Gaussian activation functions (neurons). The similarity between the input and the stored Gaussian centre c is calculated based on the Euclidean norm, such that the response from the activation function increases or decreases with the distance to the centre c. The activation function is given by Equation (7), where $\|U - c_i\|$ is the Euclidean norm, while σ defines the spread of the Gaussian functions.
3. **Output layer:** Consists of $k = 1 \dots 2$ output nodes, where each nodes outputs a linear combination of the weighted w responses from activation functions in the form of Equation (8). A bias term b is further added to each output to remove bias from the output.

As RBF networks are universal approximates, they can theoretically approximate any continuous function with arbitrary precision, assuming an appropriate selection of activation function and parameters [29]. The parameters and corresponding centres, weights, and biases are selected during the network training.

Training the RBF Network

The RBF network is trained using the orthogonal least-squared (OLS) method [30], following the forward centre selection approach. The OLS method was chosen due to its simplicity, speed, and deterministic behaviour, making it suitable for future integration directly on the IPC that controls the GLS system. Other approaches to determine the centres include unsupervised learning methods, such as K-means [29], which are more efficient for large and complex data sets.

By utilising the OLS method, the network is thereby iteratively constructed by selecting and adding Gaussian centres c from the input vector with corresponding weights w and bias b, such that the mean square error (MSE) is minimised. The network is trained using the nominal target positions $\boldsymbol{Q_{s,i}} = [x_{s,i}, y_{s,i}]$, $i = 1 \dots n$, as the input to the network along with the corresponding measured positional deviations $\boldsymbol{\delta_i} = [\delta_{x,i}, \delta_{y,i}]$ as the targets. The process is stopped when the algorithm has processed all data points or hit the specified MSE goal. As a result of the OLS method, the number of neurons n, centres c, weights w, and bias b are automatically selected. Hence, only the spread σ of the Gaussian functions and the MSE goal must be manually defined.

A small spread σ allows the network to capture local features in the data but limits its capabilities in identifying the underlying pattern. Hence, it results in poor generalisation of unseen data. Inversely, a large spread entails a close fit of the training data, allowing the network to capture global features of the data. However, overgeneralising reduces the network's ability to identify and predict local patterns, leading to poor performance on unseen data. As such, the spread of the Gaussian functions can be used to obtain a balance between fitting the data closely and overfitting the network.

The effects of the MSE goal are similar to that of the spread. By using a stringent MSE goal, such as zero, the network learns to make predictions as close to the target values as possible. This increases the risk of overfitting the network, leading to poor generalisation abilities as the network cannot capture the underlying pattern of the training data. On the contrary, a relaxed MSE goal improves the generalisation abilities but may lead to underfitting the network. This results in poor accuracy as the network's predictions may be far from the target values.

The selection of the hyper-parameters, here the MSE goal and spread of the Gaussian functions, is made using a grid-based search followed by a trial-and-error fine-tuning of the parameters. This approach allows for testing a wide range of parameter combinations, such that an optimal balance between the network's generalisation performance and prediction accuracy is achieved. This enables the network to accurately predict the positional deviations across the scan field, both in and away from the training points.

An overfitted network can react highly unpredictably on unseen data, constituting a safety concern, especially when dealing with high-power laser processing. Therefore, an underfitted network is preferred to improve generalisation performance and robustness in the case of noisy data points, though at the expense of prediction accuracy.

The performance of the network during and after training is evaluated using a five-fold cross-validation approach. The selected approach permits approximation of the generalisation performance and prediction accuracy of the network without the use of new data, which in turn minimises the risk of overfitting the network [31]. However, as with any neural network, the output of the network depends on the accuracy and quality of the training data. As such, inaccurate training data will result in an inaccurate network. The uncertainty related to the applied measurement method, and hence the training data, is discussed and presented in Section 3.2.

2.8. Correcting the Target Positions

The trained centres, weights, and biases are fed into the RBF network, which is implemented on the IPC, controlling the GLS system. The RBF network then predicts and applies the required positional corrections to the nominal target positions $\boldsymbol{Q_s}$. The result is the corrected target positions $\boldsymbol{K_s} = [\boldsymbol{x_k}, \boldsymbol{y_k}]$, given by Equation (9), that compensate for the measured scan field distortion.

$$\boldsymbol{K_s} = \boldsymbol{Q_s} + \hat{\boldsymbol{\delta}} \tag{9}$$

The corrected target positions are, subsequently, used to correct the control input to the scanner $\boldsymbol{B} = (\theta_x, \theta_y, \Delta f_r)$ based on the inverse kinematic equations, given by Equations (3)–(5) in Section 2.3.

3. Experimental Validation

The proposed method is validated based on an industrial laser processing setup, illustrated in Figure 6, along with the associated coordinate systems. The main component of the system is a customised ARGES Fibre Elephant 50 commercial GLS system that consists of dual galvanometric mirrors ($\pm 10.5°$) and a dynamic focus module (DFM). The DFM can adjust the focal length of 490 mm $\pm$25 mm, providing a focal plane of 300 $\times$ 300 mm^2 that can be transversed at a maximum velocity of 1500 mm/s. A 3kW IPG YLS-3000 single-mode laser delivers the laser beam with a beam quality of 1.2 M^2. The GLS system is controlled by a Beckhoff C6920-0060 IPC and mounted onto a KUKA KR 120 R2700 6-axis industrial manipulator. The relationship between the GLS system and the robot is calibrated using the accompanying cutting nozzle. The cutting nozzle is designed such that the tip of the nozzle is located at the focal point of the GLS system, permitting the use of the XYZ 4-point calibration method integrated with the robot controller. A calibration uncertainty of 0.366 mm was achieved for the robot.

The combination of hardware leads to a flexible setup with a significantly expanded workspace of the GLS system, adding additional degrees of freedom and thus permitting the processing of large-scale 3D-dimensional parts. The measurement data are acquired by a Wenglor MLWL 153 2D laser line scanner working at 405 nm. The measurement scanner is mounted in parallel with the GLS system, such that the Z_s-axis of the GLS system and the Z_c-axis of the measurement scanner are parallel. The measurement scanner offers a measuring range in Z_c from 215 to 475 mm, resulting in a Z_c-resolution of 0.0096–0.0220 mm. The equivalent X_c-range is 150–230 mm in X_c with a resolution between 0.079 and 0.120 mm, depending on the distance to the measured object. The linearity deviation of the line scanner is 65 µm.

The validation is performed by following the method illustrated in the flowchart, Figure 1, from Steps 1 to 12, and by substituting the target positions $\boldsymbol{Q_s}$ with the corrected target positions $\boldsymbol{K_s}$ in Step 6. Further details are presented in the below sections.

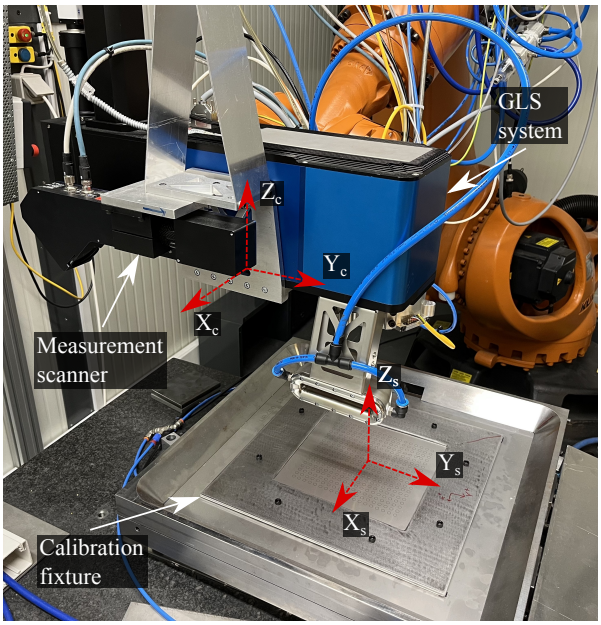

Figure 6. The system configuration and associated coordinate systems.

3.1. Laser Marking of Fiducials

The training data and subsequent validation for the RBF network are based on a single uniform grid marked onto a standard 1.5 mm thick AISI 316 stainless steel plate without visible surface defects. The marked steel plate thereby acts as a calibration plate. The calibration plate is clamped between two 2 mm steel plates to minimise the distortion. The upper clamping plate has a 220×220 mm^2 cutout to expose the calibration plate. Figure 6 illustrates the fixture and calibration plate.

The marked grid consists of $n = 361$ uniformly spaced fiducials, each composed of two concentric circles with radii $r_1 = 2.5$ mm and $r_2 = 2.7$ mm, distributed over a calibration plane of 190×190 mm^2. The fiducials are marked at a scanning velocity of 200 mm/s with 40 W laser power, orthogonal to the calibration plate. This equates to a processing time of 89 s. The calibration plane is purposely reduced compared to the theoretical maximum focal plane to allow for localised focal adjustments in future applications (± 5 mm).

3.2. Data Acquisition and Measurement Uncertainty

The data acquisition is executed at a linear robotic trajectory with a constant orientation and velocity of 15 mm/s. To further maximise the data quality, scans are performed at a minimal allowable working distance of roughly 325 mm, orthogonal to the scanned object, and in the absence of ambient light. The data acquisition results in a structured and uniform point cloud with X- and Y-resolution of 0.1 mm. The scanning trajectory is nominally identical in both the calibration and subsequent validation phases to minimise errors in the 3D scans by reducing deviations in the absolute positioning of the robot.

The scan field deviation measurements in the pre-calibration state are repeated five times, using identical parameters and scanning trajectories. The purpose is to validate the repeatability of the measurements. The mean RMS of the deviation $\|\delta\|$ (pre-calibration) across the five measurements is evaluated to 0.0819 mm with a standard deviation of 0.0028 mm, thus indicating acceptable repeatability and robustness.

The measurement accuracy and uncertainty are evaluated based on a certified GOM CP 20/MV 175×140 mm^2 ceramic calibration plate, placed at various positions to cover the full measurement area. The calibration plate consists of 23×19 circles of $r = 2.3$ distributed

over a uniform pattern. By applying Steps 7–11 of Figure 1, the positional deviations between the nominal and measured positions of the GOM plate fiducials can be evaluated. The resulting positional deviation represents the measurement accuracy and uncertainty of the proposed method and setup. The systematic error and associated standard uncertainty (coverage factor $k = 1$) in the X- and Y-direction is computed to 0.000 ± 0.0914 mm and 0.000 ± 0.0862 mm. Note that the evaluated uncertainty is roughly equivalent to the pixel size of 0.1×0.1 mm^2.

The evaluated accuracy suggests insignificant bias in the measurements, likely due to the transformation in Step 10, Figure 1. The standard uncertainty of 0.0862 mm is expected, as the data acquisition is performed at a considerable distance from the surface, at ≈325 mm, and using a large industrial manipulator. However, the low standard uncertainty and the insignificant bias in the measurements also indicate that the robot trajectory is accurate and moves in a straight trajectory as intended. As 3D optical scanning is still a relatively new technology, it is affected by several potential error sources. These include resolution and scanning orientation, which complicate the evaluation of the measurement uncertainty [32].

3.3. Training the RBF Network

For training the RBF network, the MSE goal is set to 0.0005 while the spread is $\sigma = 35$. The selected parameters are observed to provide a suitable balance between prediction accuracy and generalisation performance. The result is a network of $m = 67$ neurons in the hidden layer. The achieved mean RMS prediction error of the five cross-validation rounds is 0.047 mm with a 0.0021 mm standard deviation. Hence, a calibration accuracy below the achieved RMSE of the trained network should not be expected. The low standard deviation across the validation rounds suggests appropriate stability in the chosen hyper-parameters, while the low RMSE suggests a satisfactory modelling fit. An expanded training data set could improve the prediction accuracy, however, at the expense of an overall increased calibration time, i.e., computational and experimental.

After cross-validation, the network is trained on the complete data set of $n = 361$ points with a mean training time of 5.88 s. A single iteration of the RBF network has a mean computation time of 0.000055 s over 1000 iterations, making the RBF network suitable for real-time implementation. The computational time for the complete calibration, including data and image processing and network training, is ≈ 62 s.

All computational times are measured in MATLAB 2020b with an Intel Core i7 (i7-9750H) CPU @ 2.6 GHz.

4. Results and Discussion

The developed method was experimentally shown on the setup presented in Section 3, following the methodology shown in Figure 1. Figure 7a illustrates the scan field deviation in the pre-calibration state. It can be observed that the deviation is non-uniform and smallest at the centre of the workspace as it increases towards the edges of the scan field. This is expected and likely due to thermal effects or assembly defects, e.g., related to the mirrors and axes or the laser source, which are commonly identified as the most significant contributors to laser beam drift [4,5]. Moreover, the deviation along the Y-axis is lower than the X-axis. This can further be observed from the plotted positional deviation distribution, Figure 8. As can be seen from Table 1 and observed in the upper right corner of Figure 7a, the maximum Euclidean deviation $\|\delta\|$ across the entire scan field is 2.08 mm, while the RMS of the deviation is 0.85 mm. The significant deviation is expected as the simplified geometrical model does not consider any mechanical misalignment, laser beam drift, thermal effects, optical path errors, and mount offset errors, resulting in the observed non-linear scan field distortion [4]. For any practical application, the significant deviation is unacceptable and suggests that the utilised simplified model is, standalone, unsuited for calibrating the GLS system at hand.

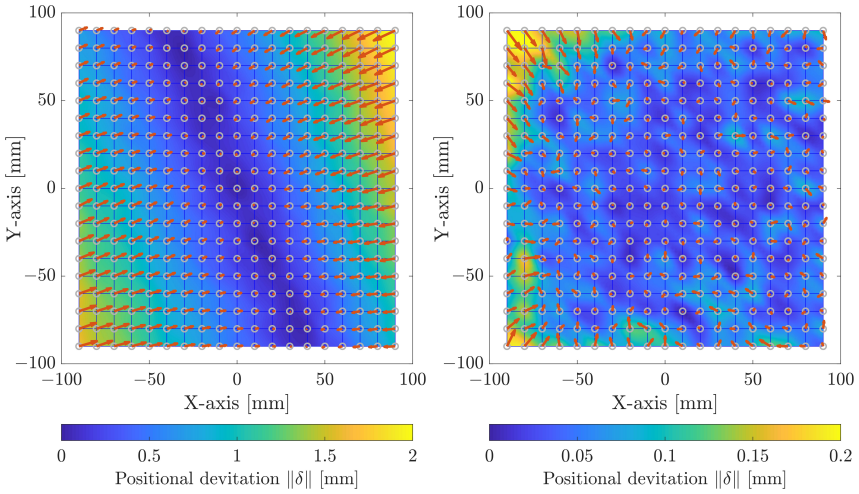

(**a**) Pre-calibration positional deviations (**b**) Post-calibration positional deviations

Figure 7. Pre- and post-calibration positional deviations δ, respectively (**a**,**b**). The grey circles indicate the target positions $\boldsymbol{P_c}$, while the direction and scale of the red arrows indicate the direction and scale of the positional deviation. Note that the scaling of the colour bar is a factor of 10 smaller in (**b**) compared to (**a**).

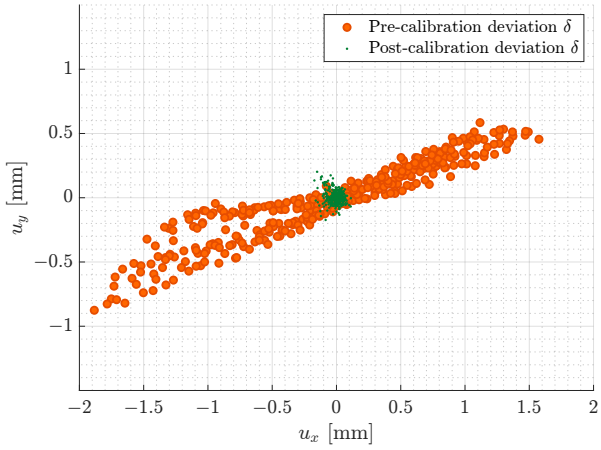

Figure 8. Comparison of positional deviations pre- and post-calibration.

Calibrating the GLS system using the proposed method has significantly reduced the calibration error. This can be observed by both the post-calibration scan field distortion of Figure 7b and the positional deviation distribution, Figure 8. As presented in Table 1 and observed at the outer edge of the calibration plane, the maximum positional deviation is reduced by 87.8% to 0.25 mm, while the RMS of the deviation has shown a 91.7% reduction to 0.071 mm. From Figure 7b, a relatively homogeneous scan field distortion is observed, indicating that both the data acquisition and processing along with the RBF network generally are robust.

Table 1. Pre- and post-calibration results in various working areas.

	Max. $[u_x, u_y, \|\delta\|]$	**RMS** $[u_x, u_y, \|\delta\|]$
Pre-calibration (190 × 190 mm^2) (mm)	[1.884, 0.876, 2.077]	[0.800, 0.301, 0.854]
Post-calibration (190 × 190 mm^2) (mm)	[0.171, 0.202, 0.252]	[0.048, 0.051, 0.071]
Post-calibration (150 × 150 mm^2) (mm)	[0.099, 0.099, 0.135]	[0.034, 0.034, 0.047]
Post-calibration (50 × 50 mm^2) (mm)	[0.064, 0.058, 0.064]	[0.026, 0.023, 0.035]

However, the upper left and lower right corners do show outlying increases in the deviation, which likely stem from a measurement error. Because of the 0.1 mm resolution of the 3D scanner, a single-pixel shift in either direction, e.g., due to a digitisation error in the measurement scanner, a spurious reflection, or other external influences, leads to a 0.1 mm measurement error. A 3D scanner with an improved resolution could reduce the risk of measurement errors.

Calibration errors at the edges are typical; therefore, the common practice is to minimise the usable work area compared to the theoretical working area [5]. The cumulative histogram, Figure 9, of the Euclidean deviations $\|\delta\|$ across the scan field illustrates that 80% of the deviations are below 0.08 mm. As can also be seen in Table 1, reducing the scan field by 15 mm around the border to 150 × 150 mm^2 almost halves the maximum deviation δ to 0.135 mm.

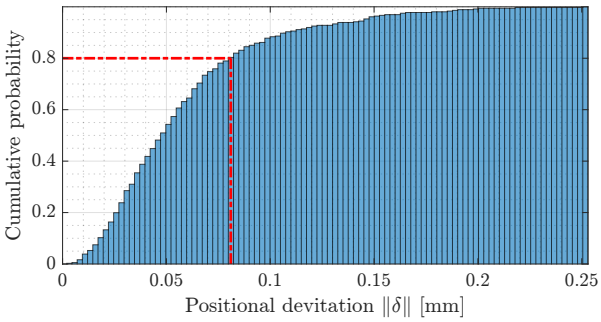

Figure 9. Cumulative histogram of the positional deviations δ post-calibration. As illustrated by the red line, note that 80% of the positional deviations are below 0.08 mm. The remaining 20% of the positional deviations are located at the border of the calibration area.

The above results confirm that the proposed method can significantly reduce the deviations and, hence, the scan field distortion. It should be noted that the calibration is performed in situ using the same hardware and materials as when the overall laser system is used for processing. Therefore, the achieved calibration accuracy is not based on specific calibration conditions and reflects the actual processing accuracy of the GLS system. Calibration methods performed in a strictly controlled environment under particular conditions, e.g., in a laboratory setup, will naturally achieve a higher calibration accuracy.

As stated in Section 1, several authors have proposed calibration approaches for GLS systems for materials processing, e.g., additive manufacturing, offering some similarities in both the application and the optical design. However, a direct quantitative comparison of the calibration accuracy to existing methods is challenging as both the hardware and optical design significantly affect the performance of the GLS systems [33], including the workspace size and positioning accuracy and repeatability. The default calibration method proposed by the manufacturer of the utilised GLS system involves laser marking a specific geometrical pattern. Subsequently, the marked pattern is manually measured using a Vernier calliper and input into the associated calibration software to correct the scan field distortion. Further details are unknown. However, the specific GLS system utilised in this paper is a customised version and, therefore, incompatible with the manufacturer's

calibration software. As a result, bench-marking the calibration accuracy with the default calibration method is not possible.

Based on the proposed methodology and results, the superiority of the proposed method compared to the existing methods can be summarised as the following:

- Using the proposed methodology, it is possible to perform the calibration in situ in an industrial robotised setup with limited knowledge of the optical design of the system.
- The achievable calibration accuracy is not dependent on certain controlled conditions as there are no strict requirements related to the placement of the calibration plate and the technical knowledge of the operator. This indicates that the achieved accuracy reflects the actual in-process accuracy of the calibrated GLS system.
- The results show that a GLS system can be calibrated without relying on specialised calibration tools or complex physical models and computationally heavy optimisation approaches.
- The proposed methodology allows for the automated calibration and validation to be conducted in less than 10 min without relying on any time-consuming and unreliable manual measurement methods.

4.1. Limitations and Sources of Error

4.1.1. Significant Pre-Calibration Deviation

Due to the use of a simplified geometrical model, the actual correction will deviate slightly from its target correction. Thus, the measured deviation will not be fully corrected. This limits the achievable calibration accuracy in the areas of the most considerable distortion. Performing a second iteration of the calibration could solve this issue.

4.1.2. Thermal Distortion

Measurement errors can occur due to thermal distortion, which directly influences the calibration accuracy. As the amount of heat induced into the surface during the laser marking process is limited, the effects are also limited. However, the probability of thermal distortion is highest at the edges of the calibration plate. Adding active cooling to the marking process could reduce the risk of errors resulting from thermal distortion.

4.1.3. Absolute Positional Errors

As the distance to the calibration plate is measured, deviations in the working distance and orientation due to the misplacement of the calibration plate are minimised. However, errors in the robot's absolute positioning and repeatability along the *Z*-axis of the robot cannot be observed and can significantly influence the calibration accuracy due to the Abbe offset. In terms of repeatability, it should be noted that the ISO9283 repeatability of the utilised robot is within ± 0.05 mm. One suggested approach is to measure the radius of the marked fiducials. Though, it is challenging to distinguish if any variation is due to a calibration error, a positioning error of the robot, or simply noise.

4.1.4. Euclidean Transformation

As the Euclidean transformation aligns the measured actual positions with the nominal target positions, any rotational errors around the *Z*-axis and the zero error of the GLS system cannot be measured. On the contrary, the influence of the robot's repeatability in the XY-plane is minimised in both the marking and measurement phases.

5. Conclusions

This paper presents a generalised and flexible method for the in situ calibration of GLS systems applied for robotic laser processing. The main contribution of the proposed method is a generalised, fast, and flexible in situ methodology that requires no specialised tools, limited user experience, or prior knowledge related both to the placement of the calibration plate, the relative pose of the GLS system, and its optical design. The presented method applies 3D scanning combined with image processing techniques to measure the

scan field distortion of the GLS system. This information is used to train an RBF neural network to predict the necessary corrections to compensate for the measured distortion. The proposed method shows promising results, with a reduction in the maximum and Euclidean scan field deviation of, respectively, 87.8% and 91.7% to 0.25 mm and 0.14 mm in the full and reduced calibration plane (150×150 mm^2). The achieved calibration accuracy results from a compromise on the calibration accuracy to achieve a generalised, flexible, and practical solution suitable for automation and industrial integration but reflects the actual in-process accuracy.

In future works, increasing the number of measurement points could improve the robustness and generalisation performance of the RBF network, leading to more accurate predictions. Moreover, performing a second calibration iteration could potentially improve the calibration accuracy of the RBF network, as the required positional corrections will be reduced.

Author Contributions: Conceptualization, A.F.M. and G.N.N.; methodology, A.F.M.; software, A.F.M. and G.N.N.; validation, A.F.M.; formal analysis, A.F.M.; investigation, A.F.M.; data curation, A.F.M.; writing—original draft, A.F.M.; writing—reviewing and editing, A.F.M., G.N.N. and M.K.; supervision, M.K.; project administration, M.K.; funding acquisition, M.K. All authors have read and agreed to the published version of the manuscript.

Funding: This work was supported by the Innovation Fund Denmark, project INTERLASE, grant number 7050-00024B, and by The Poul Due Jensen Foundation, project Laser Forming, grant number 2020-006.

Institutional Review Board Statement: Not applicable.

Informed Consent Statement: Not applicable.

Data Availability Statement: Data will be made available on request.

Acknowledgments: The authors would like to thank Anders Noel Thomsen for the rewarding discussions and comments in both the development of the proposed method and the writing process. Moreover, the authors would like to acknowledge Raphael Peter Hodgkinson for providing valuable assistance with the English editing.

Conflicts of Interest: The authors declare that they have no known competing financial interests or personal relationships that could have appeared to influence the work reported in this paper.

References

1. Gong, P.; Yang, J.; Ma, C.; Sun, Y.; Yu, Y.; Hou, Y. Research on multi-point monitoring anti-collision system for vehicle auxiliary driving. *Optik* **2016**, *127*, 7121–7127. [CrossRef]
2. Biscevic, A.; Bohac, M.; Pjano, M.A.; Grisevic, S.; Patel, S.; Pidro, A. Treatment of high astigmatism with wavelight allegretto eye-Q excimer laser platform. *Acta Inform. Medica* **2019**, *27*, 177–180. [CrossRef] [PubMed]
3. Hua, J.G.; Tian, Z.N.; Xu, S.J.; Lundgaard, S.; Juodkazis, S. Fast fabrication of optical vortex generators by femtosecond laser ablation. *Appl. Surf. Sci.* **2019**, *475*, 660–665. [CrossRef]
4. Xie, J.; Huang, S.; Duan, Z.; Shi, Y.; Wen, S. Correction of the image distortion for laser galvanometric scanning system. *Opt. Laser Technol.* **2005**, *37*, 305–311. [CrossRef]
5. Godineau, K.; Lavernhe, S.; Tournier, C. Calibration of galvanometric scan heads for additive manufacturing with machine assembly defects consideration. *Addit. Manuf.* **2019**, *26*, 250–257. [CrossRef]
6. Zhong, Q.; Tian, X.Y.; Huang, X.K.; Tong, Z.Q.; Cao, Y.; Li, D.C. High-accuracy calibration for multi-laser powder bed fusion via in situ detection and parameter identification. *Adv. Manuf.* **2022**, *10*, 556–570. [CrossRef]
7. Tu, J.; Zhang, L. Rapid on-site recalibration for binocular vision galvanometric laser scanning system. *Opt. Express* **2018**, *26*, 32608. [CrossRef]
8. Ortega Delgado, M.A.; Lasagni, A.F. Reducing field distortion for galvanometer scanning system using a vision system. *Opt. Lasers Eng.* **2016**, *86*, 106–114. [CrossRef]
9. Chen, M.F.; Chen, Y.P. Compensating technique of field-distorting error for the CO_2 laser galvanometric scanning drilling machines. *Int. J. Mach. Tools Manuf.* **2007**, *47*, 1114–1124. [CrossRef]
10. Tu, J.; Zhang, L. Effective data-driven calibration for a galvanometric laser scanning system using binocular stereo vision. *Sensors* **2018**, *18*, 197. [CrossRef]

11. Manakov, A.; Seidel, H.P.; Ihrke, I. A mathematical model and calibration procedure for galvanometric laser scanning systems. In Proceedings of the VMV 2011—Vision, Modeling and Visualization Workshop, Berlin, Germany, 4–6 October 2011; pp. 207–214. [CrossRef]
12. Le, V.T.; Quinsat, Y. In situ calibration of galvanometric scanning head for laser powder bed fusion machines based on a vision system. *Int. J. Adv. Manuf. Technol.* **2020**, *111*, 1767–1783. [CrossRef]
13. Wissel, T.; Wagner, B.; Stüber, P.; Schweikard, A.; Ernst, F. Data-driven learning for calibrating galvanometric laser scanners. *IEEE Sensors J.* **2015**, *15*, 5709–5717. [CrossRef]
14. Cui, S.; Zhu, X.; Wang, W.; Xie, Y. Calibration of a laser galvanometric scanning system by adapting a camera model. *Appl. Opt.* **2009**, *48*, 2632–2637. [CrossRef]
15. Smith, L.N.; Smith, M.L. Automatic machine vision calibration using statistical and neural network methods. *Image Vis. Comput.* **2005**, *23*, 887–899. [CrossRef]
16. Pérez, L.; Rodríguez, Í.; Rodríguez, N.; Usamentiaga, R.; García, D.F. Robot guidance using machine vision techniques in industrial environments: A comparative review. *Sensors* **2016**, *16*, 335. [CrossRef] [PubMed]
17. Gerbino, S.; Del Giudice, D.M.; Staiano, G.; Lanzotti, A.; Martorelli, M. On the influence of scanning factors on the laser scanner-based 3D inspection process. *Int. J. Adv. Manuf. Technol.* **2016**, *84*, 1787–1799. [CrossRef]
18. Amir, Y.M.; Thörnberg, B. High Precision Laser Scanning of Metallic Surfaces. *Int. J. Opt.* **2017**, *2017*, 1–13. [CrossRef]
19. Blanco, D.; Fernández, P.; Cuesta, E.; Mateos, S.; Beltrán, N. Influence of surface material on the quality of laser triangulation digitized point clouds for reverse engineering tasks. In Proceedings of the 2009 IEEE Conference on Emerging Technologies & Factory Automation, Palma de Mallorca, Spain, 22–25 September 2009. [CrossRef]
20. Mian, S.H.; Mannan, M.A.; Al-Ahmari, A.M. The influence of surface topology on the quality of the point cloud data acquired with laser line scanning probe. *Sens. Rev.* **2014**, *34*, 255–265. [CrossRef]
21. Torr, P.H.; Zisserman, A. MLESAC: A new robust estimator with application to estimating image geometry. *Comput. Vis. Image Underst.* **2000**, *78*, 138–156. [CrossRef]
22. Canny, J. A Computational Approach to Edge Detection. *IEEE Trans. Pattern Anal. Mach. Intell.* **1986**, *PAMI-8*, 679–698. [CrossRef]
23. Atherton, T.J.; Kerbyson, D.J. Size invariant circle detection. *Image Vis. Comput.* **1999**, *17*, 795–803. [CrossRef]
24. Broomhead, D.S.; Lowe, D. Multivariable Functional Interpolation and Adaptive Networks. *Complex Syst.* **1988**, *2*, 321–355.
25. Lutz, B.; Kisskalt, D.; Mayr, A.; Regulin, D.; Pantano, M.; Franke, J. In-situ identification of material batches using machine learning for machining operations. *J. Intell. Manuf.* **2021**, *32*, 1485–1495. [CrossRef]
26. Bustillo, A.; Pimenov, D.Y.; Mia, M.; Kapłonek, W. Machine-learning for automatic prediction of flatness deviation considering the wear of the face mill teeth. *J. Intell. Manuf.* **2021**, *32*, 895–912. [CrossRef]
27. Moradkhani, H.; Hsu, K.L.; Gupta, H.V.; Sorooshian, S. Improved streamflow forecasting using self-organizing radial basis function artificial neural networks. *J. Hydrol.* **2004**, *295*, 246–262. [CrossRef]
28. Aljarah, I.; Faris, H.; Mirjalili, S.; Al-Madi, N. Training radial basis function networks using biogeography-based optimizer. *Neural Comput. Appl.* **2018**, *29*, 529–553. [CrossRef]
29. Wu, Y.; Wang, H.; Zhang, B.; Du, K.L. Using Radial Basis Function Networks for Function Approximation and Classification. *ISRN Appl. Math.* **2012**, *2012*, 1–34. [CrossRef]
30. Chen, S.; Cowan, C.; Grant, P. Orthogonal least squares learning algorithm for radial basis function networks. *IEEE Trans. Neural Netw.* **1991**, *2*, 302–309. [CrossRef]
31. James, G.; Witten, D.; Hastie, T.; Tibshirani, R. An introduction to statistical learning: With applications in R. In *Springer Texts in Statistics*; Springer: New York, NY, USA, 2013; Volume 103.
32. Kortaberria, G.; Mutilba, U.; Gomez, S.; Ahmed, B. Three-Dimensional Point Cloud Task-Specific Uncertainty Assessment based on ISO 15530-3 and ISO 15530-4 Technical Specifications and Model-Based Definition Strategy. *Metrology* **2022**, *2*, 394–413. [CrossRef]
33. Cuccolini, G.; Orazi, L.; Fortunato, A. 5 Axes computer aided laser milling. *Opt. Lasers Eng.* **2013**, *51*, 749–760. [CrossRef]

Paper C

A Novel Method for Approximating Local Changes in the Surface Absorption for Laser Marking Using 3D Laser Scanning

Anders Faarbæk Mikkelstrup, Anders Noel Thomsen, and Morten Kristiansen

The paper has been published in the
IOP Conference Series: Materials Science and Engineering, vol. 1135, no. 012002, pp. 1-11, 2021.

A novel method for approximating local changes in the surface absorption for laser marking using 3D laser scanning

Anders F. Mikkelstrup[1], Anders N. Thomsen[1], Morten Kristiansen[1]

[1]Department of Materials and Production, Aalborg University, Fibigerstraede 16, 9220 Aalborg East, Denmark

afm@mp.aau.dk

Abstract. Laser marking is a non-contact technique, which achieves colouring by using a laser beam to increase surface oxidation. Controlling the amount of heat induced into the part is essential in ensuring the desired degree of oxidisation. However, the induced heat is not only dependent on the process parameters, but also on the surface absorption, which in turn is dependent on the material, laser wavelength, and surface quality, i.e., current degree of oxidation and contaminants as well as surface roughness. This paper proposes a method for correlating backscatter from a 3D laser scanner with the surface absorption of sheet metal parts. The purpose is to determine local changes in the surface absorption caused by surface oxidation and contamination. The method utilises a 3D laser scanner, which projects a laser line at the surface and measures the resulting backscatter at an angle. The proposed solution applies a bi-directional reflectance model to reduce the influence of varying scanning angles. The method's sensitivity to variations in surface treatments is investigated and validated against backscatter spectroscopy measurements. The results show that the proposed method can identify changes in the absorption. However, these were, in some cases, more than 70% higher compared to spectroscopy measurements.

1. Introduction

Laser marking is a method for increasing the thickness of the oxide layer by increasing the temperature. By changing the thickness, light is refracted differently, which gives colour changes. This can be used for aesthetic and communicative purposes in parts of metal. Controlling the colouring is a matter of process settings [1] and surface properties. The surface absorption describes the energy coupling efficiency of the surface. It thus is defined as the ratio between the incident energy from the laser and the absorbed energy by the surface [2]. As laser marking is dependent on controlling the induced heat into the material, knowledge of the absorption plays an essential role in the process stability and quality. It is well known that surface absorption is influenced by contamination, oxidation and roughness. Typically, surface contamination of sheet metal components originates from fingerprints and oil residue from manufacturing. Oxidation arises from oxygen reacting with the surface and will for stainless steel present itself as a thin layer of chromium oxide. The oxidation process will naturally occur over time but can be expedited by inducing heat, which is the principle behind laser marking. Abedi and

Hoseinpour [3] found that by coating the surface of an AISI 304L sample with an oxide layer, the surface absorption of wavelengths exceeding 1000 nm could be more than doubled.

Roughening the surface of the sample showed comparable results. Niu et al. [4] and Bergström et al. [5] discovered that the surface morphology and surface structure drastically influences the absorption, especially at incident angles below 60° in which a rougher surface generally leads to an increase in the absorption. Niu et al. [4] further concluded that the effect of the incident angle is dependent on the structure of the surface. However, the impact of the incident angle generally becomes less prominent as the surface roughness is increased. Moreover, the polarisation of the laser and the type of laser is known to affect the correlation between the incident angle and the absorption [6]. In addition, Niu et al. [4] investigated the influence of the laser wavelength in the spectrum from 0.4 μm to 4 μm and concluded that the absorption generally decreases with increasing wavelength.

The surface absorption in the solid state of a material can be estimated through a number of theoretical methods and indirect and direct measurement techniques [7]. Theoretical approaches like the classic Drude model [8] and Hagen and Rubens [9] rely on knowledge of parameters such as surface roughness, oxidation, contamination, and material properties.

Indirect measurement techniques are based on computational models to estimate the surface absorption. These methods take into account parameters such as the surface roughness [10], beam intensity [11], angle of incidence [12] and surface temperature [13]. As a result, they generally offer an improved estimation of the surface absorption compared to the purely theoretical methods.

The direct measurement techniques are both accurate and straightforward experimental methods, which can be split into two groups: Methods that directly measure the absorption (calorimetry methods [14]) and methods that indirectly measure the absorption by the radiative properties of the surface, e.g., reflectance and emission (radiometric methods) [7,15]. However, calorimetry methods cannot provide a local estimation of the surface absorption compared to methods that indirectly measure the absorption by the radiative properties of the surface, such as reflectometry and emittance spectroscopy. Kügler and Vollertsen [16] used an integrated sphere to perform reflectometry spectroscopy to determine the absorption of stainless steel. The experimental set-up consisted of a 300 mW laser diode with a wavelength of 1030 nm, which was utilised to radiate the sample, while a Si-photodiode captured the reflected radiation. The integrated sphere spectrophotometry provides simple and highly accurate measurements. Though, as each sample must be placed inside the integrated sphere, it is not sustainable in a flexible production set-up and is further limited in the physical size of the sample.

A range of theoretical models, indirect and direct measurement techniques have been developed for estimating absorption. However, none can provide a local estimation of the absorption for use in a flexible laser marking set-up. As a result, it becomes challenging to locally control the induced heat into the material, which, as mentioned earlier, is a prerequisite for laser marking to obtain a stable process and quality.

The literature review indicates a need for a solution that can determine local changes in the absorption in a flexible manufacturing step-up. The main contribution of this paper is to investigate the feasibility of using a 3D laser scanner to provide an approximation of the absorption as a preceding step for laser marking of stainless steel. By correlating the backscatter from a 3D laser scanner, it is possible to approximate local changes in the surface reflectivity. As the surface reflection is highly dependent on incident angle and perspective, the received backscatter intensity is corrected based on the Cook-Torrance bi-directional surface reflectance (BRDF) model. A series of laser marking experiments are performed to oxidate the surface and create varying levels of reflectivity across the surface of the part to validate the developed method. The results are further compared with the measured values from spectroscopy. The remainder of the paper is organised as follows: In Section 2, the experimental set-up for laser marking and geometrical and intensity measurements is presented. In Section 3, the developed method for correcting intensity values and identifying areas with increased or decreased surface reflectivity is shown. In Section 4, the results are presented and discussed. Section 5 includes the concluding remarks of the paper.

2. Experimental set-up

The experimental set-up is presented in Figure 1 and Figure 2, which, respectively, illustrates laser processing and geometrical and reflectivity measurements of a part. The laser processing set-up consists of a 3 kW IPG YLS-3000 SM laser connected to a modified HighYag processing head. The focal length is 470 mm with a collimated beam diameter of 11.05 mm. The beam quality is 1.2 M^2 with a wavelength of 1076 nm. The measurement set-up consists of a Wenglor MLWL153 3D line scanner, which is applied to acquire a 3D surface representation of the processed parts. The scanner uses a class 3R laser beam with a wavelength of 407 nm and a CMOS sensor to determine the position of the projected laser. The CMOS sensor can further measure the backscatter intensity from the projected laser in a 10-bit greyscale resolution.

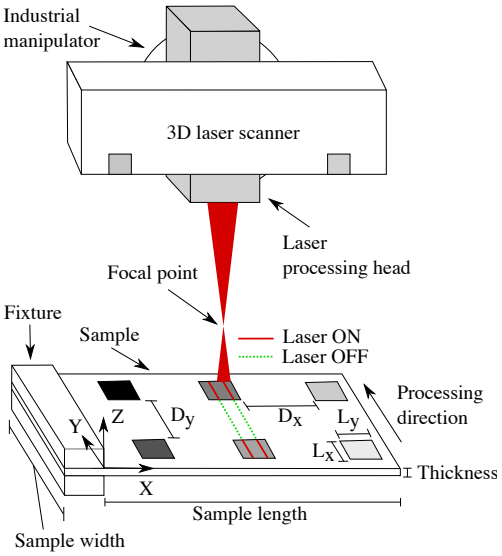

Figure 1. Laser processing set-up for laser marking.

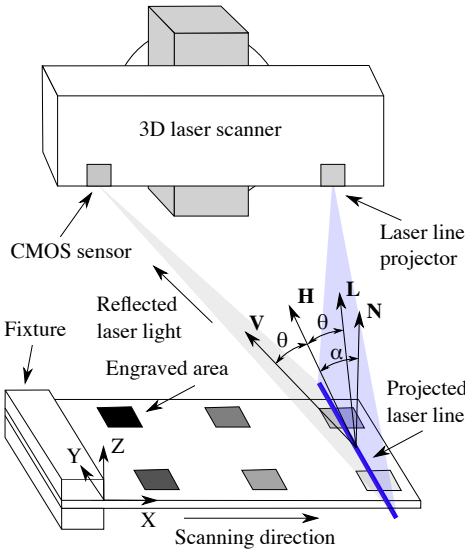

Figure 2. Measurement set-up for geometrical and intensity measurements. The projected laser line is observed by the CMOS sensor at a varying angle depending on the distance to the measured surface.

It should be noted that the specifications of both the laser and the optical components in the scanner are not disclosed by the manufacturer and, therefore, unknown to the authors. The processing head and the 3D line scanner are mounted onto and manipulated by a KUKA KR120 R2700 industrial robot for accurate and flexible positional control. Additionally, spectroscopy measurements have been performed using a LAMBDA 1050+ UV/Vis/NIR spectrophotometer with an integrated sphere to capture diffuse and specular reflectance at normal incidence. Each measured reflectivity is taken as an average of three measurements with a spacing of approximately 5 mm apart. The measured spot size was 3 x 3 mm.

The experiments consisted of three main phases: laser marking, laser scanning and spectroscopy. Spectroscopy and 3D scanning were done preceding laser marking to establish a set of reference values. Subsequently, laser marking was performed on the samples at varying speeds and power levels to generate different oxidation levels and different surface reflections. Finally, spectroscopy was performed again, along with 3D scanning of the samples. Table 1 states the parameters used for laser marking and 3D scanning, while Table 2 includes an overview of the experimental samples. The area # of Table 1 refers to the processed/engraved area, as illustrated in figures 2 and 3.

Table 1. Overview of samples for laser marking and reflectance measurements.

Area #	Scanning speed [mm/min]	Power [W]	Pulse frequency [Hz]	Duty cycle [%]	Spot size [mm]	Overlap [%]	3D scanning speed [mm/min]	3D scanning exposure time [ns]
1	7000	2300	5000	11	1	80	15000	400
2	7300	2300	5000	11	1	80	15000	400
3	7000	2100	5000	11	1	80	15000	400
4	7300	2100	5000	11	1	80	15000	400

Table 2. Overview of samples for laser marking and reflectance measurements. All samples are of rolled AISI 304L stainless steel plates.

Sample #	Treatment	Size [mm x mm x mm]	Reflection [%] λ = 407 nm	Reflection [%] λ = 1076 nm
1	Untreated	100 x 100 x 2	48.60	58.84
2	Untreated	100 x 100 x 2	48.65	62.83
3	Treated with WD-40	100 x 100 x 2	35.77	46.65
4	Treated with WD-40	100 x 100 x 2	37.90	49.65
5	Ground P80 – linear pattern	100 x 100 x 2	53.28	62.68
6	Ground P80 – random pattern	100 x 100 x 2	51.44	60.52

3. Method

The proposed method is based on measuring backscatter from a 3D scanner to locally approximate changes in the reflectivity of the laser light from the 3D scanner. The 3D scanner uses laser triangulation principles, which rely on geometric relations between the projected beam and the CMOS in the scanner. As the beam is projected in an opposite V-shape from the scanner onto the surface, the incident angle of the beam changes across the scanning width (Y-direction of Figure 2). For a perfect diffuse or Lambertian surface, the reflected light is scattered homogenously into the hemisphere, and the surface will hence appear equally bright regardless of the observed perspective. Lambert's cosine law defines a directly proportional relationship between the cosine of the incident angle and surface normal and the amount of reflected light in the given direction. Thus, it is apparent from Lambert's law that the measured backscatter intensity will not be constant across a flat surface. However, perfectly diffuse surfaces are rare in practice, as the majority of surfaces compose of an additional specular component that represents light being concentrated around the mirror direction. This is especially problematic when scanning reflective surfaces, i.e., rolled steel and other metals, as light can be reflected directedly into the sensor, resulting in high local backscatter intensities.

The ratio between the diffuse and specular components of reflected light depends on the optical properties of the surface, i.e. surface roughness and material composition [17]. The remainder of light that is not reflected will either be transmitted or absorbed by the material, hence equation (1):

$$I_i = I_d + I_s + I_a + I_t \tag{1}$$

I_i is the radiance of incident light, I_d is the diffused radiance, I_s is the specular radiance, I_a is the absorbed radiance, and I_t is the transmitted radiance, which for opaque materials like steel is typically zero. Hence, the absorbed radiance I_a can be approximated by determining I_i, I_d and I_s.

The 3D scanner is utilised to acquire 3D geometrical data of the surface and the corresponding backscatter intensities at each point in the shape of a point cloud. The reflection characteristics of the surface can be determined by modelling the specular and diffusion reflection using a bi-directional reflectance model (BRDF). The result is a rendered surface, which will act as a reference for determining changes in reflectivity across the actual surface. This approach aims to correct the received backscatter intensities and minimise the geometrical effects resulting from changes in incident angles. The Cook-

Torrance model, proposed by Cook and Torrance [18], is a BRDF based on optics theory and is well suited for rendering metallic surfaces. Furthermore, it can be generalised for numerous surfaces and represent both diffuse and specular reflections. Other mathematically simpler BRDF models are only able to represent diffuse surfaces (Oren-Nayer [19]) or have been shown not to be realistic enough for applicability (Blinn-Phong [20]). The Cook-Torrance model is further physically plausible, meaning that it obeys the laws of energy conservation and the Helmholtz Reciprocity. It should, however, be noted that the Cook-Torrance model assumes that the light is unpolarised and that the surface is isotropic, which can be a problematic assumption when dealing with ground surfaces. Reflection from other objects is also not considered. As stated by Cook and Torrance [18], the bi-directional reflectance can be expressed as the ratio between the reflected intensity from one direction and the incident radiance from another direction. Hence, the reflected intensity is given by equation (2):

$$R = \frac{I_r}{I_i(\mathbf{N} \cdot \mathbf{L})\mathrm{d}\omega_i} \tag{2}$$

Where I_r is the reflected intensity, I_i is the incident radiance, while $\mathrm{d}\omega_i$ is the differential solid angle of the light source i. $\mathbf{N}$ is the surface normal, and $\mathbf{L}$ is the unit vector in the direction of the incident light, as illustrated in Figure 2. The Cook-Torrance BRDF represents the reflection as the sum of the diffuse R_d and specular R_s reflection, controlled by the material-dependent specular s and diffuse d fractions as given by equation (3).

$$R = sR_s + dR_d, \qquad \text{where } s + d = 1 \tag{3}$$

Based on equation (2), the intensity reflected into the sensor I_r is then given by equation (4).

$$I_r = RI_i(\boldsymbol{N} \cdot \boldsymbol{L})\mathrm{d}\omega_i \tag{4}$$

By introducing the ambient light term I_a and its corresponding reflectivity R_a, the intensity of the reflected light I_r can be expressed as the sum of the ambient term and the sum of the contribution from each light source. The ambient term consists of light that is not directedly pointed at the surface. In this case, the laser from the 3D scanner is represented as a number of individual light sources with small solid angles $\mathrm{d}\omega_i$, which combined make up the entire width of the projected beam. To reduce computational complexity, it is assumed that each light source l only radiates the single point (or pixel of the rendered surface) that it hits. In this case, the reflectance intensity I_r is not computed over the entire hemisphere and thus only represents the reflection from a single point I_p in a single direction (direction of the CMOS sensor). I_p is then expressed in equation (5).

$$I_p = I_{ia}R_a + I_{il}(\boldsymbol{N} \cdot \boldsymbol{L_l})\mathrm{d}\omega_{il}(sR_s + dR_d) \tag{5}$$

Computing I_p for all points in the acquired point cloud from the 3D scanner will result in a 1 × n vector that can be rearranged into a matrix form to be represented as a 2D rendered image of the surface reflection.

The specular reflection R_s can be expressed by combining the Fresnel term, the facet slope distribution D and the shadowing-masking term G, as given by equation (6).

$$R_s = \frac{F}{4}\frac{DG}{(\boldsymbol{N} \cdot \boldsymbol{L})(\boldsymbol{N} \cdot \boldsymbol{V})} \tag{6}$$

$\mathbf{V}$ is the unit vector in the direction of the observer, which in this case is the CMOS sensor in the scanner. The Fresnel term F introduces wavelength dependence to the model and expresses the reflectance of a perfectly smooth surface based on the index of refraction n. For most metals, the index

of refraction has experimentally been determined and can be found in the literature [21]. The Fresnel term is approximated using the cheaper Schlick approximation [22], given by equation (7).

$$F = F_0 + (1 - F_0)[1 - (\mathbf{L} \cdot \mathbf{H})]^5, \qquad \text{where } F_0 = \left(\frac{1-n}{1+n}\right) \tag{7}$$

The diffuse reflection R_d is assumed to be of the same colour as the specular reflection R_s and is therefore expressed as $\underline{R_d} = F_0/\pi$. Assuming that the ambient light is uniformly incident on the surface, the ambient reflectivity can be defined as $R_a = \pi R_d$. Assuming that the surface consists of a distribution of microfacets D that only reflect specular light, the angular spread of the specular component s can be determined. It should be noted that it is merely micro facets whose normal are in the direction of the normalised bi-sector vector $\mathbf{H}$ that contribute to the observed specular reflection. $\mathbf{H}$ is defined such that $\cos(\theta) = \mathbf{V} \cdot \mathbf{H} = \mathbf{L} \cdot \mathbf{H}$, where θ is the angle between $\mathbf{V}$ and $\mathbf{H}$ or $\mathbf{L}$ and $\mathbf{H}$, as illustrated in Figure 2. As given by equation (8), the Beckman distribution considers the root mean square (RMS) of the facet slopes σ and is based on Gaussian roughness assumptions. The Beckman distribution is the commonly preferred distribution in the literature [23].

$$D(\mathbf{N}) = \frac{1}{\pi\sigma^2(\mathbf{N} \cdot \mathbf{H})^4} \exp\left[\frac{-\tan^2(\alpha)}{\sigma^2}\right], \qquad \text{where } \alpha = \cos^{-1}(\mathbf{H} \cdot \mathbf{N}) \tag{8}$$

Small values of σ represent a relatively smooth surface, resulting in a highly directional specular component, while higher values of σ represent steep facet slopes and, therefore, a rougher surface. The shadowing-masking term G describes the probability of a microfacet being visible in the ingoing (shadowing) and outgoing (masking) and is thus angular dependent [24]. Walter et al. [23] recommend using the Smith approximation, equation (9), as it serves as a more realistic representation compared to the term initially proposed by Cook and Torrance [18].

$$G_1(\mathbf{V}, \mathbf{H}) = \chi^+\left(\frac{\mathbf{V} \cdot \mathbf{H}}{\mathbf{V} \cdot \mathbf{N}}\right) \begin{cases} \dfrac{3.535y + 2.181y^2}{1 + 2.276y + 2.577y^2} & \text{if } y < 1.6, \\ 1 & \text{otherwise} \end{cases} \tag{9}$$

Where $y = (\sigma \tan \langle \mathbf{V}, \mathbf{N} \rangle)^{-1}$ and $\langle \mathbf{V}, \mathbf{N} \rangle$ is the angle between the unit vectors $\mathbf{N}$ and $\mathbf{V}$. As the Smith G approximation is a product between the two monodirectional shadowing terms G_1, G is given by equation (10).

$$G(\mathbf{L}, \mathbf{V}, \mathbf{H}) \approx G_1(\mathbf{L}, \mathbf{H}) \cdot G_1(\mathbf{V}, \mathbf{H}) \tag{10}$$

The unit vectors $\mathbf{N}$, $\mathbf{H}$, $\mathbf{V}$ and $\mathbf{L}$ are acquired from the 3D geometrical data from the point cloud. As the laser specifications from the 3D scanner are unknown to the authors, it is impossible to directly compute the intensity of the incident light I_i. The RMS value of the facet slope σ of the surface is equally an unknown parameter. The same applies to the intensity of the ambient light I_a and the specular and diffuse fractions s and d. The diffuse fraction d can be computed based on equation (3), hence $d = s - 1$. The RMS facet slope σ, the fraction of specular light s and the intensity of the incident and ambient light, respectively I_i and I_a, are determined through a non-linear least square problem by minimising the difference between the computed reflectance intensities I_p and the acquired backscatter intensities I_b from the 3D scan. The fitted parameters (σ, s, I_i, I_a) are then applied to generate a perfect reference surface W_r free from any local changes in reflection due to surface contamination or oxidation. A rendered surface is illustrated in Figure 3 (left).

The acquired backscatter intensities I_b from the 3D scanner, Figure 3 (right), is reshaped as a matrix W_b and then compared to the generated reference surface W_r. This results in the relative change in

reflectivity (or light intensity) ΔR, given by equation (11). ΔR is illustrated as an image in Figure 3 (right).

$$\Delta R = \frac{W_r}{W_b} \cdot 100 \tag{11}$$

As it is challenging to accurately determine surface absorption values, it is chosen to approximate the relative change in reflectivity ΔR. As it is clear from equation (1), the reflectivity is directly related to the absorption. By assuming that no light is transmitted through the material, a change in the surface reflection corresponds to a change in the surface absorption.

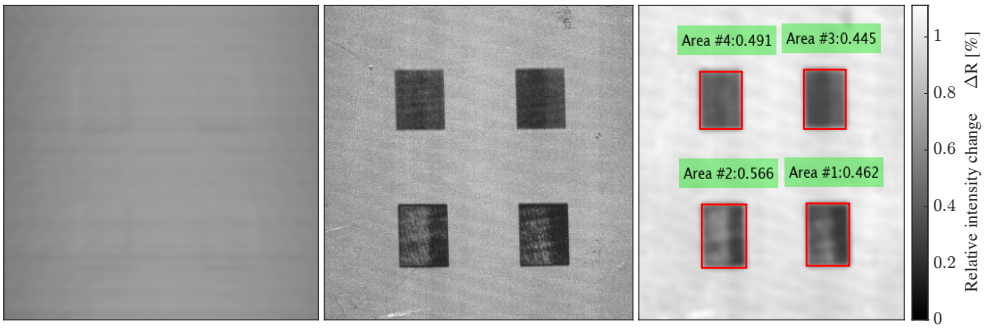

Figure 3. Left: Rendered image W_r of the surface of Sample 3 based on the Cook-Torrance BRDF model. Centre: Intensity backscatter surface W_b acquired by the 3D scanner of Sample 3. Note that the processed areas have a decreased ΔR, observed as the darker areas. Right: An image based on relative intensity change ΔR between the rendered surface W_i and the backscatter intensities W_b. Note that the values on the figure are the average ΔR within each red rectangular outline.

4. Results and discussion

The estimated relative change in reflectivity ΔR of all samples across selected, processed areas is compared with ΔR values obtained through spectroscopy. The reference values used to compute ΔR for the spectroscopy measurements is the reflectivity of the given sample before processing. Table 3 presents an overview of the measured ΔR using both the 3D scanner, spectroscopy at λ = 405 nm and λ = 1076 nm. Due to limited resources with the spectrophotometer, only samples 2 and 3 have been measured in all processed areas.

Table 3. Overview of relative change in reflectivity ΔR obtained from the 3D scanner and spectroscopy

	ΔR 3D scanning [%]				ΔR Spectroscopy [%], λ = 405 nm				ΔR Spectroscopy [%], λ = 1076 nm			
Area #	# 1	# 2	# 3	# 4	# 1	# 2	# 3	# 4	# 1	# 2	# 3	# 4
Sample 1	34	45.9	40.8	44.5		37.6		26.1		81.6		96.1
Sample 2	33.9	44.1	45	48.2	32.3	25.6	26.9	30.7	86.8	90.5	98	99.1
Sample 3	46.2	56.6	44.5	49.1	55.6	45.6	32.8	39.1	103.2	99.4	122.3	123.4
Sample 4	42.3	50.8	47.5	49.1		52.8		35.9		98.2		117.4
Sample 5	43.7	48.6	32.4	39.4		38.9		34.1		76.3		94.7
Sample 6	26.6	60.6	44.2	56.2		37.2		30.9		81.1		95.4

Table 4 presents a percentage comparison of the determined ΔR values from Table 3 based on the relation presented in equation (12).

$$C = \frac{\Delta R_{scan} - \Delta R_{spectroscopy}}{\Delta R_{spectroscopy}} \cdot 100\ \% \tag{12}$$

Table 4. 3D scanning versus spectroscopy. Percentage comparison of ΔR.

	C Spectroscopy [%], λ = 405 nm				C Spectroscopy [%], λ = 1076 nm			
Area #	# 1	# 2	# 3	# 4	# 1	# 2	# 3	# 4
Sample 2	4.95	72.27	67.29	57	-62.79	-71.71	-72.5	-51.36
Sample 3	-16.91	56.6	35.67	36.78	-55.23	-44.06	-63.61	-58.18

The results of tables 3 and 4 show that the proposed solution can identify changes in the reflection. However, there is generally a significant deviation (in some cases > 70%) in the measured ΔR values compared to spectroscopy. As isotropy is assumed in the model, a deviation is expected in the ground samples 4 and 5. The deviation is further expected to be substantial when comparing ΔR from the 3D scanner to those obtained by spectroscopy at λ = 1076 nm due to the difference in the wavelength. Therefore, the application of the proposed method should be made using a measuring laser that has a wavelength closer to that of the applied processing laser to minimise approximation error. Another source of error could be due to the presented laser marking experiments being conducted on standard industrial AISI 304L sheet metal to resemble a real industrial manufacturing scenario. This induced that the surface of the samples was not entirely homogeneous, which produces a visible variation in the absorption and thereby the marking results, as seen in Figure 4 (left). This effect was evident compared to the results presented by Antończak et al. [1] conducted on well-prepared surfaces. As the spectroscopy measurements are performed in an area of 3 x 3 mm, there is additionally a possible risk of accidentally measuring an area with considerably higher absorption.

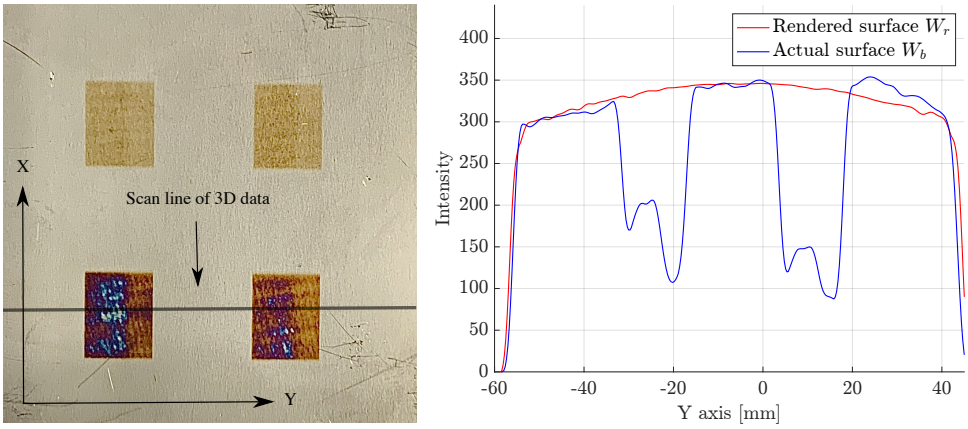

Figure 4. Left: A photograph of Sample 4 after laser marking. The different oxidation levels as a result of the induced heat are apparent. Right: A comparison of the rendered reference W_r and backscatter intensity W_b at a random scan line, indicated by the left figure. Note that the rendered surface follows the actual surface except for the oxidised areas as intended.

It can be observed from Figure 4 that the implemented model performs as intended. The rendered surface of W_r follows the actual surface W_b in the non-oxidised areas, which results in a relative change

in reflectivity ΔR, which approaches one. However, in the processed/oxidised areas, ΔR drops rapidly, which is expected as the surface colour has shifted into the red area as this in the opposite spectrum compared to the scanner laser's blue colour. It can further be observed from the rendered surface of Figure 4 that the highest intensity is not measured at the centre of the field of view. The slight shift away from the centre signifies that the sample is rotated at a small angle relative to the scanner, thus underlining the necessity of correcting the intensity for geometric effects.

From additional experiments, it was concluded that the ambient light has no substantial effect on the results. The method has also been tested at incident angles above 30°. Due to the specular nature of the measured surfaces, light is reflected away from the sensor, and the reflection could not be satisfactorily approximated. The proposed model was also able to render realistic surfaces for titanium, construction steel and aluminium. Though these samples were not laser marked, and thus any change in relative reflectivity was not approximated. Highly reflective or mirror-like surfaces are expected to be problematic, as the Cook-Torrance model is not well suited for such surfaces. In addition, the model is expected to be applicable for very rough surfaces that exhibit multi-reflections, assuming an isotropy random roughness as such surfaces will likely act as diffuse reflectors. Note that performing measurements simultaneously with active laser processing should be avoided, as processing light inevitably will be reflected into the CMOS sensor of the scanner, drastically influencing the results.

5. Conclusion

The study has examined the feasibility of applying a 3D scanner to measure backscatter intensities for determining surface absorption of stainless steel samples. The proposed solution is based on the Cook-Torrance BRDF to model the reflectance across the surface to generate a reference surface free of containments and oxidation. The generated reference surface is compared to the actual surface, acquired as backscatter intensity data from the 3D scanner. The ratio between the reference surface and the actual surface defines the relative change in reflectivity or absorption. The proposed solution was proven feasible as it could identify a change in the reflectivity locally across the surface when measuring an oxidised surface from laser marking.

Comparing the approximated change in reflectivity to those acquired by spectroscopy at the same wavelength (λ = 405 nm) showed a deviation of more than 70% in some cases. At the wavelength (λ = 1076 nm) of the processing laser, the deviation was more substantial, and thus an application of the proposed solution should be made using a measurement laser with a comparable wavelength. Part of the significant deviation could be attributed to noisy spectroscopy measurement. Research into establishing a mathematical relation between the approximated reflectance and the measured reflectance from spectroscopy could potentially improve the results.

The proposed solution shows significant potential for identifying areas with a potentially large change in absorption. In a production set-up, this knowledge could be applied to reject samples before processing. Providing a clean and homogenous surface for laser marking of samples and hence a better base for model verification could aid in defining the potential for the proposed solution. The results show that further work is necessary to improve the modelled accuracy and applicability of the model. This could include fitting a complete BRDF model to backscatter data acquired from a larger variation in scanning angles, thus making it possible to model the entire reflection into the hemisphere. In addition, introducing an anisotropic term to the model would add to the flexibility of the model.

Acknowledgements

The authors would like to acknowledge Peter Kjær Kristensen from Aalborg University for guiding the spectroscopy measurements. Innovation Fund Denmark, the INTERLASE project, with number 7050-00024B is gratefully acknowledged for supporting this project. The experimental equipment used for this project was supported by the Poul Due Jensen Foundation.

ORCID iDs
A F Mikkelstrup https://orcid.org/0000-0001-8209-6787
A N Thomsen https://orcid.org/0000-0003-4865-1032
M Kristiansen https://orcid.org/0000-0001-9652-3348

References

[1] Antończak A J, Stępak B, Kozioł P E and Abramski K M 2014 The influence of process parameters on the laser-induced coloring of titanium *Appl. Phys. A Mater. Sci. Process.* **115** 1003–13
[2] Dausinger F and Shen J 1993 Energy Coupling Efficiency in Laser Surface Treatment *ISIJ Int.* **33** 925–33
[3] Abedi H R and Hoseinpour Gollo M 2019 An experimental study of the effects of surface roughness and coating of Cr2O3 layer on the laser-forming process *Opt. Laser Technol.* **109** 336–47
[4] Niu C, Zhu T and Lv Y 2019 Influence of Surface Morphology on Absorptivity of Light-Absorbing Materials *Int. J. Photoenergy* **2019** 1-9
[5] Bergström D, Powell J and Kaplan A F H 2008 The absorption of light by rough metal surfaces-A three-dimensional ray-tracing analysis *J. Appl. Phys.* **103** 1–12
[6] Davim J P 2013 Laser Beam Manufacturing *Nontraditional Machining Processes* ed J P Davim (London: Springer London) chapter 2 pp 35-96
[7] Indhu R, Vivek V, Loganathan S, Bharatish A and Soundarapandian S 2018 Overview of Laser Absorptivity Measurement Techniques for Material Processing *Lasers Manuf. Mater. Process.* **5** 458–81
[8] Drude P 1900 Zur Elektronentheorie der Metalle *Ann. Phys.* **306** 566–613
[9] Hagen E and Rubens H 1903 Über Beziehungen des Reflexions- und Emissionsvermögens der Metalle zu ihrem elektrischen Leitvermögen *Ann. Phys.* **316** 873–901
[10] Ang L K, Lau Y Y, Gilgenbach R M and Spindler H L 1997 Analysis of laser absorption on a rough metal surface *Appl. Phys. Lett.* **70** 696–8
[11] Blidegn M S K and Olsen F O 1997 Investigation into the absorptivity change in metals with increased laser power *XI Int. Symp. Gas Flow Chem. Lasers High-Power Laser Conf.* **3092** 615-8
[12] Wang H, Kawahito Y, Yoshida R, Nakashima Y and Shiokawa K 2018 A model to calculate the laser absorption property of actual surface *Int. J. Heat Mass Transf.* **118** 562–9
[13] Wang J T, Weng C I, Chang J G and Hwang C C 2000 The influence of temperature and surface conditions on surface absorptivity in laser surface treatment *J. Appl. Phys.* **87** 3245–53
[14] Rubenchik A M, Wu S S Q, Kanz V K, LeBlanc M M, Lowdermilk W H, Rotter M D and Stanley J R 2014 Temperature-dependent 780-nm laser absorption by engineering grade aluminum, titanium, and steel alloy surfaces *Opt. Eng.* **53** 122506
[15] Bergström D 2008 *The absorption of laser light by rough metal surfaces* (Luleå University of Technology)
[16] Kügler H and Vollertsen F 2018 Determining Absorptivity Variations of Multiple Laser Beam Treatments of Stainless Steel Sheets *J. Manuf. Mater. Process.* **2** 84
[17] Vukašinovíc N, Bračun D, Možina J and Duhovnik J 2010 The influence of incident angle, object colour and distance on CNC laser scanning *Int. J. Adv. Manuf. Technol.* **50** 265–74
[18] Cook R L and Torrance K E 1982 A Reflectance Model for Computer Graphics *ACM Trans. Graph.* **1** 7–24
[19] Oren M and Nayar S K 1994 Generalization of Lambert's reflectance model *Proc. 21st Annu. Conf. Comput. Graph. Interact. Tech. SIGGRAPH 1994* 239–46
[20] Blinn J F 1977 Models of light reflection for computer synthesized pictures *Proc. 4th Annu. Conf. Comput. Graph. Interact. Tech. SIGGRAPH 1977* 192–8
[21] Johnson P B and Christy R W 1974 Optical constants of transition metals: Ti, V, Cr, Mn, Fe,

Co, Ni, and Pd *Phys. Rev. B* **9** 5056–70
[22] Schlick C 1994 An Inexpensive BRDF Model for Physically-based Rendering *Comput. Graph. Forum* **13** 233–46
[23] Walter B, Marschner S, Li H and Torrance K 2007 Microfacet models for refraction through rough surfaces *Eurographics* 195–206
[24] Heitz E 2014 Understanding the Masking-Shadowing Function in Microfacet-Based BRDFs *J. Comput. Graph. Tech.* **3** 48–107

Paper D

Quality Inspection System for Robotic Laser Welding of Double-curved Geometries

Anders Faarbæk Mikkelstrup, Mathias Ernst Thomsen, Kristoffer Stampe, Benny Ørtoft Endelt, Jens Vestergaard Boll, Ewa Kristiansen, and Morten Kristiansen

The paper has been published in the
Procedia Manufacturing, vol. 36, pp. 50-57, 2019.

Available online at www.sciencedirect.com

ScienceDirect

Procedia Manufacturing 00 (2019) 000–000

Procedia MANUFACTURING

www.elsevier.com/locate/procedia

17th Nordic Laser Material Processing Conference (NOLAMP17), 27 – 29 August 2019

Quality Inspection System for Robotic Laser Welding of Double-Curved Geometries

Anders Mikkelstrup[a], Mathias Thomsen[a], Kristoffer Stampe[a], Benny Endelt[a], Jens Boll[b], Ewa Kristiansen[a], Morten Kristiansen[a]

[a]*Aalborg University, Departement of Materials And Production, 9220 Aalborg, Denmark*
[b]*Grundfos A/S, 8850 Bjerringbro, Denmark*

Abstract

The quality of robotic laser welded parts is related to the joint location, the trajectory of the laser focal point and the process parameters. By performing in-process monitoring, it is possible to acquire sufficient process knowledge for post-inspection to evaluate the geometrical weld quality. The existing solutions for such systems operate along linear welds. This paper contributes with a quality inspection system for robot laser welding, that can handle double-curved geometries. The data acquisition system includes a CMOS camera, which is mounted such that it looks through the laser optics, external LED illumination and matching optical filters. During the process, the area around the moving laser focal point is captured, resulting in a sequence of images. The trajectory of the focal point is determined by estimating the 2D displacement field between each image. This is done by applying template matching and subsequently filtering the data through a Kalman filter, that is aided by a radial basis neural network to improve the accuracy and robustness of the system. The joint location is determined by applying a Canny edge detector and a standard Hough transform within a specified region of interest. As this paper deals with double-curved geometries, the region of interest is moved in relation to the laser trajectory, such that it always contains the visible part of the joint, that is closest to the focal point. The developed post-inspection system evaluates the quality of the weld based on the output of the in-process monitoring system by comparing the estimated trajectory relative to the determined location of the joint. The performance of the proposed quality inspection system was validated empirically on 18 samples. The tests showed promising results, as the system was able to accurately detect changes in the welding trajectory relative to the location of the joint with an accuracy of ± 0.2 mm.

Peer-review under responsibility of the scientific committee of the 17th Nordic Laser Material Processing Conference.

Keywords: Laser welding; Quality inspection; Image processing; Welding trajectory; Vision system

1. Introduction

High-power fiber laser welding is becoming increasingly popular in the mass-production industry for joining both ferrite and non-ferrite sheet metal plates due to its ability to produce a high-intensity heat source, that can be precisely

Peer-review under responsibility of the scientific committee of the 17th Nordic Laser Material Processing Conference.

focused onto a small area. This enables the possibility of producing key hole welds at high speeds, while limiting the heat affected zone. A consequence of this is, however, strict tolerances to joint alignment and lateral positioning of the laser focal point to ensure structural integrity and fatigue life of the weld, especially in autogenous laser welding processes. In automated production set-ups, where the laser welding optics are manipulated by using a six-axis robot, the need for process monitoring and trajectory tracking is further emphasized. This is mainly due to positional inaccuracies in the robot's repeatability, especially along (complex) 3D welding trajectories at high speeds.

In the recent past, the topic of joint monitoring, seam tracking and online control of the laser welding process has been highly researched. The majority of published papers within this field of study have utilized a monitoring system containing similar key elements, which include an image sensor, a narrow band-pass filter, a powerful light source with a specific wavelength and in some cases a neutral density filter. [1, 2, 3]

M. de Graff, et al. [4] and W. Cieszyński, et al. [5] all used the aforementioned approach, coupled with common image processing techniques such as BLOB- analysis and edge detection to analyze the laser welding process. With this type of monitoring system, they respectively succeeded in mapping and monitoring 3D butt joints, tracking the laser focal point and online correction of joint misalignment. R.-K. Zäh, et al. [6] and S. M. Portnov, et al. [7] proposed an alternative approach for monitoring of the laser welding process, utilizing a photo detector to detect emitted light from the process has also been proposed. These monitoring systems made it possible to set up a mathematical model of the laser welding process to improve control of deep penetration welds. In order to improve robustness of the laser welding vison-based monitoring systems, M. Nilsen, et al. [8] implemented a Kalman filter to estimate the joint gap, where the image processing had failed. This method turned out to improve robustness of the monitoring system and also reduced computation time, compared to other approaches. X. Gao, et al. [9] improved the robustness even further by combining a Kalman filter with a radial basis function neural network to account for dynamic colored noise, thereby improving the estimation capabilities of the Kalman filter.

This paper deals with the challenge of acquiring a sufficient amount of robust process data for post inspection of laser welds, that have been performed along curved three-dimensional trajectories, as illustrated in Fig. 1. (a). More specifically, autogenous robotic laser welding of pre-worked thin stainless-steel metal plates. The aim is to detect changes in the welding trajectory in relation to the joint position, with the purpose of ensuring a stable and acceptable weld quality. The failure mode, illustrated in Fig. 1. (b), is a result of short- and long-term process disturbances. Short term disturbances are defined as Gaussian noise, such as misplacement of the sub-components, while long term process disturbances are defined as time-dependent noise, e.g. temperature shifts or tool wear.

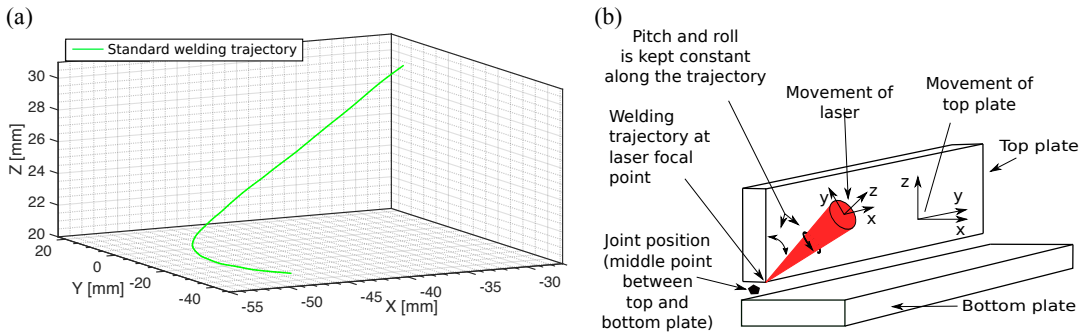

Fig. 1. (a) The green line indicates the curved three-dimensional welding trajectory of interest in the global coordinate system.; (b) The failure mode is defined as a misalignment in the welding trajectory in relation to the position the joint. The position of the joint is defined as the middle point between the top and the bottom plate. However, it should be noted, that a change in the position of the laser focal point in the axial direction (Z-direction) of the laser is not considered to be within the scope of this paper.

The approach is based on an image sequence, captured with a CMOS camera through the laser optics during welding. The monitoring system proposed in this paper applies a combination of a Canny edge detector and a standard Hough transform to determine the joint position. Template matching is used to estimate the displacement field between subsequent image frames for computing the welding trajectory. In an effort to improve the prediction capability,

precision and overall robustness of the estimations, a Kalman filter combined with a radial basis function, neural network, onwards referred to as a neural network, is incorporated into the monitoring system. Validation of the monitoring system is done by comparing the welding trajectory and joint position from the monitoring system to a series of forward kinematic estimations of the welding trajectory. The quality inspection system should be able to detect shifts in the process, such as a varying joint position and an incorrect welding trajectory within a precision of ± 0.2 mm. This is based on the tolerances for joint alignment and lateral positioning of the laser focal point, required to obtain a sufficient weld quality for the material thickness.

2. Experimental set-up

The experimental set-up consists of a solid-state laser, a TruDisk 4001 by manufacturer Trumpf with a 200 µm LLK-D fiber delivery system. It is connected to a Permanova WT04 ST optics with a motorized twin spot unit, that is mounted on a KUKA KR 30 HA 6D robot. The robot is a high accuracy model from KUKA AG with a repeatability of ± 0.05 mm.

The weld of interest in this paper is a double-curved T-joint configuration, illustrated in Fig. 2. (a), consisting of two 4301 austenitic stainless-steel plates with a thickness of respectively 2 mm and 1.5 mm for the bottom and top plate of the T-joint. To minimize heat induced distortions, the plates have been clamped during the welding operation. The weld is performed at a desired speed of 100 mm/s with no filler material and shielding gas, following the curved three-dimensional trajectory, illustrated in Fig. 1. (a).

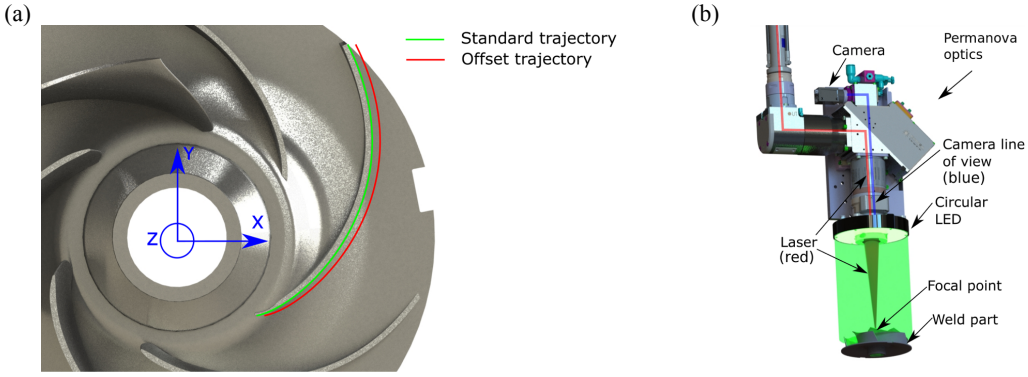

Fig. 2. (a) Presentation of offset in the standard welding trajectory.; (b) Permanova WT04 ST optics with LED light source.

The experimental results were obtained by performing 24 consecutive welds to limit the amount of long-term process disturbances through two different tests scenarios. An overview of the different tests is presented in Table 1.

Table 1. Experimental test overview. All tests are conducted with the same laser spot size, collimation, test set-up and narrow-band-pass filter.

Test	Total welds	Welding speed	Average laser power	Offset	Collimation lens focal length	Focus lens focal length
1-3	18	100 mm/s	3100 W	No	180 mm	300 mm
4	6	100 mm/s	3100 W	Yes	180 mm	300 mm

The first three tests will be defined as standard weld and are performed to establish a reference for the performance of the monitoring system and to investigate the variance between identical samples. Subsequently, Test 4 is performed with a 1 mm offset in the X direction of the standard welding trajectory, as illustrated in Fig. 2. (a), in order to determine the detection capabilities of the monitoring system.

2.1. Image acquisition system

The optics presented in Fig. 2. (b) houses a built-in image acquisition system that includes a Basler acA645-100gm CMOS camera, mounted so its perspective is co-axial with the laser beam. This is illustrated in Fig. 2. (b). The camera has a frame rate of 100 fps and a resolution of 658 × 492 px in 8-bit grey scale. At the focus point, this results in a spatial resolution of 25 × 25 px/mm^2 minimize in-plane rotation and tilt of the camera, the pitch and roll are kept constant along the welding trajectory as illustrated in Fig. 1. (b). The image processing and the related operations are performed in MATLAB 2016b using an Intel Core i7- 6700HQ CPU in combination with 16 GB of memory and a Radeon Pro 450 GPU.

An external light source has been mounted at the end of the Permanova optics, as illustrated in Fig. 2. (b). This is based on the monitoring system described in M. Nilsen, et al. [8]. By synchronising the trigger of the LED light to the exposure time of the camera, it has been possible to run a higher current through the LED light, thus increasing the light intensity in shorts bursts. In addition, matching optical filters consisting of a narrow band pass filter and a neutral-density filter have been mounted in front of the camera lens.

3. Signal processing

The signal processing deals with image processing of the camera signal to estimate the welding trajectory and joint position. In the following sections, n defines the total number of frames captured during the welding operation, while k defines the current frame, counted from the beginning of the captured welding operation.

3.1. Determining joint position using Canny detector and Hough lines

With the purpose of having some reference to indicate if the weld has been performed within the requirements outlined in section 3, the $2 \times n$ joint position matrix $\mathbf{J}(k) = [x(k), y(k)]$ must be established. This is done through a six-step approach, illustrated in Fig. 3.

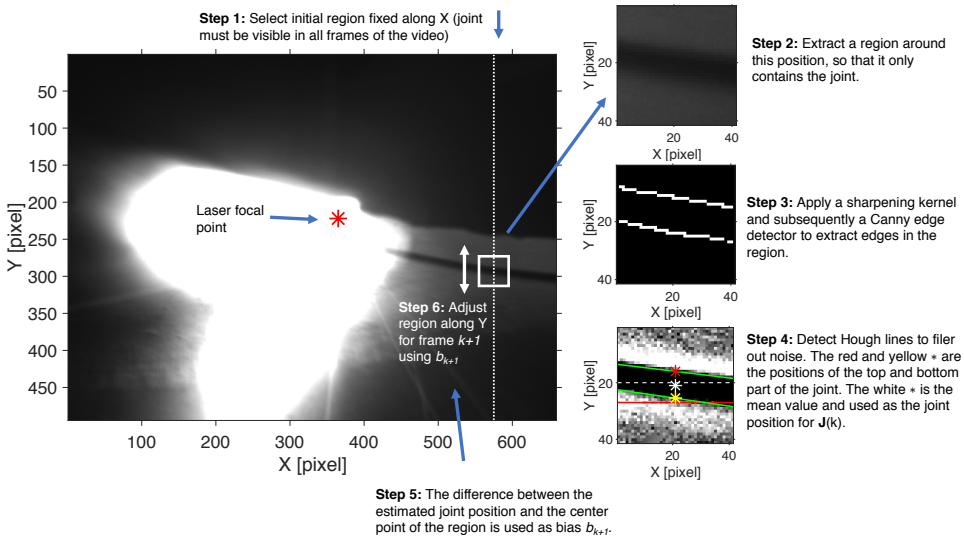

Fig. 3. Camera view with illustration of the steps for determining the joint position of the welding operation. The green Hough lines of step 4 indicate the lines with gradients within the limits, while the gradient of the red line exceeds the limits and is hence considered as noise. As an additional processing step, the joint position matrix **J**(k) is fitted with a 4th degree polynomial to minimize noise and predict missing data points. The above steps are iterated $k = k + 1$ to the next frame until $k = n$. [10, 11]

3.2. Estimation of welding trajectory using normalized cross-correlation template matching

Let Δx and Δy describe the camera's displacement field between subsequent video frames in respectively the X and Y direction in relation to the camera's moving coordinate system. The camera's displacement field is measured by selecting a region around the joint in frame k, similar to the procedure of step 2. The displacement of the region from frame k to $k + 1$ is then determined by performing normalized cross-correlation template matching between the two frames. The region around the joint is selected, as it is distinct and contains high intensity gradients, which are normally easier to track. As there is no in-plane rotation in the video frames, normalized cross-correlation template matching has proven to be more computationally efficient and robust to image noise, compared to more advanced feature matching methods, such as SURF, proposed by H. Bay, et al. [12].

The points defining the estimated welding trajectory $\mathbf{I}(k)$, can be estimated by summing up the displacement field for the previous frames of k, as stated by (1), where $\mathbf{U}(k) = [\Delta x(k), \Delta y(k)]$ is the displacement matrix.

$$\mathbf{I}(k) = \sum_{i=1}^{k} \mathbf{U}(i) \quad \forall k \leq n \tag{1}$$

3.3. Kalman filter for displacement field estimates

The displacement matrix $\mathbf{U}(k) = [\Delta x(k),\ \Delta y(k)]$ contains excessive noise primarily due to light disturbances from the laser beam. As a result, two separate discrete-time Kalman filters, one for X displacement Δx and one for Y displacement Δy is implemented. The two Kalman filters employ almost identical dynamic models to estimate the displacements, only differing in whether they make use of the values belonging to X or Y. (2) presents the state system equation for Δx. The state variables for the process model is chosen as the displacement field at sample k (Δx_1), the change in the displacement from $k - 1$ to k (Δx_2) and the displacement at $k - 1$ (Δx_3).

$$\mathbf{X}(k+1) = \begin{bmatrix} 1 & t & 0 \\ 0 & 1 & 0 \\ 1 & 0 & 0 \end{bmatrix} \begin{bmatrix} \Delta x_1(k) \\ \Delta x_2(k) \\ \Delta x_3(k) \end{bmatrix} + \begin{bmatrix} \frac{1}{2}\Delta t^2 \\ t \\ 0 \end{bmatrix} w_x(k) = \phi \mathbf{X}(k) + \Gamma w_x(k) \tag{2}$$

Where w_x(k) describes the system dynamic noise for Δx. ϕ and Γ being respectively the state transformations matrix and the noise drive matrix. The sampling rate Δt is determined by the frame rate of the camera, thus making $\Delta t = 0.01$ s for this application. The Kalman filters are implemented under the assumption that the weld is performed with a constant speed, and that the camera has a constant distance and angle to the surface of the component. The measurement equation then becomes:

$$\mathbf{Z}(k) = \begin{bmatrix} 1 & 0 & 0 \\ 1 & 0 & -1 \end{bmatrix} \begin{bmatrix} \Delta x_1 \\ \Delta x_2 \\ \Delta x_3 \end{bmatrix} + \mathbf{V}(k) = \mathbf{H}\mathbf{X}(k) + \mathbf{V}(k) \tag{3}$$

In the traditional Kalman filter, the best estimation of the state vector $\mathbf{X}(k)$ relies on conditional variance information, which requires that the system dynamic noise $w_x(k)$ and sensor measurement noise $\mathbf{V}(k)$ are random uncorrelated Gaussian white noise models. However, according to X. Gao et al. [9], the $w(k)$ and $\mathbf{V}(k)$ of the welding process is colored instead of white. X. Gao, et al. [9] proposes to solve this challenge by driving Gaussian white noise through a shaping filter and introducing three associated coefficients λ, α and β. The coefficients λ, α and β and variances are used to tune the performance of the shaping filter and have been determined by a trial-and-error approach and are stated in Table 2.

Table 2. Coefficients for Kalman filters

	Q	**R**	λ	α	β
x	10	$[10^{-3}, 0; 0, 10^{-3}]$	0.3	0.1	0.1
y	50	$[10^{-3}, 0; 0, 10^{-3}]$	0.3	0.1	0.1

In order to incorporate the colored noise into the Kalman filter, the approach of this paper applies the method proposed by X. Gao, et al. [9]. Hence incorporating the state system equation for Δx, stated by (2), the corresponding state system equation for Δy and the coefficients of Table 2. This will not be further outlined in this paper.

The output of the Kalman filter is the predicted and corrected displacement matrix $\tilde{\mathbf{U}}(k) = [\Delta\tilde{x}(k), \Delta\tilde{y}(k)]$, that can be applied to determine the estimated welding trajectory, as by (1).

3.4. Radial basis neural network displacement field prediction

The purpose of the neural network is to act as a more accurate predictor for the Kalman filter, where the image processing is not able to determine the displacement field. The evaluation criteria is defined as the gradient between the displacement field $\mathbf{U}(k)$ and the corrected displacement field $\tilde{\mathbf{U}}(k-1)$, which must not exceed a specified threshold ρ.

$$\left| \frac{\mathbf{U}(k) - \tilde{\mathbf{U}}(k-1)}{\Delta t} \right| < \rho \tag{4}$$

A standard three-layer radial basis function neural network is applied due to its generalization ability, stability and shorter training times, compared to many other neural networks. The input to the neural network is a $1 \times n$ vector $\mathbf{G}(k)$ containing the frame numbers $k = 1 \rightarrow n$ for the current video. The output is the predicted displacement matrix $\mathbf{U}^*(k)$, which is used instead of $\mathbf{U}(k)$ in cases, when ρ is exceeded. Training of the neural network follows the orthogonal least squares algorithm, which is employed as a forward regression method used to determine suitable radial basis function centers, as proposed by S. Chen, et al. [13]. The neural network is trained using $\tilde{\mathbf{U}}(k)$ as the target and $\mathbf{G}(k)$ as the input for the 12 most recent welds.

4. Validation and results

4.1. Geometrical coordinate transformations for system validation

Through a forward kinematic analysis, the KUKA software is able to estimate the position and hence trajectory of the laser focal point during the welding operation and will be used as a reference for comparison. As the image processing estimates the welding trajectory by calculating the trajectory based on the displacement field between subsequent frames from a moving camera, the trajectory is defined in relation to the coordinate system of each individual camera frame. The trajectory from the robot coordinate system is transformed to the moving image coordinate system by rotating the focal point coordinates from the trace analysis in the negative direction and in the opposite order of the angle-set convention, Z-Y-X Euler angles as $\mathbf{R}_{ZYX}$. Transforming the image coordinates to the robot coordinate system is done using the same approach, however, in the original order of the angle-set as $\mathbf{R}_{XYZ}$.

4.2. Performance evaluation

By using the estimated welding trajectory, $\mathbf{I}(k)$ from the monitoring system, the position of the laser focal point can be compared to the joint position $\mathbf{J}(k)$ in the preceding frames. Fig. 4. (a) illustrates an image, where the visible area of the joint of each frame has been combined to form one single image by applying the corrected displacement matrix $\tilde{\mathbf{U}}(k)$. In addition, the estimated joint positions of $\mathbf{J}(k)$ have been plotted in the image for comparison. As

illustrated in Fig. 3., it is essential to note, that due to the large number of saturated pixels, it is not possible to directly compare the deviation between the laser focus point and joint in the same frame.

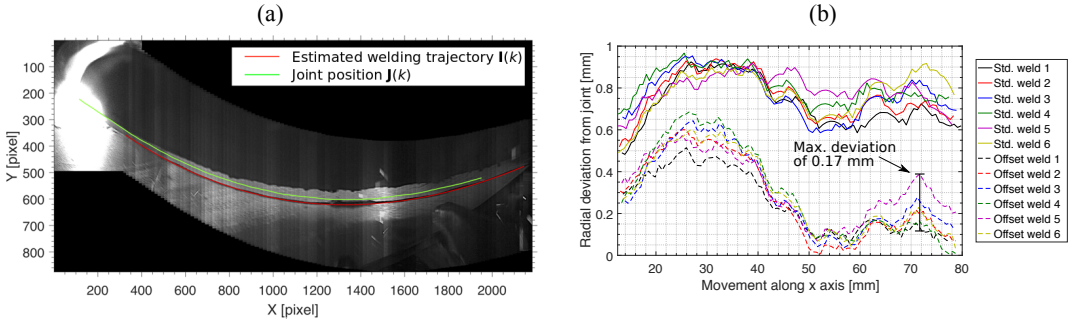

Fig. 4. (a) Visual comparison of the estimated welding trajectory and joint position in each frame of a standard weld. (b) Radial deviation of welding trajectories $\mathbf{I}(k)$ the standard welds of Test 3 versus the offset welds of Test 4, compared to estimated joint positions $\mathbf{J}(k)$.

Fib. 4. (b) shows a comparison of six standard welding trajectories, in this case Test 3 of Table 1, and six offset trajectories from Test 4, all compared to their respective estimated joint position. The differences in the radial deviations of between the welding trajectories $\mathbf{I}(k)$, compared to estimated joint positions $\mathbf{J}(k)$, give an indication of the precision of the estimated welding trajectories and furthermore evaluates the system's ability to precisely detect process disturbances. The maximum deviation is 0.17 mm, which occurred on Test 3, as illustrated in Fig. 4. (b). By computing the deviation between the estimated joint positions $\mathbf{J}(k)$ of six welds, it is possible to evaluate the precision and robustness of the joint locater. Fig. 5. (a) shows the difference in the Y coordinate of the joint positions for all frames from the videos of Test 3. The X coordinate of the joint is fixed in all frames and is therefore not considered. The joint positions are compared to a reference, that has been determined by a neural network. In this case, it is roughly a weighted average of all the joint positions. The results show, that the maximum deviation is within the requirements of ± 0.2 mm.

The deviation between the trajectory and the joint position in the Y direction of both the standard and the 1 mm offset weld is transformed into the global robot coordinate system. The results are illustrated in Fig. 5. (b).

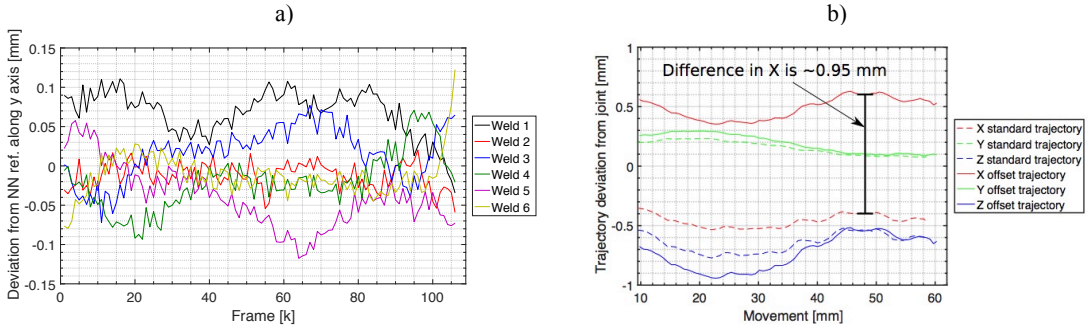

Fig. 5. (a) Deviation in the joint position $\mathbf{J}(k)$ of six welds compared to a neural network reference.; (b) Comparison of estimated standard trajectory $\mathbf{I}(k)$ versus estimated offset trajectory transformed into the global coordinate system of the robot.

The results indicate, that the mean offset is approximately 0.95 mm in the X direction, which corresponds to the actual offset of 1 mm between the standard and offset weld. In addition, the results indicate a slight offset in both the Y and Z direction, which is likely a consequence of image noise and inaccurate synchronizing of the data from the forward kinematic analysis of the robot and the data from the quality inspection system.

The total cost time of the monitoring system, i.e. estimating joint position and welding trajectory for $n = 106$ frames, excluding loading of video and plotting is 3.05 s. For comparison, the welding operation elapses 1.16 s pr. weld.

5. Conclusion

This paper proposed a monitoring system to deal with the challenges of acquiring a sufficient amount of robust process data for post inspection of autogenous laser welds, that have been performed along curved three- dimensional trajectories. The monitoring system, purely rely on template matching for determining the frame displacement field showed promising results, however, it suffered from instabilities. To improve the system, it was extended to include a Kalman filter in combination with a radial basis function neural network to account for non-linear uncertainties in the Kalman filter. Based on the results presented in the previous section, when estimating the welding trajectory relative to the joint position, the monitoring system achieved an accuracy within ± 0.2 mm between individual welds with a total cost time of 3.05 s. In addition, it was able to detect an offset in the welding trajectory of 1 mm within an accuracy of ± 0.05 mm. The system should however be tested under a more extensive set of different scenarios to better evaluate the robustness and to further validate the monitoring system.

Replacing the implemented method for locating the joint with a convolution neural network could improve the accuracy, however at the expensive of an increased cost time in the form of network training. Implementation on a convolution neural network was investigated for this paper, but due to inadequate amount of training data, it was not possible to produce a detector, that outperformed the method. Another interesting aspect to investigate further is the possibility of measuring the displacement of the weld trajectory along the Z direction, the axial direction of the laser, by applying the principles behind stereo vision to estimate the depth parameter in the video.

Acknowledgement

A sincere thanks must be directed to our supervisor Benny Endelt, co-supervisor Jens V. Boll, Peter T. Sørensen and Kenneth K. Meyer for their guidance and collaboration.

References

[1] W. Huang, R. Kovacevic, Development of a real-time laser-based machine vision system to monitor and control welding processes. International Journal of Advanced Manufacturing Technology, 63 (2012) 235–248.
[2] W. Huang, R. Kovacevic, A laser-based vision system for weld quality inspection. Sensors, 11 (2011) 506–521.
[3] M. de Graaf, R. Aarts, B. Jonker, J. Meijer, Real-Time Trajectory Generation for Sensor-Guided Robotic Laser Welding, IFAC Proceedings Volumes, 39 (2006) 382-387.
[4] M. de Graaf, R. Aarts, B. Jonker, J. Meijer. Real-time seam tracking for robotic laser welding using trajectory-based control. Control Engineering Practice, 18 (2010) 944–953.
[5] W. Cieszyński, M. Zięba, J. Reiner, Real time trajectory correction system of optical head in laser welding. Acta Mechanica et Automatica, 9 (2015) 265–269.
[6] R.-K. Zäh, B. Mosbach, J. Hollwich, B. Faupel, Modelling and control for laser based welding processes: modern methods of process control to improve quality of laser-based joining methods. High-Power Laser Materials Processing: Applications, Diagnostics, and Systems VI, 10097 (2017) 100970A-100970A-13.
[7] S. M. Portnov, I. K. Israfilov, A. V. Perestoronin, A. G. Grigoryants, V. V. Zvezdin, A system for automatic control of precision laser welding in engineering. Welding International, 29 (2015) 801–804.
[8] Nilsen, M., F. Sikström, F., A. K. Christiansson, A. Ancona, Monitoring of Varying Joint Gap Width during Laser Beam Welding by a Dual Vision and Spectroscopic Sensing System. Physics Procedia, 89 (2017) 100–107.
[9] X. Gao, X. Zhong, D. You, S. Katayama, Kalman filtering compensated by radial basis function neural network for seam tracking of laser welding. IEEE Transactions on Control Systems Technology, 21 (2013) 1916–1923.
[10] J. Canny, A Computational Approach to Edge Detection. IEEE Transactions on Pattern Analysis and Machine Intelligence, PAMI-8 (1986) 679-698.
[11] R.O. Duda, P.E. Hart, Use of the Hough Transform to Detect Lines and Curves in Pictures. Communication of the ACM ,15 (1972) 11-15.
[12] H. Bay, T. Tuytelaars, L. V. Gool, SURF: Speeded Up Robust Features, Computer Vision and Image Understanding, 110 (2006) 404-417.
[13] S. Chen, C.F.N. Cowan, P.M. Grant, Orthogonal least squares learning algorithm for RBF, IEEE Transactions on Neural Networks, 2(1991) 302–309.

ISSN (online): 2446-1636
ISBN (online): 978-87-7573-655-3

AALBORG UNIVERSITY PRESS